UNIVERSITY OF OKLAHOMA

GRADUATE COLLEGE

M13 BACTERIOPHAGE-BASED POLYMERS, A PROMISING NEXT GENERATION
OF BIOHYDROGEL

A DISSERTATION

SUBMITTED TO THE GRADUATE FACULTY

In partial fulfillment of the requirements for the

Degree of

DOCTOR OF PHILOSOPHY

By

James Lee Cho

Norman, Oklahoma

2018

M13 BACTERIOPHAGE-BASED POLYMERS, A PROMISING NEXT GENERATION
OF BIOHYDROGEL

A DISSERTATION APPROVED FOR THE

DEPARTMENT OF CHEMISTRY AND BIOCHEMISTRY

BY

Dr. Chuanbin Mao, Chair

Dr. Ronald L. Halterman

Dr. Wai Tak Yip

Dr. Zhibo Yang

Dr. Roger G. Harrison

Acknowledgements

When I first came to the University of Oklahoma, I was filled with hopes and dreams of being a great scientist despite my greenness in the field of research at that time. However, I did not take long to realize that I would need to be very lucky and fortunate to be a good scientist after numerous failures and unexpected results in my early research. I was tremendously blessed to have many people who helped me get through all the troubles in my graduate life. I am standing where I am now because of the help I received from my colleagues and other great minds at OU. This overwhelmingly thankful experience made me a better and humble scientist.

Firstly, I do not know how to thank Dr. Chuanbin Mao enough for all the support that I have received from him. Literally speaking, I would not have been able to succeed in my graduate school life without him. He is the reason that I have successfully finished the required assignments to be a PhD. I would also like to express my gratitude for all my committee members. They have instructed and encouraged me in many positive ways which helped me advance in my research projects. Their helpful and informative advice indeed empowered me to come up with a new scientific and critical method to prove logical points in my projects.

Secondly, I have many other people whom I owe for my research. Dr. Brian P. Grady and Dr. Jie Gao have gently trained me to perform hydrogel characterization with the torsional rheometer in Stephenson science center, and Dr. Preston L. Larson has successfully helped me perform a lot of TEM/SEM imaging on my samples. I also want to thank Dr. Tingting Gu for her time and effort to generate beautiful confocal images of my samples. Dr. Binrui Cao and Dr. Penghe Qiu, research professors in Dr. Mao's lab, have helped me much, and I have learned

many techniques and methods from them in the lab.

Thirdly, I want to thank my valuable colleagues who are my friends and I also want to thank the undergraduate researchers who helped my research, Isaiah Gilley and Sarah Stark. They have become best friends of mine and made my graduate life much less painful and more endurable. They have tried their best to help my research and give me useful advice. They have truly inspired me to be a better scientist.

Fourthly, my family members, my father (Kyu-Cheol Cho), my mother (Hea-Suk Lee), and my brother (Woohyun Cho), have been a great anchor and support for my entire life. Without their heartwarming encouragements and kind words, I would not be standing where I am today. I love them so much and am so proud to be their son and brother.

Lastly, I believe that God has given me all the blessings and graceful environments to grow me as a faithful Christian scientist. I sincerely thank and praise his almighty work that he has done for me and anybody else around me. I hope that I can venture my path in my future, pursuing his plan.

Table of Contents

List of Tables

List of Figures

List of Abbreviations

2D	two-dimensional
3D	three-dimensional
B31 Phage	(HQKLVFFAED peptide-displayed) M13 phage
BT	ferroelectric tetragonal barium titanate (BaTiO3)
Calcium ion	Ca^{2+} ion
CD	circular dichroism
CNS	central nerve system
Copper (II) ion	Cu^{2+} ion
DAPI	4,6-diamidino-2-phenylindole
ECM	extracellular matrix
ESI	electrospray ionization
EPR	electron paramagnetic resonance
Gold (III) ion	Au^{3+} ion
Gold Nanoparticles	AuNPs
GT2 Phage	(GTGAGTGTGAGIRTG peptide-displayed) M13 Phage
M13 bacteriophage	M13 phage
MALDI	matrix-assisted laser desorption/ionization
MC	Monte Carlo (MC) simulations
MS	mass spectrometry
MCF-7	breast cancer cell line MCF-7
MDA-MB-231	breast cancer cell line MDA-MB-231
NPs	nanoparticles

OD	optical density
PCR	polymerase chain reaction
PrP	Platelet-rich plasma
SEM	scanning electron microscope
TEM	transmission electron microscope
WT phage	wild-type M13 phage

Abstract

Hydrogel has been considered a promising material for many biomedical applicational researches due to its unique properties. One such promising hydrogel is a peptide-based hydrogel due to its excellent biocompatibility and bioinjectability, which are important properties for most biomedical applicative research. However, synthesis of peptide is a biohazardous, difficult, and expensive process. M13 phage can be a better alternative biomaterial as a monomer for constructing a good hydrogel because of easy amplification process, cost efficiency, and safe, bio-green chemical production. In this thesis article, copper-M13 phage hydrogel shows a good cytotoxicity to breast cancer cell lines via pH-controlled release of copper (II) ion-phage complex at body temperature 37°C. Gold (III)-M13 phage hydrogel has been constructed via metal-beta amyloid peptide interaction in a stable form in various aqueous biochemical media. It induces fine gold nanoparticle synthesis after the reduction of gold (III) ion by phages in the hydrogel. M13 phage-based hydrogel has a great potential to become a next generation biopolymer in the near future.

Chapter 1. Introduction

1.1 Introduction of general background information

Biological polymer (hydrogel) is a promising biomaterial for many biomedical researches due to its biocompatibility, bio-injectability, biostability, and useful multiple functionality.[1-3] Most hydrogels have been designed and used for tissue engineering research such as building up blood vessels[4] and growing and differentiating stem cells in a controlled manner.[5-6]

One of the best biological hydrogels is a peptide-based hydrogel because it generally shows higher values in those biocompatibility, bio-injectability, biostability, and useful multiple functionality than is present in other biological hydrogels.[7-8] One of the methods to construct a peptide-based hydrogel is to use metal ion-peptide interaction. In most metal ion-peptide interactions, electrostatic force between cationic metal ions and the negatively charged side chains of a peptide generate a strong interaction to form a bond between them.[9] Through this type of bonds, metal ions and certain peptides can form various types of hydrogels. However, synthesis of the peptides is a difficult, expensive, and biohazardous process. Peptide-based hydrogels cannot be easily used in a large quantities due to these reasons.[10-12]

M13 phage is an easily genetically engineerable bacterial phage made of one single strand DNA and coat proteins. Except the single strand DNA in the phage, the phage is simply a complex of proteins.[13] Through the similar metal ion-peptide interaction of peptide-based hydrogel, metal ion induced M13 phage-based hydrogel has been successfully made and has showed great potential in many biomedical applications. Additionally, the amplification process of engineered M13 phage is safer, easier, and cheaper than that of peptide-based hydrogel. In chapter 1, the unique

properties and possible benefits of using M13 phage for hydrogel formation, compared to peptide hydrogels, will be discussed, and the fundamental mechanism of M13 phage hydrogel formation will be introduced through similar examples of peptide hydrogels.

1.1 General background of M13 phage

M13 phage is a lysogenic bacterial phage that only infects its host cells (gram negative bacterial cells).[14-15] Due to its many unique properties, M13 phage has been used for many biological researches. For instance, the morphology and liquid crystalline structure of M13 phage can be used as a Nano-scaled building block to construct a 2-dimensional (2D) structure such as a phage film for stem cell growth.[16-17] However, there are only a limited number of scientific journal articles that have reported a 3-dimensional (3D) structure of M13 phage.

1.1.1 M13 phage structure and morphology

Interestingly, the width and length of M13 phage are neither definite nor specifically uniform. The reported range of width is only 5-8 nm long, and the length one of M13 phage is 870-960nm long. Therefore, M13 phage has a long length-changeable filament-like shape because M13 phage has 2700-2800 copies of its major coat proteins (pVIII) but only 5-6 copies of minor coat proteins at each end of the M13 phage; pVII and pIX coat proteins comprise one end, while pIII and pVI coat proteins comprise the other end of the M13 phage. (Figure 1.1) M13 phage contains a circular single-stranded DNA genome that can be easily engineered (ssDNA, usually 6.4kb).[18-19]

M13 Bacteriophage
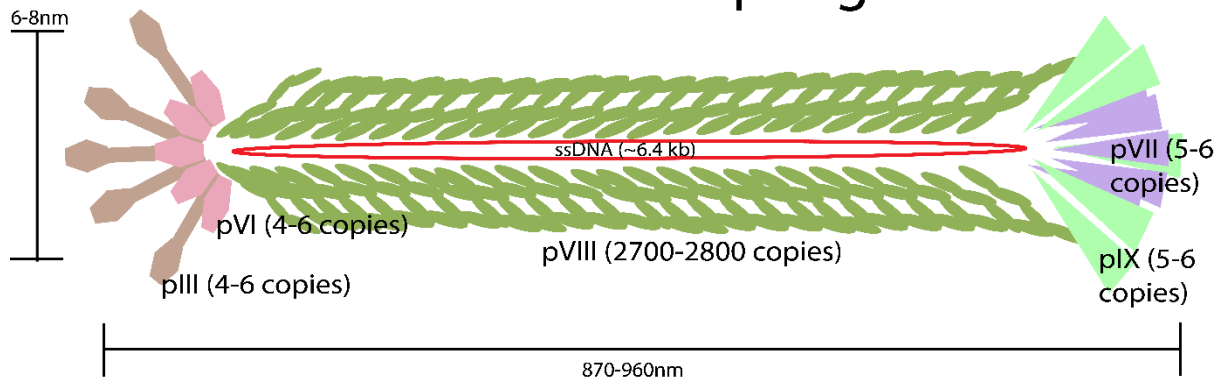
Figure 1.1 The morphology of M13 Bacteriophage, M13 bacteriophage has a filament like shape. It stores its single stranded DNA in its several coat proteins; pIII, pIV, pVI, pVII, pVIII, and pIX. The designed longer DNA genome size can generate the longer M13 phage, meaning more copies of pVIII coat proteins.

The surface of WT phage contains chemically workable amino groups in N-terminal alanine and in lysine (Lys8) and carboxylic acid groups in glutamic acid (Glu2) and aspartic acid (Asp4 and Asp5) on pVIII.[20] By displaying the desired molecular structures on the phage, the molecular displayed phage can be utilized for many conventional biomedical applications of viruses without genetic manipulation of the virus surface. And, when genetic modification is needed, it can also expand its repertoire of biomedical applications. Both covalent and noncovalent chemical modifications, some in conjunction with genetic modifications, generate enhancements on natural functionalities such as targeting, imaging cells, cell cytotoxicity, gene delivery for treatment, and tissue regenerating functionalities for both specific diagnosis and treatment. (Figure 1.2)[21]
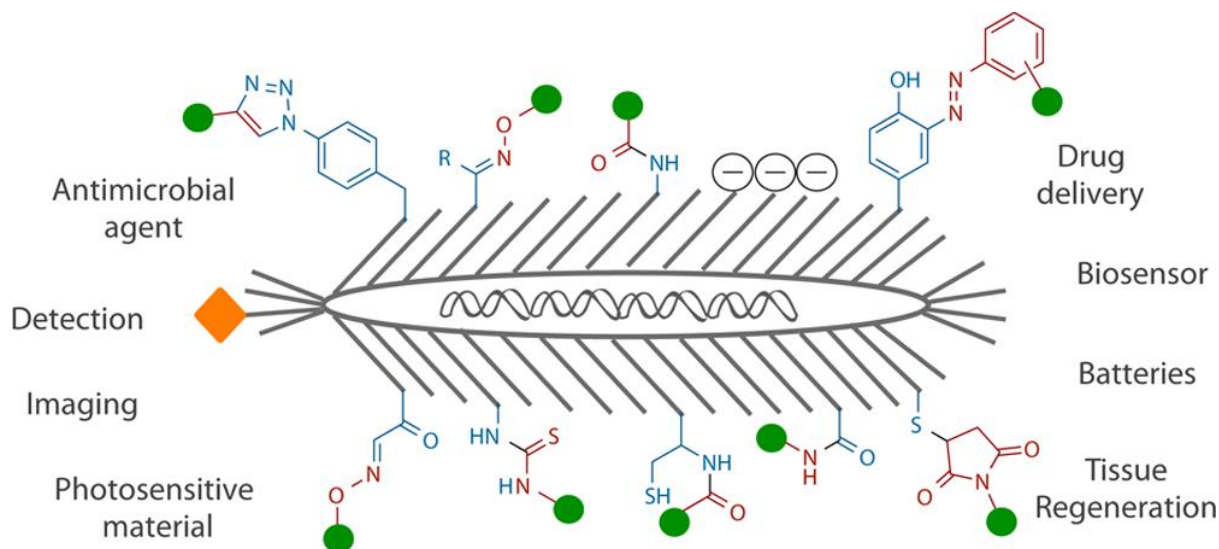
Figure 1.2 Chemically Modifying M13 phage, because of chemical modifiable properties of M13 phage, chemical modifications can be executed to imbue the M13 phage more useful/active/stronger functions for many biomedical purposes.

1.1.2 M13 phage liquid crystallinity and Phage display

M13 phage has the unique property of self-assembly because M13 phage is able form the liquid-crystalline structure due to its dipole characteristics. The liquid-crystalline property of these phages often empowers the self-assembly mechanism of the phage to transform into phage films.[22] Due to this unique property alone, the M13 phage can be used as a potential bio-battery. It is reported that M13 phage can be possibly used as an actuator or energy harvester. In the article, a higher energy output can be obtained by combining ordered phage films in series or parallel configurations in gold coated substrate. (Figure 1.3)[23]
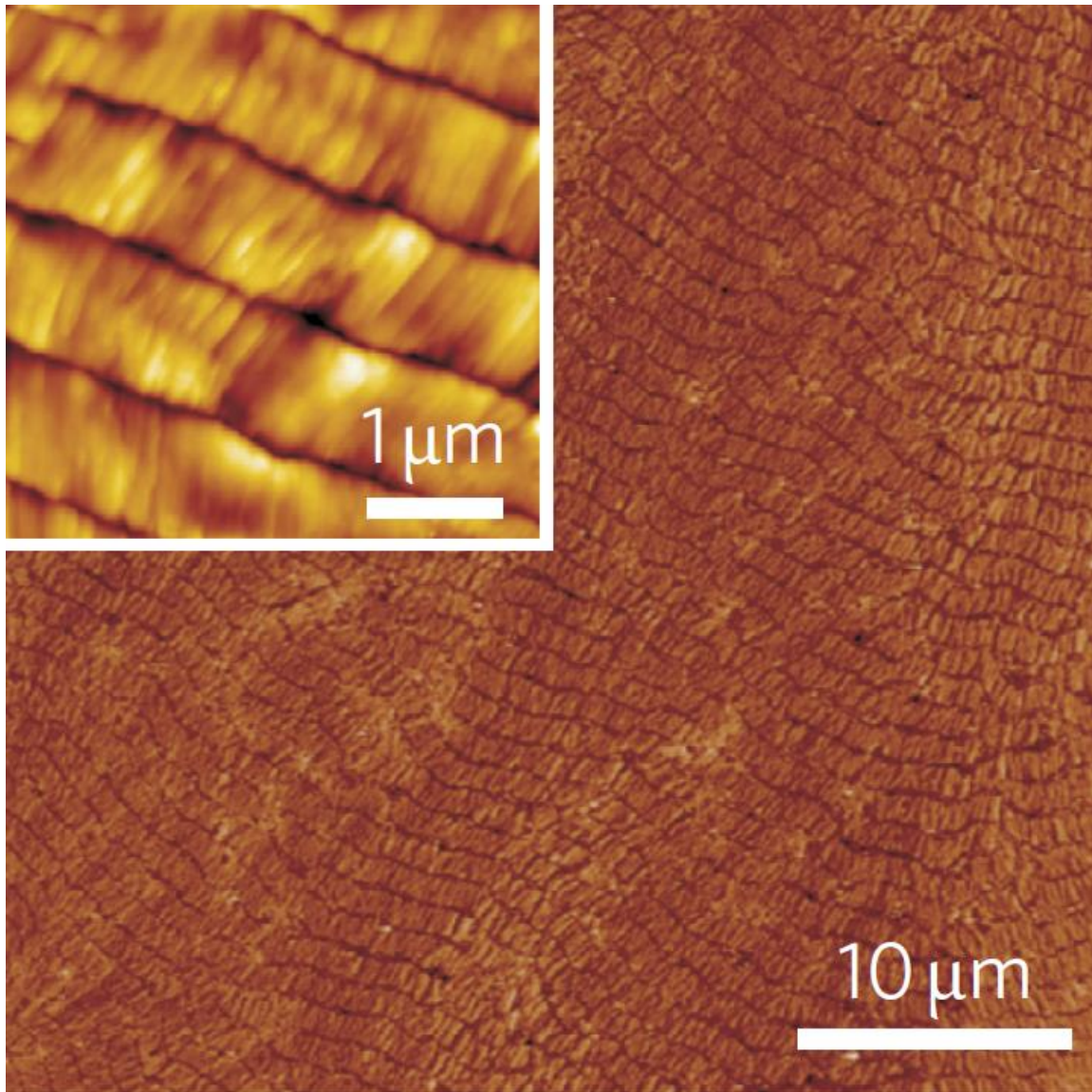
Figure 1.3 M13 phage film in AFM topography, a long-range ordered liquid-crystalline film (in smectic phase) is shown. Inset: smectic-aligned phage bundles are in ~1 μm thick bands.

Additionally, M13 phage can be more usefully fabricated for other biomedical researches with phage display including bio-panning methods. (Figure 1.4)[24] Lysogenic M13 phages do not break the host gram-negative bacterial *E. coli* cells during the process of infection and amplification. Rather than killing the host cells,

the M13 phage undergoes lysogeny, making the phage genome integrate with the host DNA and replicate. Therefore, nonlytic M13 phage is one of the best bacteriophages that can be used in recombinant DNA engineering for phage display.[24] Phage display is a method to functionalize the liquid-crystalline M13 phage. Phage display broadens up the bio-application range of M13 phage.[19] Beside the liquid-crystallinity of M13 phage, M13 phage can be even a better biomaterial with phage display for biomedical applications such as the identification of peptides, proteins, or antibodies with a high affinity for a specific target molecules or cells or tissue. Once bio-panned peptides are revealed, the peptide genetically fused M13 phages can be utilized to bear target-specific peptides or proteins for biorecognition. The specific peptide can be genetically fused to the N-terminus ends of pVIII coat proteins.[3] This means that a peptide can be displayed on the surface of M13 phage.
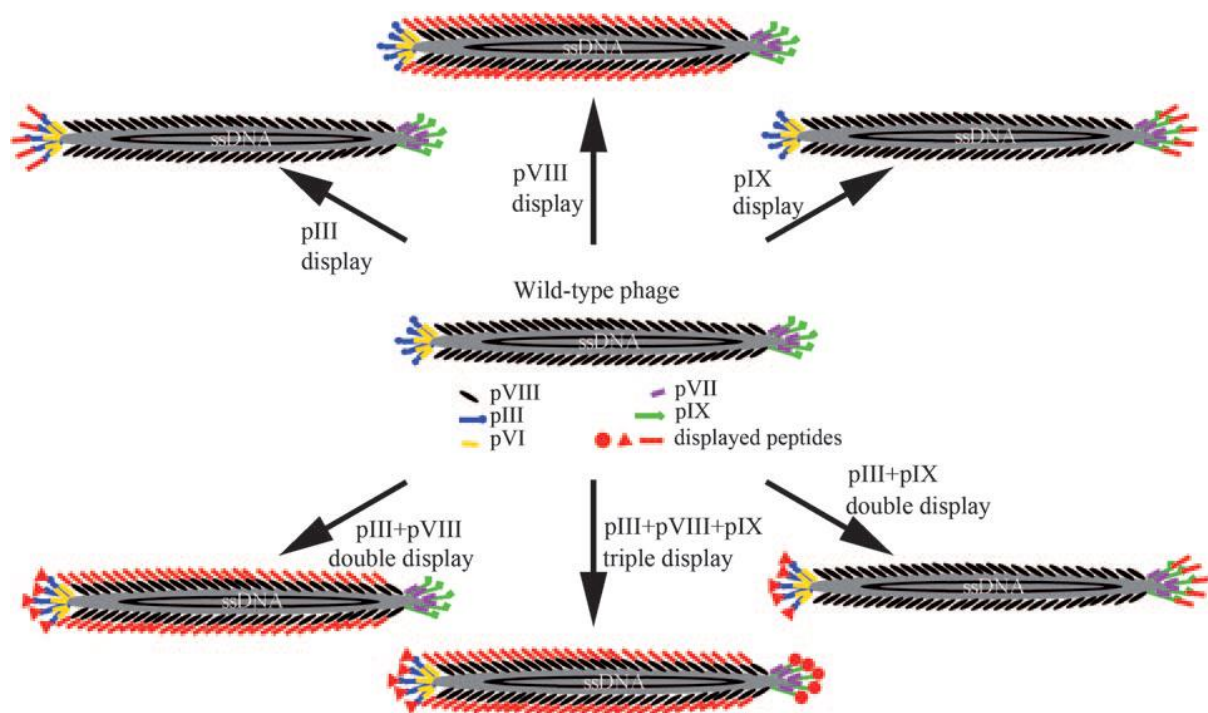
Figure 1.4 Genetically engineered versions of filamentous phage (M13 bacteriophage), the arrows show different genetic modifications that display a

peptide on the surface of the different phage coat protein by genetic fusion. Through the site-specific modification method to genetically alter the phage DNA, the foreign peptide (in red) can be fused to the coat protein.

The displayed peptides are selected by the result of the biological evolutionary selection process mentioned earlier, biopanning. A library of billions of M13 phage clones can be used to identify one or more peptides that show a high affinity to a target such as molecules, peptides, cells, or even tissues. (Figure 1.5)[24-25]
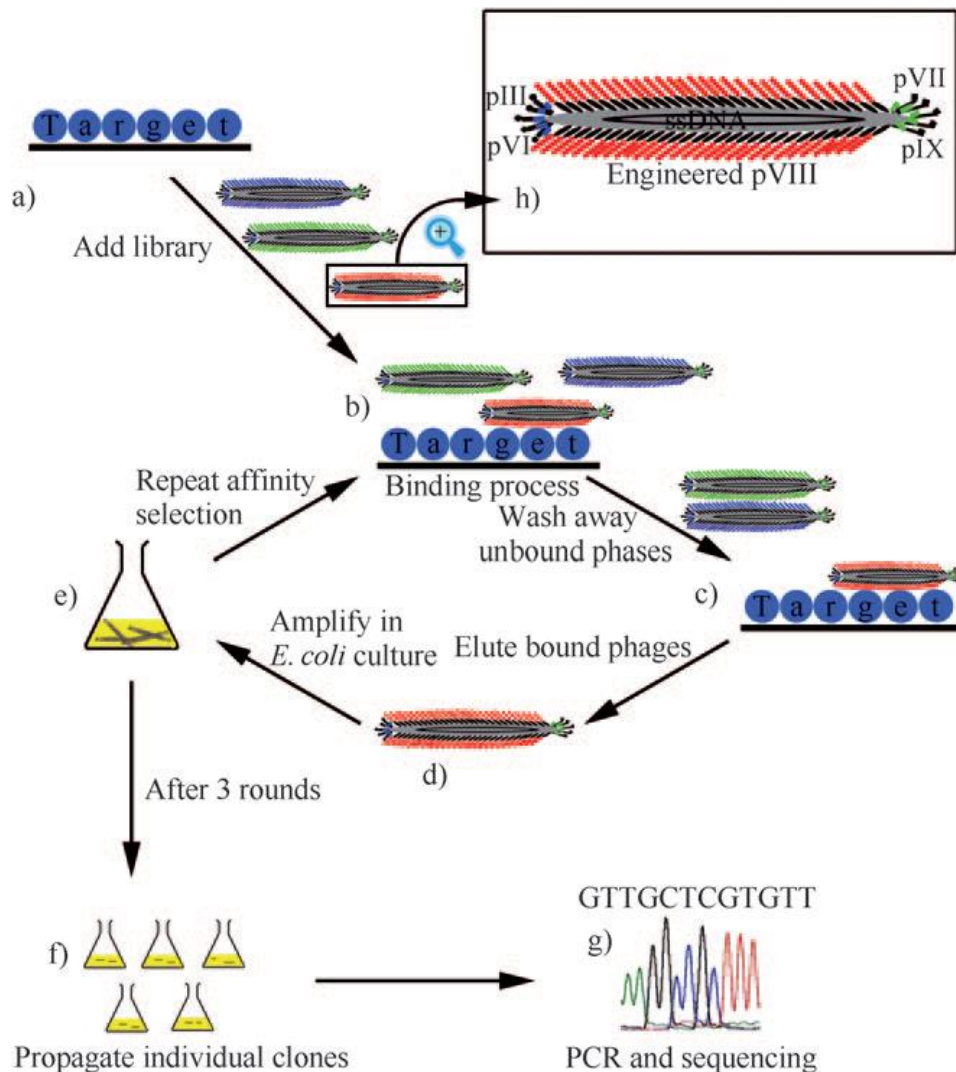
Figure 1.5 Schematic illustration of the biopanning process, a) The target analyte (blue circle) is immobilized on the dish by chemical or biological means; b) a library of billions of phage clones is adjusted to the target analyte for possible interactions; c) the unbound phages are washed/eluted away with a buffer and the bound phages stay bound to the target analyte; d) the bound phages are eluted away from the analyte with an elution buffer; e) the previously eluted phages are amplified by infecting *E.coli* bacteria in the Luria Broth (LB) medium culture to obtain an amplified library, which is used as an input for (b) in the next round of panning selection; f) after several rounds of selection (b↔e), the best target binding phage clones are proliferated; g) Through the DNA sequencing, the phage DNA is sequenced to identify the target-specific binding peptide.

The displayed peptide on the surface of M13 phage can induce a desired function in their liquid-crystalline structure or interactions with various cells, tissues, enzymes, organic compounds, receptors, or peptides.[26] For instance, the surface-displayed M13 phages can be used as a template via the site-specific nucleation to grow specific nanocrystals. The $BaTiO_3$-binding/nucleating peptide was identified via biopanning with CRGATPMSC (from a phage-displayed random peptide library). The novel peptide was displayed on the surface of M13 phage. On the exterior surface of the M13 phages, crystallographically oriented semiconducting nanowire in ferroelectric tetragonal barium titanate ($BaTiO_3$) can be controlled in size, shape, aspect ratio, crystal orientation, and crystal structure (Figure 1.6)[27]
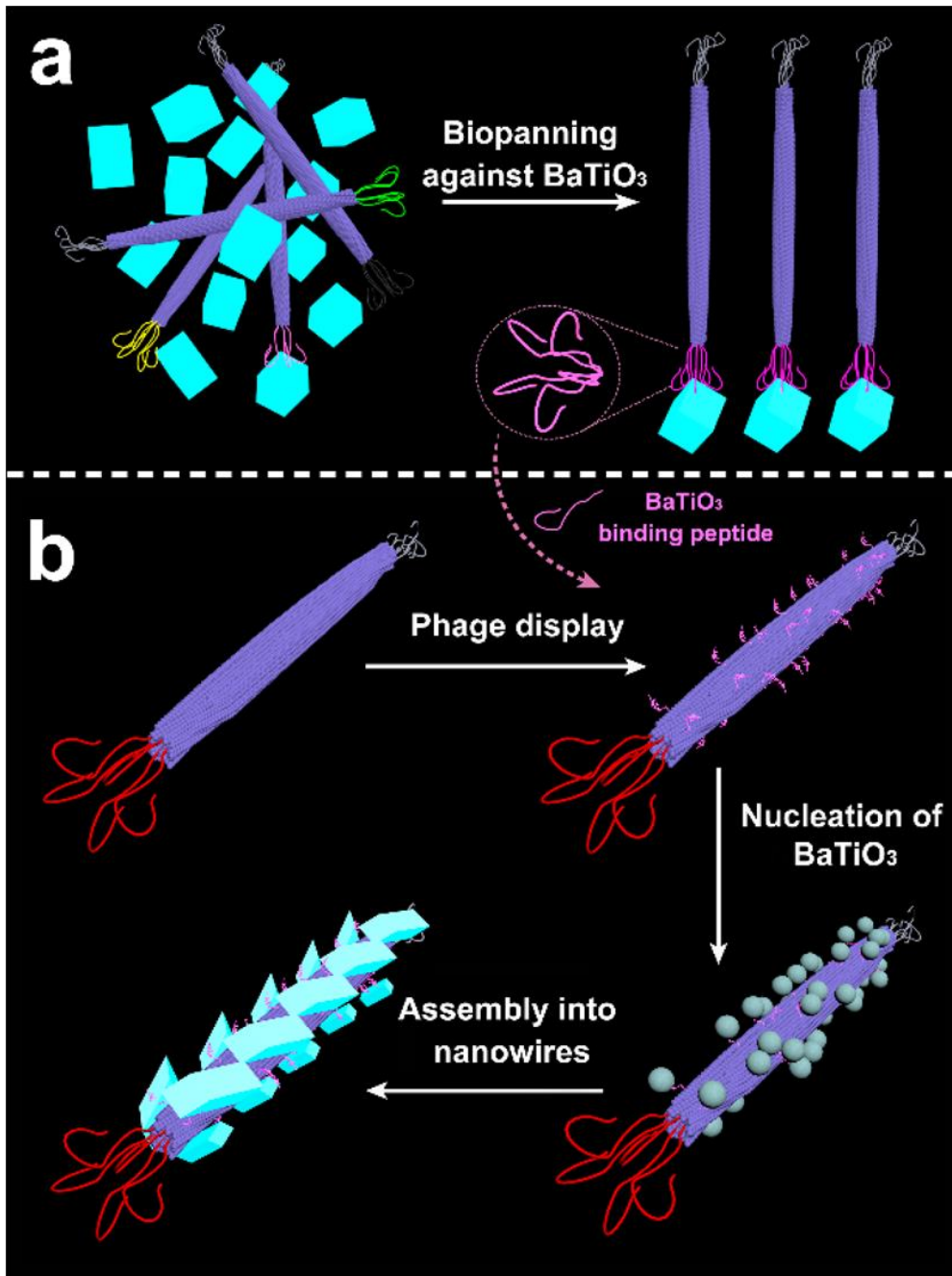
Figure 1.6 Synthesis of BaTiO₃ (BT) Polycrystalline Nanowires at Room Temperature using the engineered M13 phage; (a) Selected BT-Binding Peptides via Biopanning method, (b) Construction of the pVIII-RS (C<u>R</u>GATPM<u>S</u>C (termed RS)) Phage via Displaying of BT-Binding Peptides on pVIII major coat proteins that dictate the nucleation of BT crystals in a form of polycrystalline nanowires

Engineered M13 phages can also be electrostatically conjugated to gold nanoparticles, forming a gold nanowire. The gold nanowires can form a film to measure humidity using the unique surface plasmon resonance spectra (SPR) pattern.[28] For artificial bone biomaterials synthesis via bioinspired mineralization, two different peptides derived from Dentin Matrix Protein-1 were displayed on the surface of M13 phages and these two engineered phages were mixed together to form self-assembled structures to achieve oriented nucleation and growth of HAP crystals to make a bone mimicking organic-inorganic hybrid scaffolds that may form artificial bone structures in the future.[29]

Through the phage display, M13 phages can also bind to biological molecule-inorganic material hybrids as well. For instance, glucose oxidase (Gox) conjugated gold-coated M13 phages were used as a template for making biofuel cells, exhibiting a good direct electron transfer (DET). Through an EDC-NHS chemical crosslinking method, glucose oxidases were covalently bound to gold nanoparticles. glucose oxidases-AuNPs were assembled onto genetically engineered M13 phage. This virus-based strategy induced a greater enzyme surface coverage than other DET attachment methods, resulting in the electrodes with improved electrical contact between the redox enzymes and the conductive metal support by introducing broader scaled, compactly packed, highly conductive "nanomesh" electrodes for biofuel cell applications.[30]

In tissue engineering, the phage film can be manipulated to grow bone regenerative stem cells for the desired/controlled/manipulated differentiation and administration of orientation/morphological growth of the mesenchymal stem cells (MSC) growth. RDG and PHSRN peptide displayed phages were used to make a

biochemical/topographical artificial extracellular matrix (aECM) that can direct stem cell fate. Because of advantages of M13 phage, a virus-activated aECM with constant ordered ridge/groove nanotopography was generated utilizing the self-assembly of easily genetically modifiable phage into a ridge/groove structure. (Figure 1.7)[16]
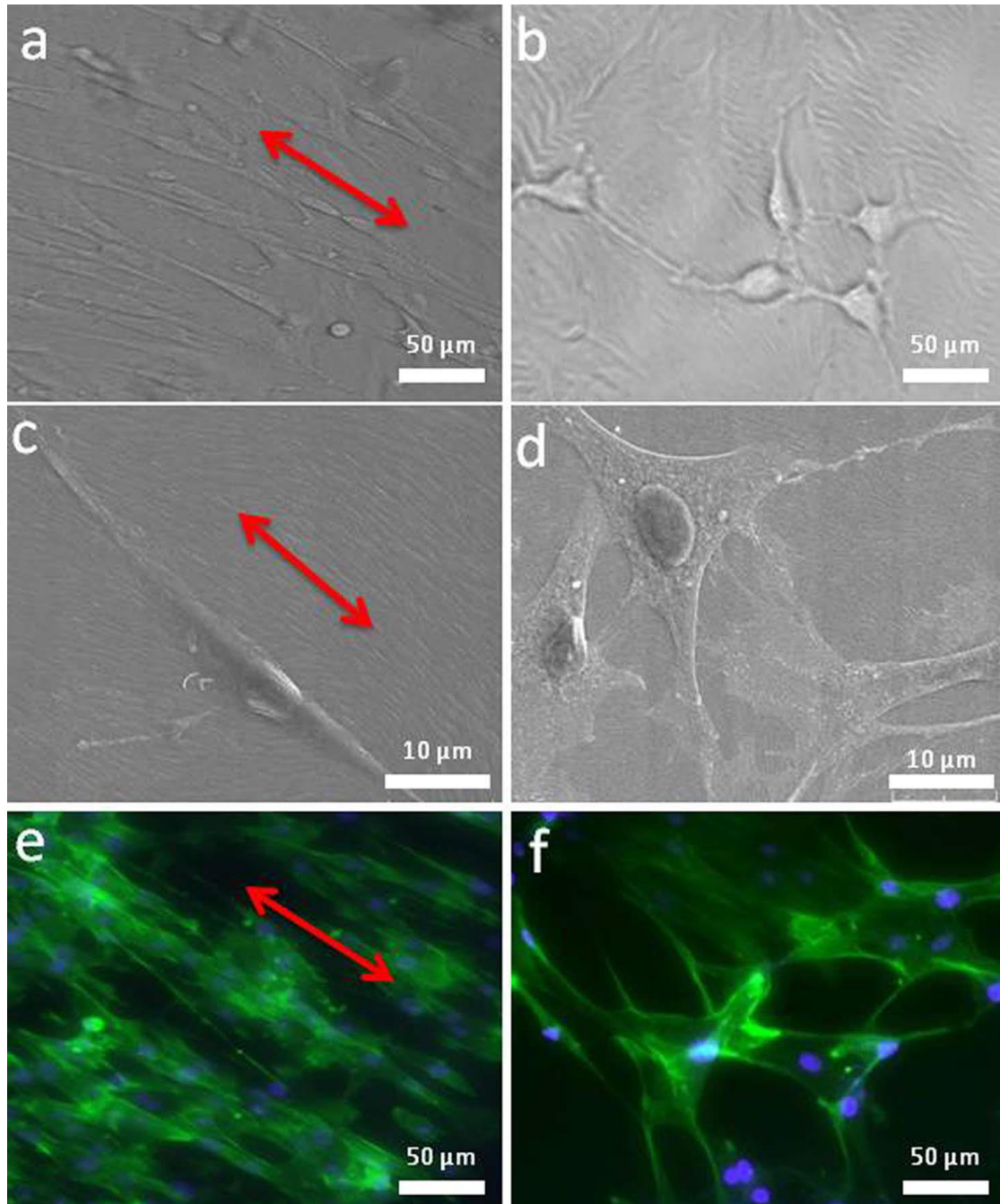
Figure 1.7 MSC adhesion on the phage film created from both low phage

concentration (a, c, e) and high phage concentration (b, d, f), The MSCs on the phage-based film (a, c, e) were significantly elongated and aligned along phage bundles (a, c, e) while those on the phage-based film (b, d, f) were randomly oriented and not elongated in the desired pattern (b, d, f). Bright field optical microscopy (a, b), SEM (c, d) and fluorescence microscopy (e, f) (Cell nuclei stained by DAPI (blue) and F-actin stained by FITC-labeled phalloidin (green))

1.2 Peptide hydrogel formation with metal ions

Peptide hydrogel can be formed in strong metal ion-peptide interactions. Many Metal ions are very important for many biological activities in body. Many proteins are highly involved in various cellular mechanisms with metal cofactors and they often show a strong coordination bond between the metal ions and related proteins. Through the bonds, peptide hydrogel can be constructed. However, the process of synthesizing peptides or proteins is high in the cost, time, labor, and biohazard level.[31] (Table 1.1) Alternatively, M13 phage can be a good peptide hydrogel that may induce better results in biocompatibility, biological injectability, and bio-safety than those of regular peptide hydrogels.[32]

Synthesis Condition (1mg)	Cost	Time	Labor	Biohazard
Peptide	Higher	Longer	Higher	Higher
	$16.32-$24.08 per amino aicd (>98%)	3-5 weeks	Requires lots of chemical processes related to amide coupling	Require lots of biohazardous organic chemicals
M13 phage	Lower	Shorter	Lower	Lower
	~$2.73	4-5 days	Simple biological amplification protocol	Requires a few antibiotics

Table 1.1 Relative Comparison between synthesis of peptide and M13 phage in cost, time, labor, and biohazard terms

1.2.1 Metal-Peptide interactions

Metal-peptide interaction is common and important in living organisms. Metal ion binding has been considered to offer a highly versatile means of generating self-assembled peptide structures that are both specific and highly modular. For instance, the inclusion of metal-binding ligands specifically into synthetic coiled-coil peptides (GCN4-p2L) for hierarchical assembly has been proven in the process of creating nanospheres, nanofibers, and fibrils. The head-to-tail assembly of a trimeric coiled-coil peptide can occur to provide microscale 3D crystals and nanoscale or microscale spheres through metal ion mediation. The metal-ligand interactions at the ends of the growing crystal could be linked to direct His-tagged fluorophores to

specific locations within the 3D peptide crystals, creating a notable feature of the head-to-tail crystallization. Metal-mediated directional assembly encourages the formation of trimeric coiled coil linear stacks. Surface exposed residues in the coiled coils can support an antiparallel packing arrangement to maximize the electrostatic interactions between a group of positive residues at the C-termini and negative residues at the N-termini of the coiled coils. (Figure 1.8)[33]
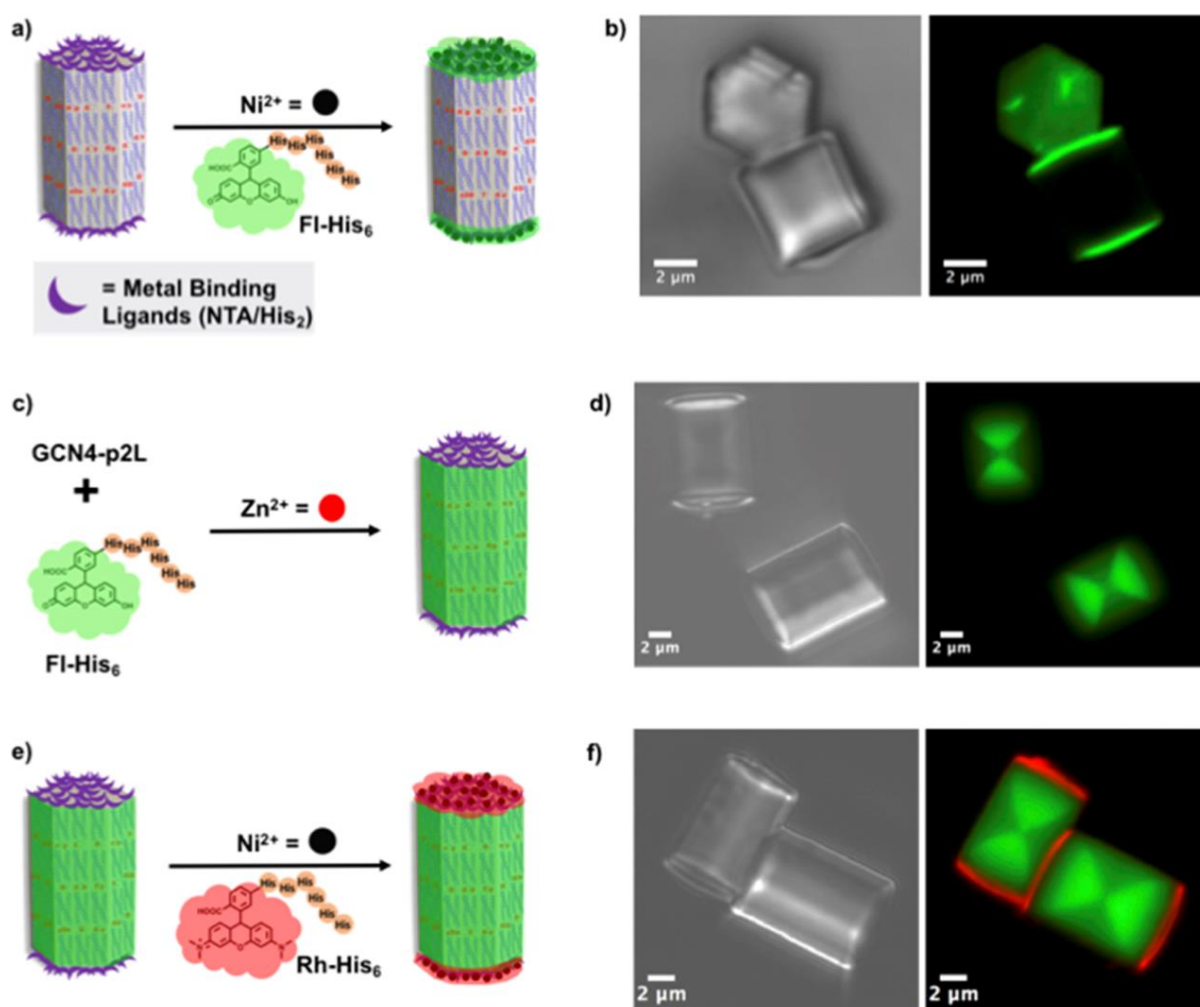
Figure 1.8 Directing His-tagged fluorophore guest molecules to the Zn (II)/GCN4-p2L (The coiled-coil helical peptide) crystals; (a) the hexagonal faces of the crystals containing free metal-binding ligands, N-terminal nitrilotriacetic Acid, (NTA) with metal ions that bind to His-tagged cargoes, (c) guests within the core of the crystals

in a His-tag-dependent fashion within the crystal during formation, or (e) at both the surface and within crystals. Bright-field (left) and confocal (right) microscopy images of (b) after hexagonal crystal treatment with Fl-His6 (fluorescein labeled histidine in Green), the fluorescence was located only at the hexagonal top and bottom faces of the crystal (0.1 mM), (d) Fl-His6 added during the formation of the crystals, and (f) crystals in the presence of Fl-His6 (0.1 mM) with Rh-His6 treatment (0.1 mM) after crystallization.

Especially, metal cations are well-known to be important for cellular activities such as stabilization of protein structural folds (Mg^{2+}, Ca^{2+}, and Zn^{2+}), oxidative catalysis via electron transfer (Mn^{2+}, Fe^{2+}, and Cu^{2+}), and cellular signaling and metabolism (Na^+, K^+, and Ca^{2+}). A third of all proteins (such as metalloproteins) are involved in cellular mechanisms that require a metal cofactor with the divalent metal cations of Mg^{2+}, Ca^{2+}, Zn^{2+}, and Mn^{2+}. The transition metal cations (Co^{2+}, Ni^{2+}, Cu^{2+}, and Zn^{2+}) are relatively softer borderline-acids that usually coordinate with the softer bases of nitrogen or sulfur-containing residue side chains of histidine or cysteine. The transition metal cations can also coordinate to harder moieties such as carboxylic acids in the side chains of aspartic acid and glutamic acid. The selectivity of the metal ion interactions is largely determined by the offered peptide functional groups. The preferred interaction for the transition-metal cations with specific amino acid residues was found. Metal ion (Mg^{2+}) showed the selective interaction with certain residues (specifically His, Cys, Asp, and Met).[34]

Among metal ions, transition-metal ions (such as copper) are essential elements in all living systems, but they can also trigger pathological disorders under

certain occasions. In vivo studies, copper can anchor to the sites of the thiol moieties of cysteines and the imidazole residues of histidine. All these interactions are highly dependent on reaction conditions. The other groups of a peptide can also be involved in the coordination-bond to copper. Several techniques (such as X-ray or nuclear magnetic resonance, mass spectrometry (MS), electrospray ionization (ESI) and matrix-assisted laser desorption/ionization (MALDI)) can be used for locating metal bindings with inorganic/organic/bioinorganic complexes, a Copper (II)-histidine/arginine-containing peptide, angiotensin III (RVYIHPF). This peptide has been selected and used to form Cu-aniotensin III complex in the process of studying the relative complexation properties of the two oxidation states.[35]

Peptides are operative and specific ligands for various metal ions (such as Cu^{2+}) in the formation of protein-metal complexes, and they have a decisive influence on protein-folding mechanisms because they act as a regulator of copper concentration and reactive oxygen species. This might be the reason that the prion protein that binds Cu (II) ions makes the transition from the native to the pathological form of Platelet-rich plasma (PrP) due to the copper coordination in the structure of the prion protein. Cu^{2+} coordinately binds to the N-terminal domain, composed of four or more repeats of the eight-residue sequence PHGGGWGQ (octarepeat), confirmed in electron paramagnetic resonance (EPR) and circular dichroism (CD) experiments, X-ray diffraction (XRD) experiments.[36]

Histidine-rich peptides have been considered widely as peptides with high affinities to metal ions. However, through histidine-metal complexation and protein deformation, such peptides can damage the central nerve system (CNS) to cause Parkinson's and Alzheimer's diseases. A nanotube-form of immobilized histidine-rich

peptides (AHHAHHAAD) was used as a template for metallic nanowire synthesis by mineralizing gold nanocrystals on the nanotubes in the uniform size distribution. The pH change fluctuates peptide-metal ion interactions, mainly because of the charge distribution variations in electron donor groups of peptides. The different interactions between peptides and metal ions make the chemical structure change of the ion-peptide complexes. One of the main driving forces of metal-peptide binding is the electrostatic force. It eventually controlled the size and the morphology of nanocrystals after the reduction of the ions due to initial pH changes.[37]

Tezcan and coworkers have reported another transition metal ion (Zn (II) ion) as an important ion for the metal ion-peptide interactions. Strategic placement of Zn (II)-binding motifs within cytochrome cb 562 protein allowed the formation of 2D and 3D crystalline arrays.[38] Metal ion (Zn (II) plays a role of linking the cytochrome motif derived peptides.

1.2.2 Metal-peptide hydrogels

The term hydrogel can be defined as a three-dimensional hydrophilic polymer network system that can absorb certain amount of water through the hydration in an aqueous solvent.[39] Gelation (sol-gel transition) is the process of linking of monomers to form progressively larger branched yet soluble polymers from the structure and conformation of the starting material. Continuation of the gelation process eventually increases the size of the branched polymer with decreasing solubility. After the critical point (gel point), a gel starts to appear. Hydrogels can be stimuli sensitive and respond to the surrounding environmental stimuli such as temperature, pH, electric field, and light. Any pH-sensitive polymer structurally contains hanging acidic or basic

groups that respond to the pH changes in their environment by gaining or losing protons.

Certain peptides can be used as monomers to form peptide-based hydrogels. Peptide hydrogel has unique properties. Peptide hydrogel shows a high biocompatibility and bioactivity because of its biological structure. This is the reason novel peptide-based hydrogels can be used in biomedical research utilizing these unique properties.[40]

Peptide hydrogel can be categorized into several types. The most common type of peptide hydrogel is a self-assembled peptide hydrogel through peptide-peptide interactions.[41] Self-assembly peptide can form a hydrogel alone or with an inducer (such as pH, temperature, and ions).[42] For instance, Various β-hairpin forming peptide-based hydrogels can intermolecularly self-assemble into nanofibrillar, physical hydrogels after intramolecular folding. These β-hairpin peptide hydrogels showed injectable-solid properties and exhibited shear-thinning flow during syringe injection before rapid solid recovery. Gelation time, stiffness, and network mesh size can be modified via molecule design and solution conditions that control the intermolecular self-assembly into a hydrogel polymerized system.[43]

Some peptides can form a hydrogel through metal-peptide interactions. These peptide based-hydrogels often become novel biological platforms for local, injectable applications because of the capability of their encapsulation and distribution properties of materials such as drugs, large proteins, and even cells with bio-injectability properties.[8, 44] After the biological injection, the hydrogel may continuously release chemotherapeutical molecules, remaining in the desired location for a desired time period, possibly replacing dangerous surgeries and

invasive procedures. Many injectable hydrogels are constructed to be precursors that assembles in vivo when the reaction conditions reach the desired temperature, ions, pH, or certain radiations. (Figure 1.9)[45-46] The injectable hydrogel can be made in a solid form within a syringe without the need for additional external interactions.[47]

MAX1: VKVKVKVKV^{D}PPTKVKVKVKV-NH$_2$
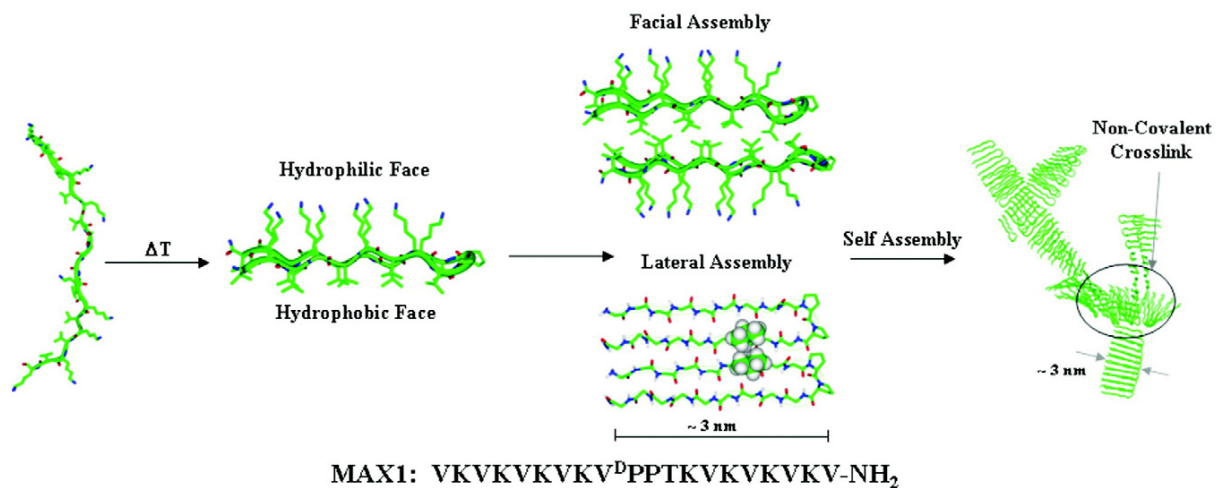
Figure 1.9 MAX1 (self-assembly peptide) intramolecular folding mechanism with consequential intermolecular assembly, A desired trigger can be a change in salt concentration, pH or temperature (figure 1.9) to order the peptides to fold and form lateral and facial self-assembled structures of fibrils even whole hydrogel network structure

1.2.3 Alternative of Metal-peptide hydrogel

M13 phage hydrogel can be a good alternative for peptide hydrogel. Peptide hydrogel synthesis requires difficult and expensive processes with biohazardous chemicals. However, M13 phage hydrogel is an easily creatable and cheap biomaterial that can contains every advantage of peptide hydrogel. M13 phage is made of several coat proteins and single stranded DNA.

Most filamentous biopolymers (such as DNA and protein filaments) are highly

charged polyelectrolytes in compact and highly ordered forms in body. The net force between two adjacent polyions can be attractive due to the correlated fluctuations in the ion clouds around the polyions, following Poisson-Boltzman treatment with an introduced correlation between counterions by Asakura-Oosawa approximate analytical treatment. At smaller distances between filaments, the Manning condensation of ions on the surface of charged rod-like filaments may induce strong spatial correlations of ions or even the formation of Wigner crystals. Electrostatic attraction for rod like polyelectrolytes was also found in Monte Carlo (MC) simulations for a system of hexagonally ordered rod like polyelectrolytes (such as DNA and filamentous phages). Filamentous bacteriophages (fd and M13) are both long and stiff rod-like biological filamentous particles, each with different surface charge density. The protein based viral particles is atomic-resolutive structurally stable in solution over a wide range of ionic conditions. The filament viruses are good model systems to examine theoretical predictions of interactions between rod-like polyelectrolytes with ions. Lateral aggregation of fd and M13 viruses induced by several divalent metal ions (Ca^{2+} and Mg^{2+}) was experimentally found as expected in grand canonical MC simulations considering parameters such as the size of ions and surface charge distributions of the virus particles beside unexpected solubilization at certain ion concentrations. These counterion-mediated electrostatic interactions are primarily responsible for bundle formation induced by the alkali earth-metal ions. Weak ion-specific bonds play a dominant role in the aggregation induced by the transition-metal ions (Mn^{2+}, Zn^{2+}, Co^{2+}, and Cu^{2+}). The exact location and mode of coordination of the divalent ions inside the large bundles is still poorly understood. Filamentous bacteriophages have been widely used as vectors for molecular

20

genetics.[48] Their aggregation properties under various solution conditions can be used for many biomedical applications.
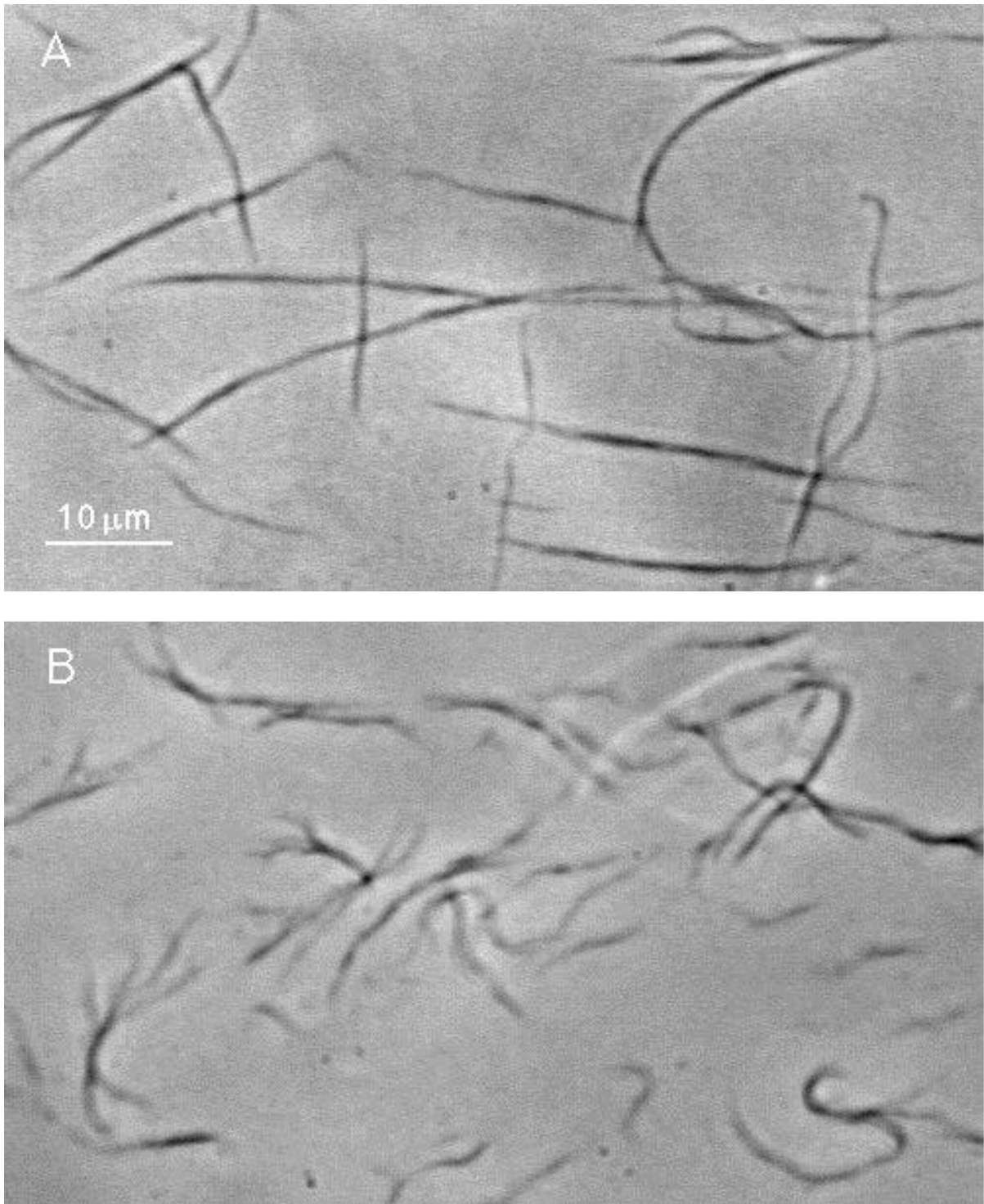
Figure 1.10 Phase contrast microscopy images of filament (A) fd and (B) M13 bacteriophage bundles, fd and M13 phage bundles are induced by 100 mM $CaCl_2$

solution. Each bundle was determined to contain thousands of virus filaments, and the average diameter of the tubular bundles is approximately 0.2μm. M13 bundles are shorter and occasionally branch open toward the ends, indicative of weaker interfilament association.

Chapter 2. M13 bacteriophage-based Hydrogel for Inhibition of Breast cancer growth through pH-controlled release of Cu^{2+}-bioorganic complex at body temperature

2.1 Introduction

Breast cancer is cancer that originates from breast tissues in the body. Breast cancer is one of the biggest health concerns in women.[49] According to American Cancer Society, Inc., Surveillance Research, 40,610 American female patients died from breast cancer in 2017. To cure breast cancer, the related scientists and researchers have been studied several breast cancer cell lines.[50-52] As a result, currently, there are several breast cancer therapies to cure and treat breast cancer. However, despite the invested effort and time, there are still many challenging problems facing the complete cure of breast cancer.[39] Some scientists are considering copper as a possibly good agent for overcoming these current challenging problems.

Copper is an important element for many types of cells and tissues in the body.[53-54] There are many critical enzyme proteins (such as such as cytochrome oxidase[55], zinc-copper superoxide dismutase[56], and lysyl oxidase[57]) that require certain amounts of copper for their activities.[47] These activities are highly involved in cellular growth regulation.[58] It means that adequate amount of copper can help the cells and tissues grow in a regulated manner.

Copper concentration is high in the body of cancer patients.[59] Copper becomes even more important for cancer cells because it is not only a growth factor stimulator, but also a critical angiogenesis inducer.[60] Cancer typically shows a high

angiogenesis property to obtain necessary oxygen and nutrients.[60] Tumor copper plays a great role as a mandatory cofactor for many key proteins inducing angiogenesis. It means that copper depletion can cause a serious problem in the growth of cells and tissues in the body.[61] Indeed, copper depletion have already been successfully proven to be as one of promising cancer therapeutic methods.[62] Intriguingly, copper overaccumulation has also been known to be potentially harmful for cells and used to treat cancer cells.[63-64] Copper salts and complexes can kill cells by damaging DNA strands at high concentration.[65] Among other copper-complexes, copper-peptide complexes can be formed through the interaction of copper with one or more peptides to form a type of metal-complex.[66-67]

In this article, we demonstrate the virus-based hydrogel that can release copper-bioorganic complexes (phage or phage coat proteins) in a controlled manner. This hydrogel can be formed by simply adding Cu^{2+} ions to genetically engineered M13 phage solution displaying a new novel peptide (AGTGAGTGTGAGIRTG) on the major coat protein VIII. M13 bacteriophage (also called phage) is a filamentous virus (870nm-960 nm long and 6-8 nm wide) that specifically infects bacteria. The M13 phage is non-toxic to humans, and it is genetically modifiable in a monodisperse polymer form via phage display method.[24] Interestingly, decomposition rate of the hydrogel (GT2 Hydrogel) is pH-dependent. This pH sensitive decomposition of GT2 hydrogel can show a controlled release of copper-phage complex in the cancer microenvironment at pH 6.5-6.9 at 37 °C. The released copper-phage complex showed a high cytotoxicity to two breast cancer cell lines. (MCF-7 and MDA-MB-231) The MCF-7 and MDA-MB-231 cell lines were chosen for this study because they have been some of the most well-documented cell lines in previously published

studies for their characteristics. The MCF-10A cell line was selected as a healthy cell line to determine the safety level and selectivity of the use of Cu^{2+} ions at different concentrations and Cu^{2+} ion-phage complex.[68-70]

2.2 Materials and Methods

2.2.1 Preparation of the engineered M13 phage

Through previously published methods of phage display[29], a peptide sequence (AGTGAGTGTGAGIRTG) was genetically fused on the pVIII coat proteins on the surface of genetically engineered M13 phage (GT2 phage). (Figure 2.1) The GT2 phage was amplified via the previously published protocol to fulfill the experimentally obtained critical concentration of the engineered M13 phage (2 x 10^{14} phage/ml). The concentration of phage solution was measured using the spectrometer, considering optical density (OD) 0.1 in 1mm pathlength (OD =1 in 1cm pathlength) was unit-converted in to the phage concentration of 1 x 10^{13} phages/ml based on the previously calculated data. The engineered phage solution was microfiltered with a microfilter syringe (CORNING®) whose pore size was 0.2μm. The phage solution was also purified via desalting process to remove ions and small undesired molecules in the phage solution by dialysis with a spectra/Por® 6 dialysis membrane (MW 50kD). Presence of M13 phage was confirmed by bio-AFM imaging using a biological atomic force microscope (Bruker Catalysis). (Figure 2.2)
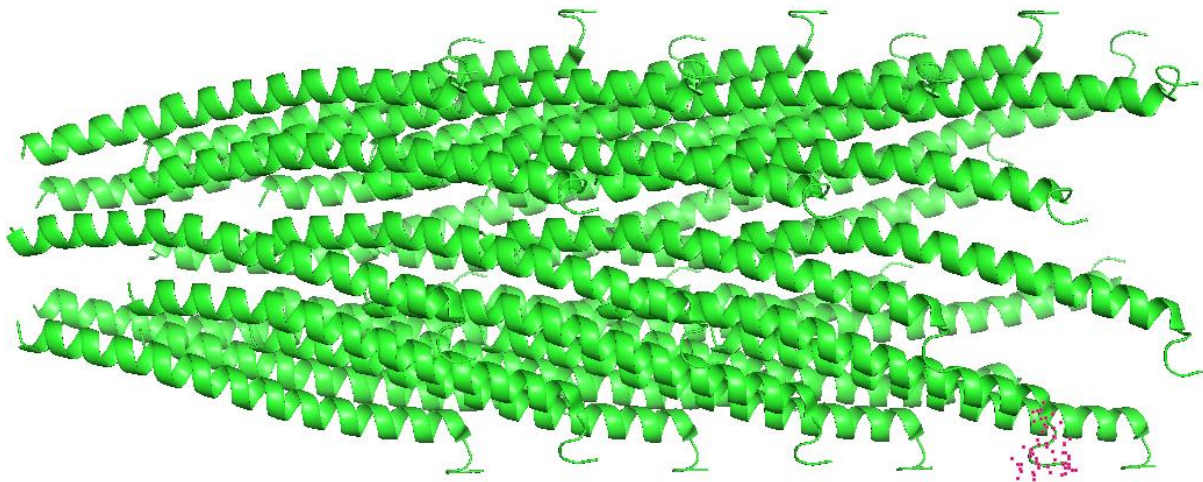
Figure 2.1 The pVIII major coat protein structure from PDB (Protein Data Bank) website, the tip of pVIII coat protein (pink dotted area) is where the novel peptide was genetically fused on the surface of M13 bacteriophage.
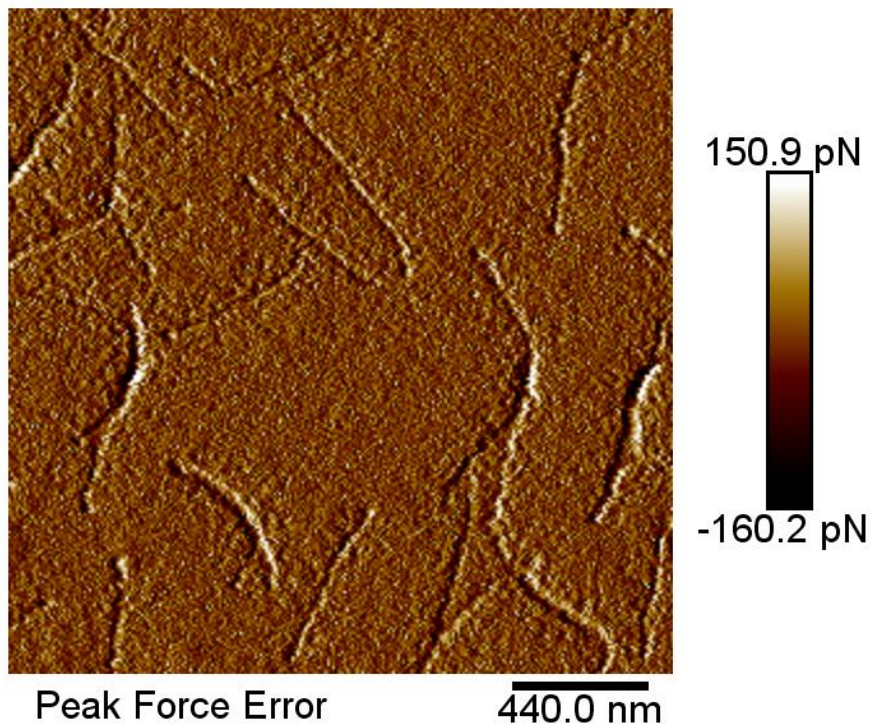

Figure 2.2 GT2 M13 bacteriophage in AFM image, GT2 bacteriophage has also a long filamentous shape like the native form of M13 bacteriophage.

2.2.2 Copper-phage Hydrogel Formation

50µl of 20mM copper (II) was added to 300µl of GT2 phage solution (2 x 10^{14} phage/ml). After 2-3 hours, Cu^{2+} ions were passively and homogenously dispersed in the GT2 phage solution at 37°C and formed a hydrogel with the GT2 phage at room temperature (20 °C). Another method to form GT2 hydrogel can be done by injecting GT2 phage solution into copper (II) chloride solution at 3-25mM (Best Cu^{2+} ion concentration is 20mM). The injection orientation and rate were used to change the morphology of hydrogels. To test water insolubility of GT2 hydrogel at different pH levels, 300µl of GT2 hydrogels were transferred into water in each glass vial. Each glass vial with hydrogel was shaken vigorously. Hydrochloric acid and sodium hydroxide were used to alter the pH level in each solution at a different pH.

2.2.3 Phage film formation (thin layer of Cu^{2+} ion-phage aggregations)

GT phage film and WT phage film were prepared by adding 5µl of 5mM $CuCl_2$ solution to each 50µl of GT2 phage solution (5.0 x 10^{13} phage/ml) and air-dried (2-3 hours) on the glass coverslips. A Zeiss NEON High Resolution Scanning Electron Microscope was used to visualize the arrangements of M13 phage in the film with Cu^{2+} ions. The aggregations of Cu^{2+} ions-GT2 phage were detected and recorded in the SEM images. WT phage was also processed in the same method to make a WT phage film as a control group.

2.2.4 Cu^{2+} ion-Phage Interaction

Agarose gel electrophoresis was performed for Cu^{2+} ion-phage complex in sol-gel status in TAE buffer. 20µl of GT2 phage solution (5.0 x 10^{13} phages/ml) was

placed in each well of the agarose gel with a different Cu^{2+} ion concentration (0mM – 120mM). With an applied electric current (at 30 voltages for 3-4 hours), negatively charged Cu^{2+} ion-phage migrated towards the positively charged electrode. Coomassie blue staining was performed to locate the migrated M13 phage coat proteins in the agarose gel. The agarose gel was treated in Coomassie ® R-250 staining solution for 3-5 minutes in a gentle shaking manner and treated in wash (destaining) buffer (10% acetic acid and 5% ethanol) overnight to remove blue staining in the background agarose gel (to clearly see the blue bands for phage coat proteins).

2.2.5 Evaluation of Hydrogel in mechanical properties

Torsional rheometry (Discovery Hybrid Rheometer, DHR-2) was used to measure the rheological behaviors of the hydrogels. Hydrogel samples were tested on the geometry, steel parallel plate (diameter 40 mm), under the conditions of a time sweep at 37 °C with a 700-750 μm gap, and frequency sweep at 0.5-40 rad/s. Storage modulus and loss modulus values were obtained to measure elasticity and viscosity of gel-like WT aggregate/GT2 hydrogel respectively. Hydrogel Mass (mg), water content ratio, gel fraction, and swelling ratio were measured after 50μl of WT and GT2 phage solution were added to Dulbecco Modified Eagle Media (DMEM) at 20mM Cu^{2+} ion. The mass of the hydrogels was taken by a scoopula to be measured after they were formed in the media with Cu^{2+} ion. Water content ratio was measured using ((wet hydrogel-dried hydrogel)/dried hydrogel). Gel fraction was measured by ((hydrogel mass/(phage mass + Cu^{2+} mass)*100). Swelling ratio was measured by ((swollen hydrogel-dried hydrogel)/dried hydrogel)

2.2.6 Copper Cytotoxicity

AlamarBlue® (Cell Viability Assay from Bio-Rad company) assay was used to measure copper cytotoxicity to two breast cancer cell lines (MCF-7, MDA-MB-231). MCF-7 and MDA-MB-231 cells were cultured in wells in 96-well plate (5-7 days) and treated at the concentrations of Cu^{2+} ions (50µM, 100µM, 200µM, 500µM, 1mM, 2mM, 5mM, and 10mM) and 50µl of GT2 hydrogel (created by inserting 50µl of GT2 phage solution (2×10^{14} phages/ml) into 20mM Cu^{2+} ion solution) was transferred to one of the sample groups to treat the cancer cells. The cell viability was measured at three different time points; Day 1, Day 2, and Day 3. The cell viability of the positive control (No Cu^{2+} ion nor GT2 hydrogel) was regarded as 100% for comparing to ones of the samples. Cell viability was confirmed and compared to breast endothelium cells ((MCF-10A), Normal cell control) by Live-Dead cell assay kit from Thermo Fisher (The LIVE/DEAD® Cell Imaging Kit).

2.2.7 Fluorescent Imaging of Nucleus and Actin Filaments in Breast Cancer cells (MCF-7 and MDA-MB-231)

DAPI (4′,6-diamidino-2-phenylindole) was used as a blue fluorescent stain to image DNA in the nucleus and Phalloidin (Alexa 488) was used to stain actin filaments in green for both MCF-7 and MDA-MB-231 breast cancer cell lines. MCF-7 and MDA-MB-231 cells were both cultured in different 96-well plates (5-7 days) and treated at the same concentrations of Cu^{2+} ions (50µM, 100µM, 200µM, 500µM, 1mM, 2mM, 5mM, and 10mM) and 50µl of GT2 hydrogel (created by inserting 50µl of GT2 phage solution (2×10^{14} phages/ml) into 20mM Cu^{2+} ion solution) was transferred to one of the sample groups to treat the cancer cells. DAPI-Phalloidin

images were merged for the same group by ImageJ software.

2.2.8 pH-Controlled Release of Copper-phage complex

ICP-AES method was used to detect and count the numbers of released Cu^{2+} ions from each GT2 hydrogel (50µl) in the media (3 samples per group) at a different pH (6.5 and 7.4) at different time points; 5 minutes, 30 minutes, 1 hour, 2 hour, 3 hour, 6 hour, 12 hour, 24 hour in Soil, Water, and Forage Analytical Laboratory (SWFAL) at Oklahoma State University. ICP-AES was also used to detect and count the numbers of released Cu^{2+} ions from GT2 hydrogel (300µl) in the media (pH 6.5) at body temperature (37 ^{o}C); 5 minutes, 30 minutes, 1 hour, 2 hour, 3 hour, 6 hour, 12 hour, 24 hour, 2 day, 5 day, 7 day, 14 day, and 30 day.

2.2.9 Cu^{2+}-GT2 phage complex Imaging

Confocal imaging and SEM imaging were performed to visualize the morphological changes of breast cancer cells. Leica SP8 Scanning Confocal/Multiphoton/FLIM Microscope was used to perform Confocal imaging in Confocal Microscopy/Advanced Light Imaging at the University of Oklahoma. Fixed breast cancer cells, previously fluorescently dyed in Phalloidin Alexa 488 (green) and DAPI (blue) were collected by micro-pipetting and viewed on the coverslip under the microscope. Zeiss NEON High Resolution Scanning Electron Microscope was used to make SEM images of critical point dried breast cancer cells (MCF-7 and MDA-MB-231 cell lines) on the coverslip (coverslips were 20 minute-sonicated and 75% ethanol treated and placed under 6 hour-UV radiation for sterilization) after 4% paraformaldehyde fixation and gradual ethanol dehydration process.

2.3 Results and Discussion

2.3.1 Cu²⁺-Engineered M13 phage Hydrogel

300μl of phage solution and 50μl of 20mM copper (II) chloride solution were mixed to form GT2 hydrogel. GT2 hydrogel showed a good water insolubility in a slightly weak acidic condition. GT2 hydrogel was elastic enough to be picked up by forceps. WT-M13 phage can also form a gel-like aggregate with Cu^{2+} ion. However, gel-like Cu^{2+} ion-WT aggregate (WT aggregate) shows less copper sensitivity and less aggregation of phage with Cu^{2+} ion. (Figure 2.3 and 2.4) Cu^{2+} ion can make a coordination bond to nitrogen in the N-terminus of peptides.[71-73] The coordination bond may induce the formation of gel-like structure of M13 phage. GT2 phage can potentially make stronger coordination bonds with more Cu^{2+} ions because of possible additional coordination bonds between Cu^{2+} ions and the threonine/arginine residues in the displayed peptide sequence (AGTGAGTGTGAGIRTG).[74-76]
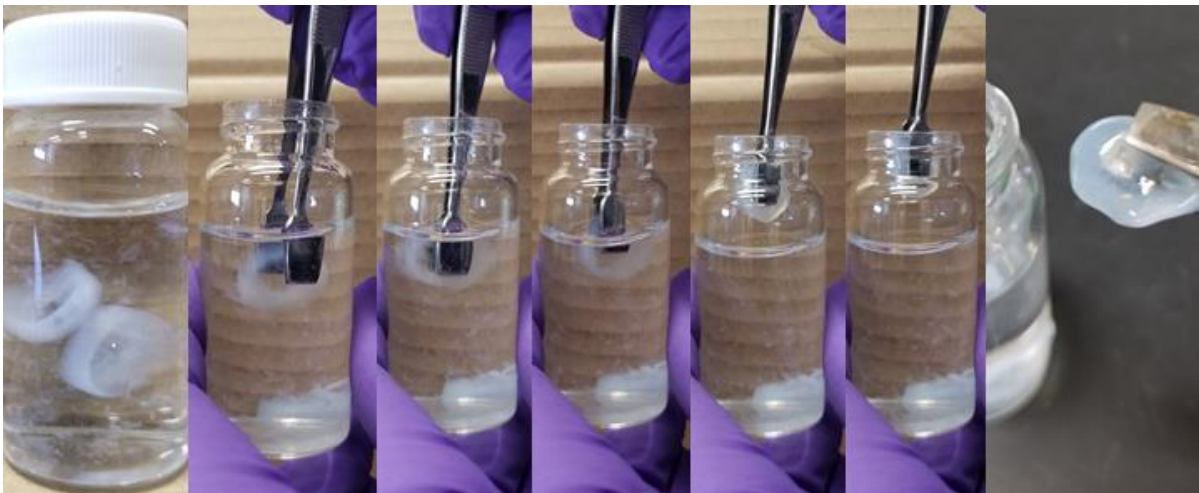

Figure 2.3 GT2 Hydrogel in water at pH 6, GT2 hydrogel shows a good water insolubility at a weak acidic condition. Viscoelastic GT2 hydrogel can be picked up by forceps.
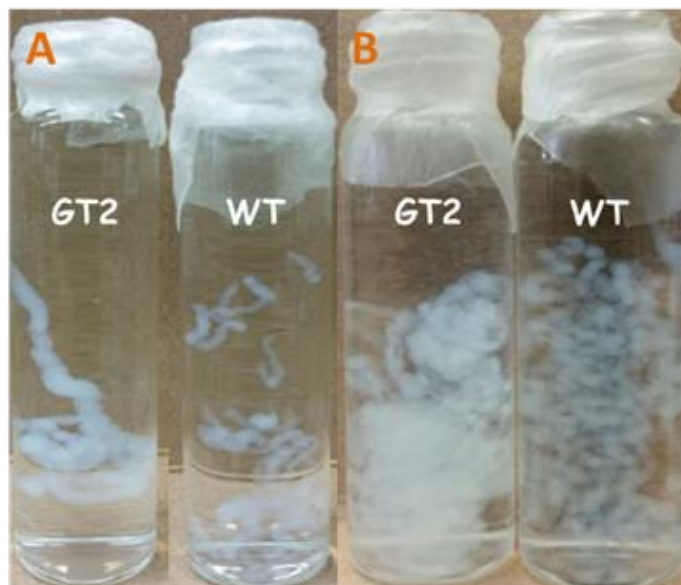
Figure 2.4 GT2 Hydrogel and WT aggregate at Cu^{2+} 20mM (A), 3mM (B), (A) Once GT2 hydrogel and WT aggregate were formed in Cu^{2+} solution, the glass vials were vigorously shaken. GT2 hydrogel shows a higher mechanical strength than that of WT aggregate. (B) GT2 hydrogel shows a higher aggregation than that of WT aggregate at a low Cu^{2+} ion concentration (3mM).

Water insolubility of GT2 hydrogel was tested at different pH levels. GT2 Hydrogel showed the best water insolubility at pH 5.7. GT2 hydrogel starts to dissolve completely in water out of the pH range (5 - 8). (Figure 2.5)
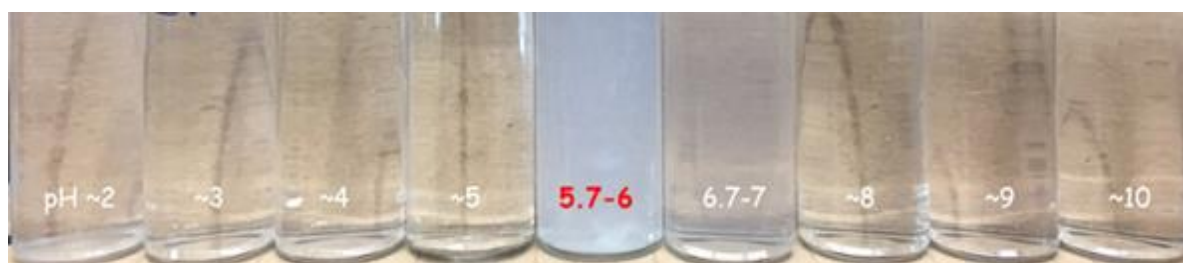

Figure 2.5 pH sensitivity of GT2 Hydrogel, GT2 hydrogel shows the best water insolubility at pH 6. GT2 hydrogel seems to be semi-soluble at pH 7. Beside the pH range of 5.7-7, GT2 hydrogel becomes soluble in water at the other pH levels.

2.3.2 Cu^{2+}-M13 phage interaction

The interaction between Cu^{2+} ions and M13 phage can be shown in SEM images. (Figure 2.6) GT2 phage aggregated massively with Cu^{2+} ions to form larger bundles and even created a micro-millimeter large bioorganic complex. However, WT phage showed less aggregation with Cu^{2+} ions than that of GT phage. Copper salts were found near Cu^{2+}-WT phage complex. (Figure 2.7) It suggests that WT phage did not fully interact with all the Cu^{2+} ions, therefore it could not form a large Cu^{2+}-WT phage complex. Cu^{2+} ion-GT2 phage aggregations appeared larger with phage bundling structures interacting with more Cu^{2+} ions. (Figure 2.8) To confirm the reactivity and interaction strength of GT2 phage and Cu^{2+} ions, GT2 phage was separately inserted into agarose gel for electrophoresis with a different Cu^{2+} ion concentration at each trial. GT2 phage showed a stronger interaction with Cu^{2+} ions and a small fraction of GT2 phage was migrated at high Cu^{2+} ion concentration conditions due to its aggregation and formation of larger bioorganic complexes for resisting migration in the agarose gel. Cu^{2+} ion-GT2 phage complexes were found in their initial positions at > Cu^{2+} ion 15mM with naked eye. (Figure 2.9), meaning GT2 phage still has a high affinity to Cu^{2+} ions below its critical concentration for hydrogel formation.
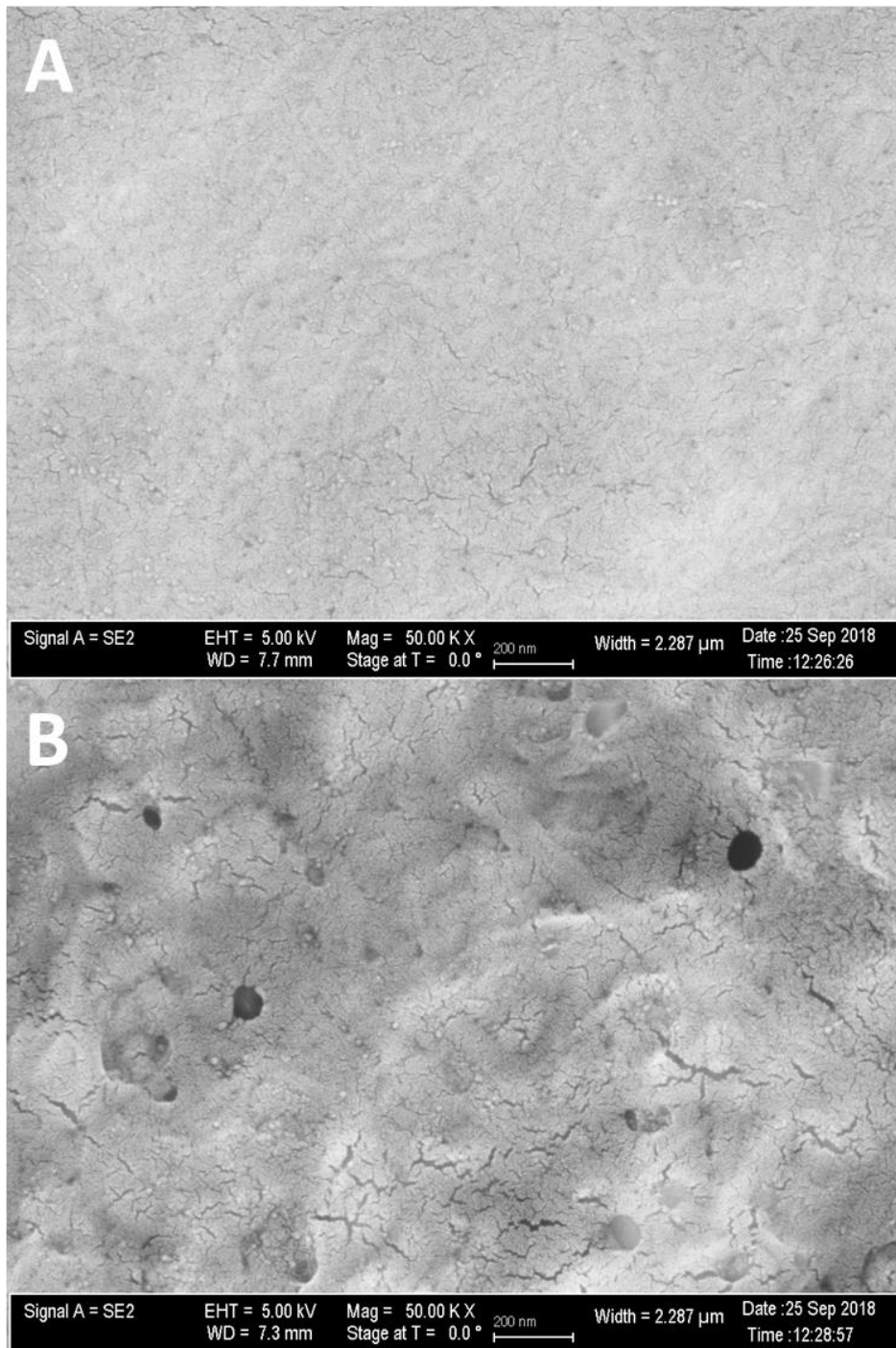
Figure 2.6 M13 phage alignments in the phage films, (A) WT phage shows isotropic arrangement in the film, (B) GT2 phage shows isotropic mesh network in the film, however in the thicker phage bundle form.

Figure 2.7 Cu^{2+} ion induced M13 phage aggregations in a thin layered film, (A) GT2 phage made one large aggregated layer with Cu^{2+} ions, (B) WT phage aggregations with Cu^{2+} ions were shown in a scattered pattern lacking a cross-linking property.

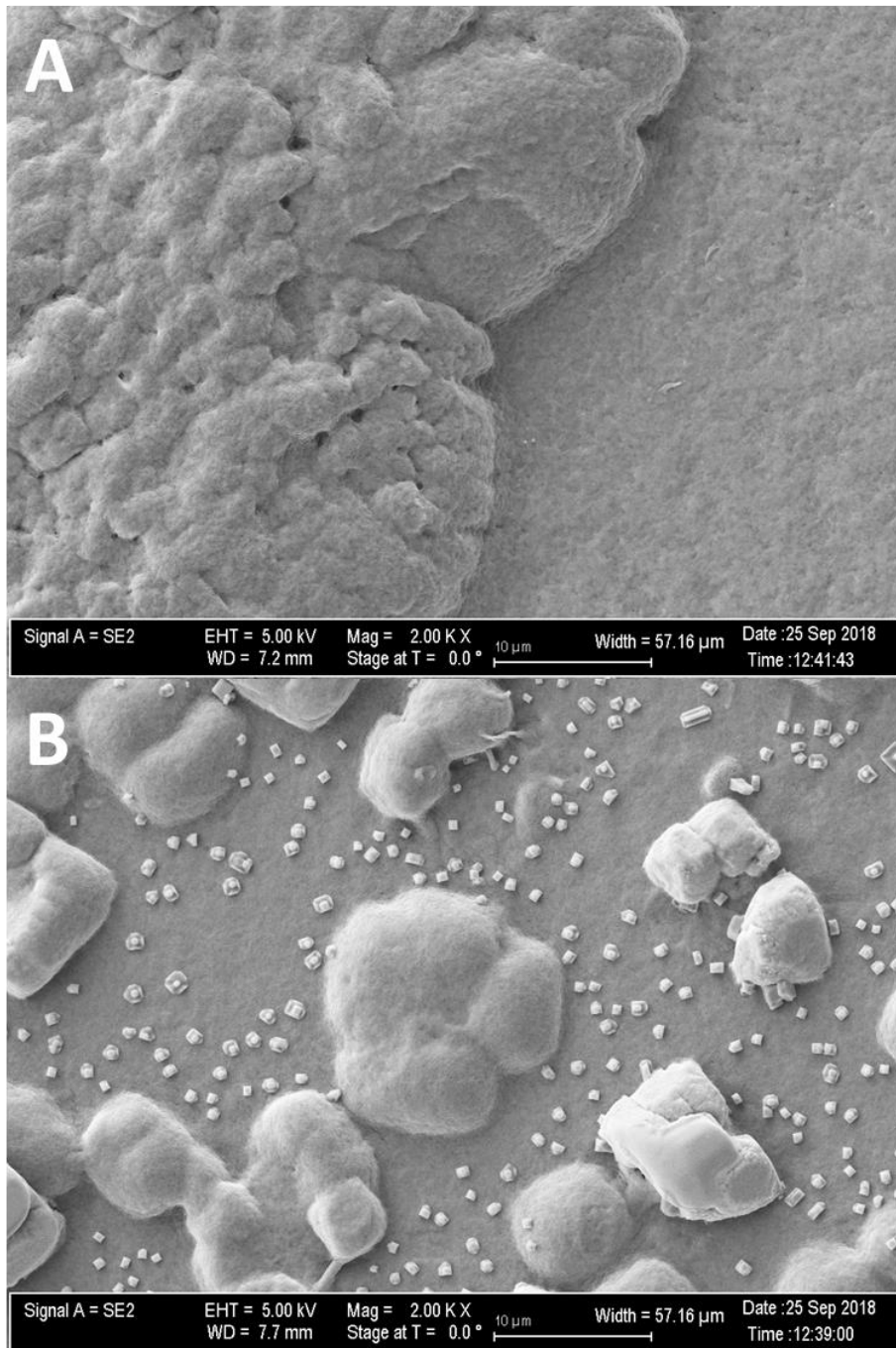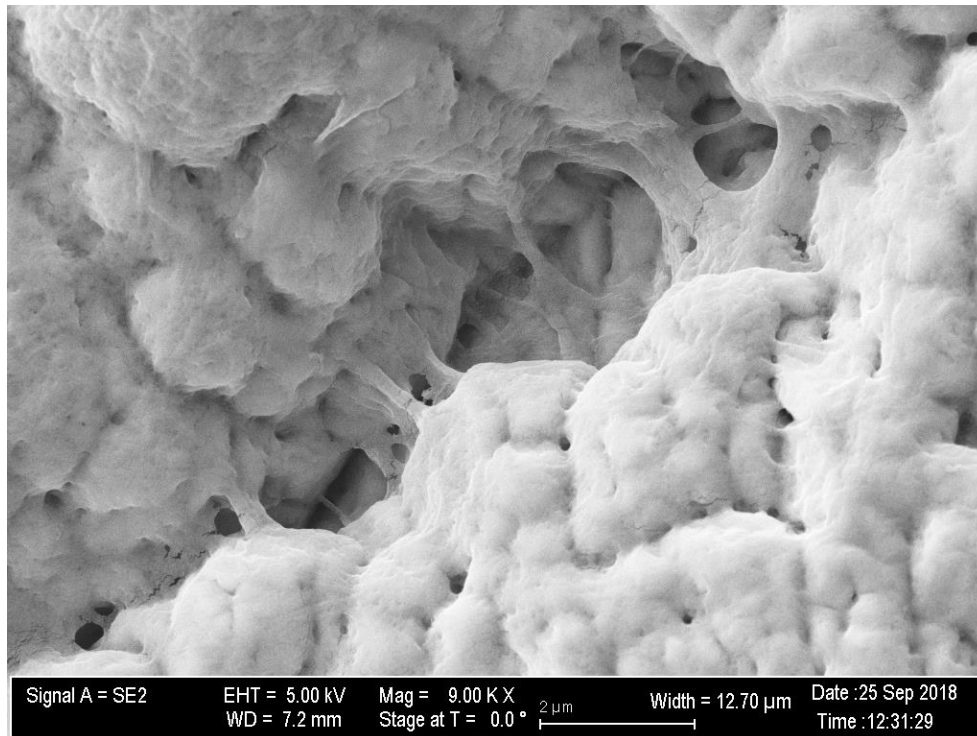**Figure 2.8** Cross-linking property of Cu^{2+} ion-GT2 phage, Cu^{2+} ion-GT2 phage bundles are strongly linked and bound together.

GT2 Phage (5.0×10^{13}/ml) in 10 ul ddH$_2$O

Top Down View (45°)

Top Down View (90°)

Cu 2+ ion

0 mM   120 mM

Figure 2.9 Electrophoretic mobility shift assay for Cu^{2+} ion-GT2 phage, when GT2 phage forms a complex with Cu^{2+} ions, the large complex resists to migrate in the agarose gel during the electrophoresis. At the higher Cu^{2+} ion concentration, the lower amount of GT2 phage proteins migrate.

2.3.3 Characteristics of Cu^{2+}-phage hydrogel/aggregate

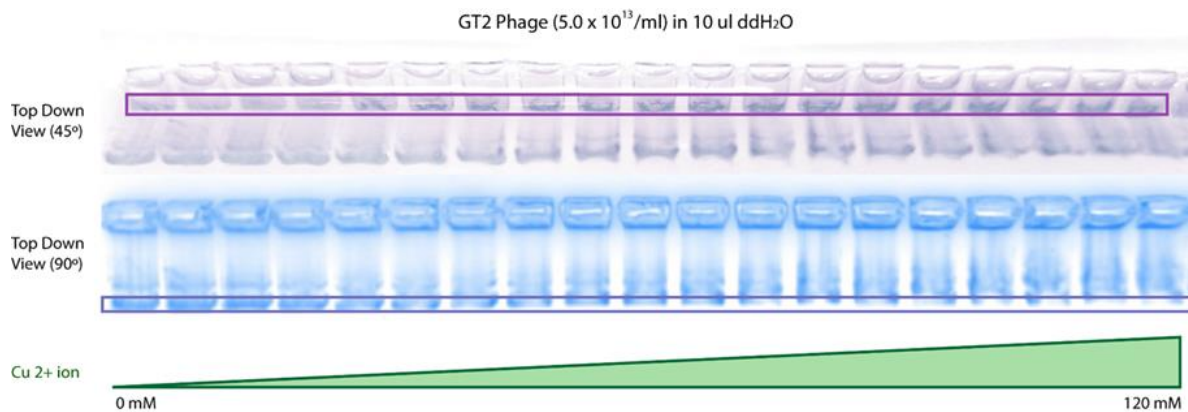Elastic GT2 hydrogel and gel-like WT aggregate can be formed in DMEM medium at 20mM Cu^{2+} ion. GT2 hydrogel and WT aggregate can be both picked up by forceps. However, after formation of hydrogel structure, GT2 hydrogel and WT aggregate decomposes slowly at pH 7.4 in the DMEM media. GT2 hydrogel shows superior hydrogel properties in water content ratio, gel fraction, and swelling ratio to those of WT aggregate. Because of higher water content/swelling/gel fraction properties of GT2 hydrogel, it has higher mass than WT aggregate under same conditions. This means when WT aggregate and GT2 hydrogel were formed in DMEM medium at 20 mM Cu^{2+} ion, GT2 phage could build a larger and heavier hydrogel from the equivalent amount of initial phage solution than ones in WT phage. (Figure 2.10) GT2 hydrogel also shows higher storage modulus and loss modulus than ones of WT aggregate. GT2 hydrogel is more elastic and viscous than WT aggregate. (Figure 2.11) This may suggest that, due to the higher water content and gel fraction, more GT2 phages were able to interact with a higher number of Cu^{2+} ions to form a polymer structure, absorbing a larger amount of water than WT phages do in WT aggregate formation with copper (II) ions. Due to the weak mechanical properties of WT aggregate to fulfill the requirements of good hydrogel unlike GT2 hydrogel, WT aggregate was not easily moveable with forceps.
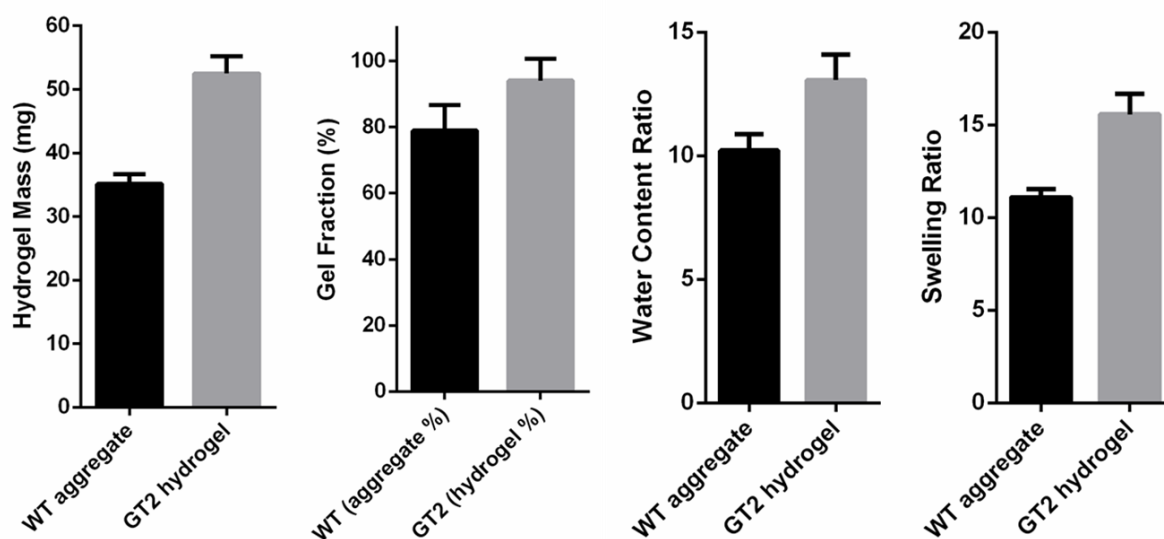
Figure 2.10 Hydrogel properties of GT2 hydrogel and WT aggregate, GT2 hydrogel mass is higher than one of WT aggregate because GT2 hydrogel has higher values in gel fraction, water content ratio, and swelling ratio.

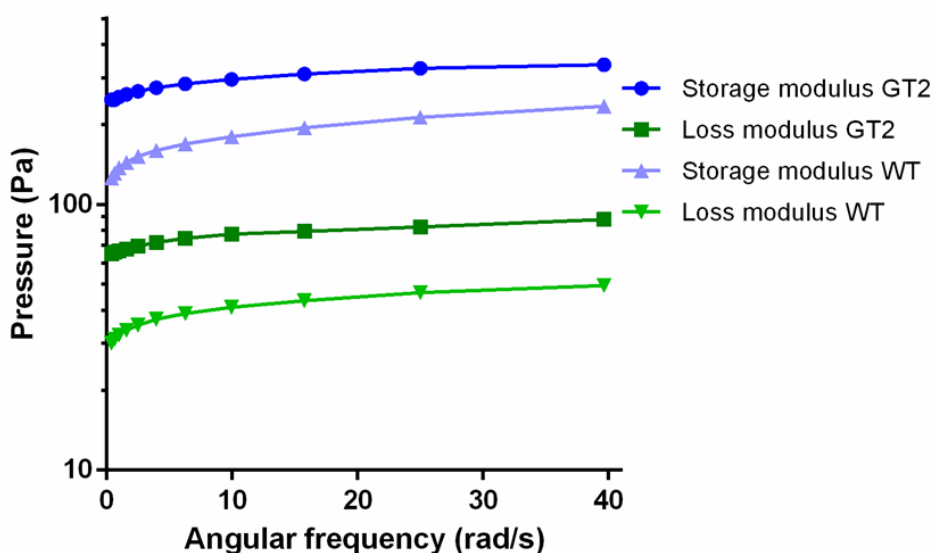**Figure 2.11** Mechanical properties of GT2 hydrogel and Gel-like WT aggregate, GT2 hydrogel has higher storage and higher loss modulus than ones of WT aggregate. It indicates that GT2 hydrogel is >2-fold more elastic and viscous (at certain angular

frequencies) than ones of WT aggregate. GT2 hydrogel is significantly higher in mechanical strength than WT aggregate. (storage modulus in blue and loss modulus in green)

2.3.4 Cytotoxicity of Cu^{2+} and GT2 Hydrogel on Breast cancer cells

Copper (II) ions show a high cytotoxicity on breast cancer cells (MCF-7 cell line) at a high concentration (20 mM) while neither GT2 phage nor PBS solution are toxic to MCF-7 cells after 72-hour incubation. However, addition of GT2 phage into MCF-7 cells in DMEM media at 20 mM Cu^{2+} ion showed a higher cytotoxicity than that of only Cu^{2+} ions. (Figure 2.12) To clarify the cytotoxicity of Cu^{2+} ions and GT2 hydrogel in detail, the cytotoxicity of Cu^{2+} ion at different concentrations and GT2 hydrogel on MCF-7 cells was measured at three different time points; Day 1, Day 2, and Day 3. At day 3, the growth of MCF-7 breast cancer cells was significantly repressed by >500µM Cu^{2+} ion or 50 µl of GT2 hydrogel. (Figure 2.13) Live/Dead cell imaging results also support the cell viability data. (Figure 2.14) The copper toxicity on MDA-MB-231 in the same conditions was also obtained. The growth of MDA-MB-231 was significantly suppressed by >500µM Cu^{2+} and GT2 hydrogel. GT2 hydrogel showed a lower cytotoxicity on MDA-MB-231 cells at day 1 and day 2 than those on MCF-7 cells. (Figure 2.15 and Figure 2.16) The copper toxicity on MCF-10A, Breast endothelium cells (normal cell control), in the same conditions was also attained to compare to those of MCF-7 and MDA-MB-231. Surprisingly, the growth of MCF-10A was suppressed by >1 mM Cu^{2+} and GT2 hydrogel. GT2 hydrogel showed a lower cytotoxicity on MCF-10A cell line than that on MCF-7 and MDA-MB-231 cell lines. (Figure 2.17) Interestingly, the cell growths (MCF-7, MDA-MB-231, and MCF-10A)

were highly inhibited by 50µl of GT2 hydrogel as they were at high Cu^{2+} ion concentration despite of that GT2 hydrogel can only release a low amount of Cu^{2+} ions, creating a low Cu^{2+} ion concentration (~178µM) in the DMEM media. Additionally, as proven in Figure 2.12, M13 phage is non-toxic to cells.[77] It proposes that strong inhibition of breast cancer cell growth can only occur with the presence of both Cu^{2+} ions and GT phages.
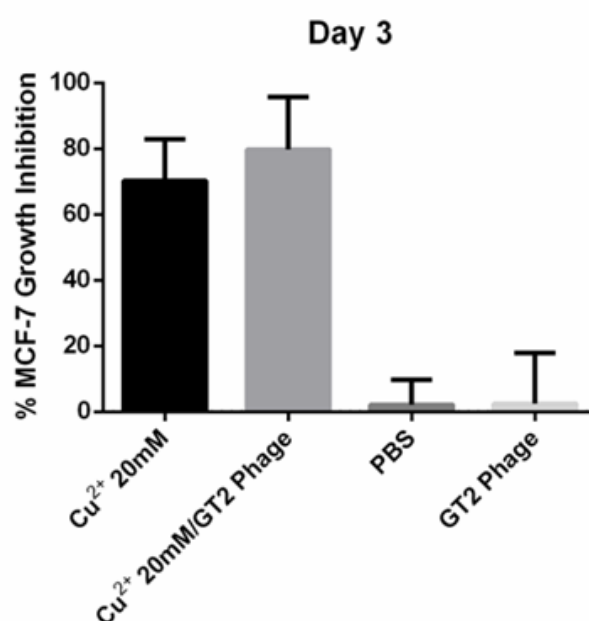

Figure 2.12 Growth Inhibition (%) of Cu^{2+} ion and GT2 phage, Copper (II) ions inhibit the MCF-7 cell growth significantly at a high concentration. GT2 phage (50µl), itself, does not inhibit the growth of MCF-7 cells. However, GT2 phage shows a synergetic cytotoxicity on MCF-7 cells with Cu^{2+} ions.
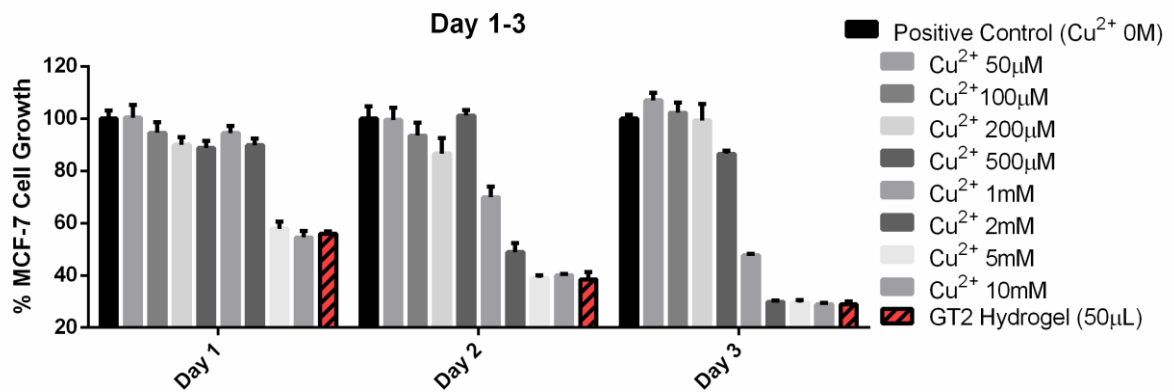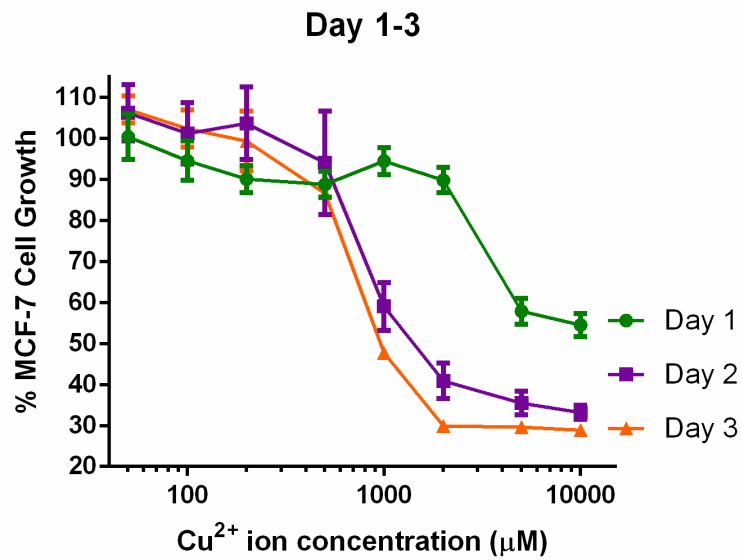
Figure 2.13 MCF-7 cell growth on different concentrations of Cu^{2+} ion and GT2 hydrogel, MCF-7 cancer cell growth was suppressed by > 5mM Cu^{2+} ion at Day 1, 1mM Cu^{2+} ion at Day 2 and 3, MCF-7 cancer cell growth was suppressed by GT2 hydrogel at all Day 1, 2, and 3 (50 μl)

Figure 2.14 Live/Dead MCF-7 Cell Imaging, Live cells were stained in green color and dead cells were stained red color after 3-day incubation.

Figure 2.15 MDA-MB-231 cell growth on different concentrations of Cu^{2+} ion and

GT2 hydrogel, the growth of MDA-MB-231 Breast cancer cell is significantly suppressed by >500µM Cu^{2+} ion or 50µl of GT2 hydrogel.

Figure 2.16 Live/Dead MDA-MB-231 Cell Imaging, Live cells were stained in green color and dead cells were stained red color after 3-day incubation.
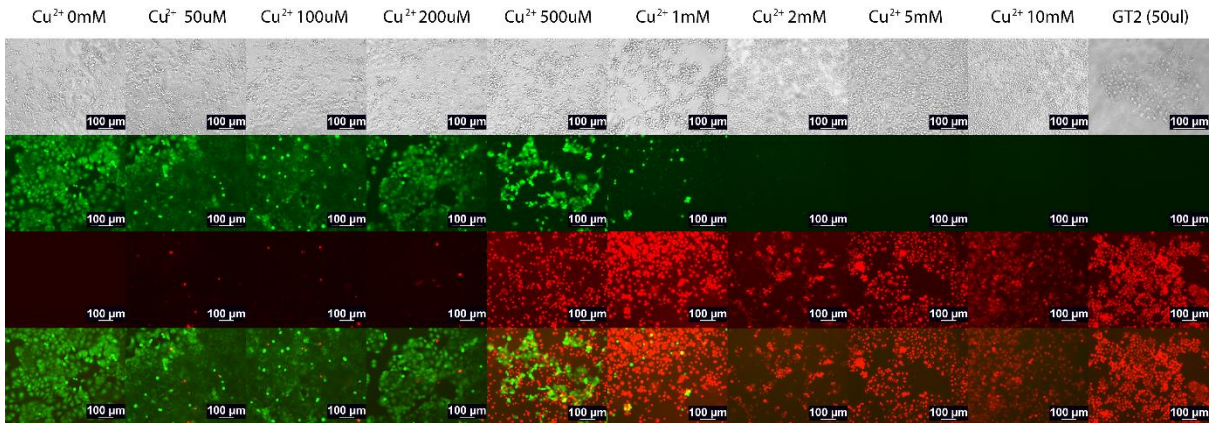

Figure 2.17 Live/Dead MCF-10A Cell Imaging, Live cells were stained in green color and dead cells were stained red color after 3-day incubation.

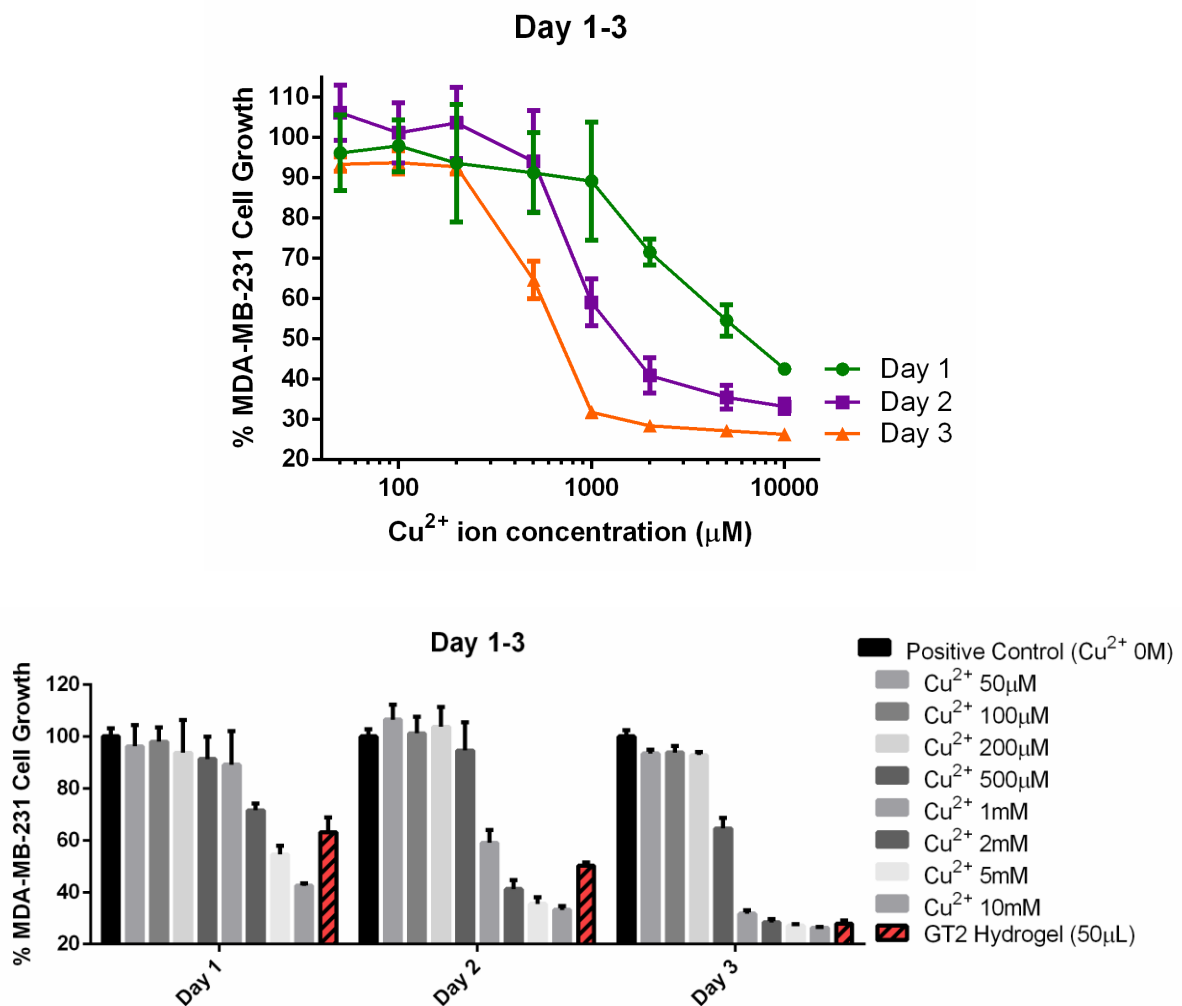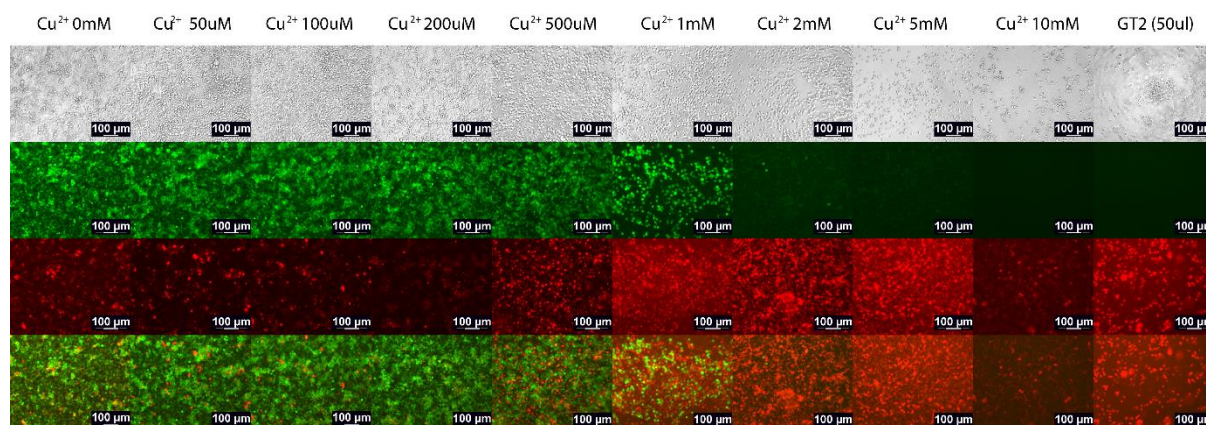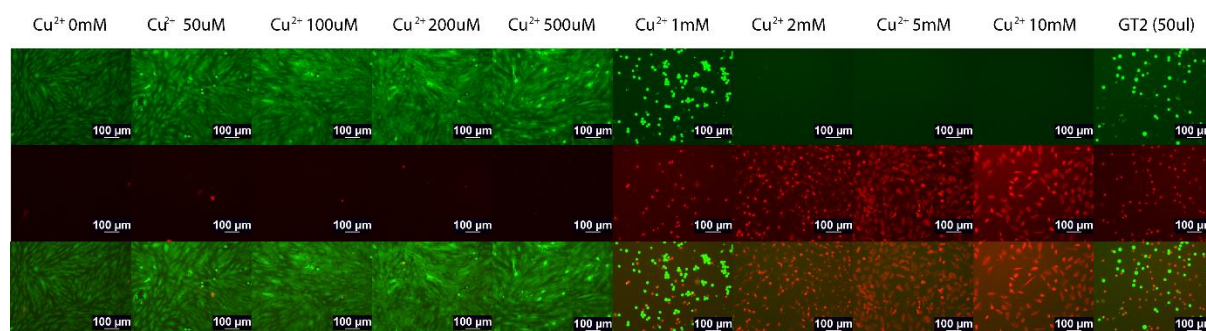## 2.3.5 Nucleus and Actin Filaments in MCF-7 and MDA-MB-231 with Cu^{2+} and GT2 hydrogel

MCF-7 cells were immunofluorescent stained in DAPI and phalloidin (Alexa 488) to locate and visualize DNA (in the nucleus) and actin filaments in MCF-7 cells

after 3-day incubation in Cu^{2+} ion at various concentrations and 50μl of GT2 hydrogel. MCF-7 cells (at <1mM Cu^{2+} ion) did not show any noticeable change in the size of shape of nucleus and actin filaments, compared to ones of MCF-7 cells in positive control except those at 500μM Cu^{2+}. The size of the nucleus and the actin filament network in MCF-7 cells at 500μM Cu^{2+} became larger than that in the positive control. However, actin filaments in MCF-7 cells were significantly contracted at >1mM Cu^{2+}, compared to those in the positive control (Figure 2.18) MDA-MB-231 breast cancer cells were also immunofluorescent stained in DAPI and phalloidin (Alexa 488) to locate and visualize DNA (in the nucleus) and actin filaments in MDA-MB-231 cells after 3-day incubation in Cu^{2+} at various concentrations and 50μl of GT2 hydrogel. MDA-MB-231 cells (at <1mM Cu^{2+} ion) did not show any noticeable change in the size and shape of nucleus and actin filaments, compared to those of MCF-7 cells in the positive control. However, actin filaments in MDA-MB-231 cells were significantly contracted at >1mM Cu^{2+}, compared to those in the positive control (Figure 2.19) In both MCF-7 and MDA-MB-231 cells, the actin filaments are strongly inhibited with the presence of >1mM Cu^{2+} ion and 50μl of GT2 hydrogel. It is possible that actin filaments are damaged by oxidative stress from added Cu^{2+} ions in the medium. An excess of Cu^{2+} ions can cause oxidative stress that mainly targets actin monomers in all living organism in water-based medium. In the presence of Cu^{2+} ions, hydroxyl radicals can oxidize most of amino acid residues (such as K, R, P, and T) in protein. Hydroxyl radical can steal a hydrogen on a carbon in the side chain of amino acid residue in actin protein. After hydrogen abstraction of hydroxyl radicals, Cu^{2+} ion can accept the lone pair of a radical carbon. A radical carbon on the side chain of the protein may be later led to a possible carbonylation pathway (carbon radical

44

carbonylation). The modification of actin monomer structure may destabilize the actin polymerization. It may also cause a serious problem for actin monomers to be re-formed in actin filaments. Eventually, oxidative stress (from Cu^{2+} ions) can induce many biochemical processes that suppress a stable formation of actin filaments.[78-79]

Figure 2.18 DAPI and Phalloidin staining of MCF-7 cells after 3-day incubation with GT2 hydrogel treatment besides various Cu^{2+} ion concentrations, DNA in the nucleus and actin filaments (MCF-7) were stained in DAPI and phalloidin (Alexa 488) respectively at various Cu^{2+} concentrations and GT2 hydrogel. Nucleus in MCF-7 cells seems to increase at <500μM Cu^{2+} ion and decreased at >500μM Cu^{2+} ion. The signs of actin filament activity/expression in green color is inhibited at >1mM Cu^{2+} ion and GT2 hydrogel (50μl)
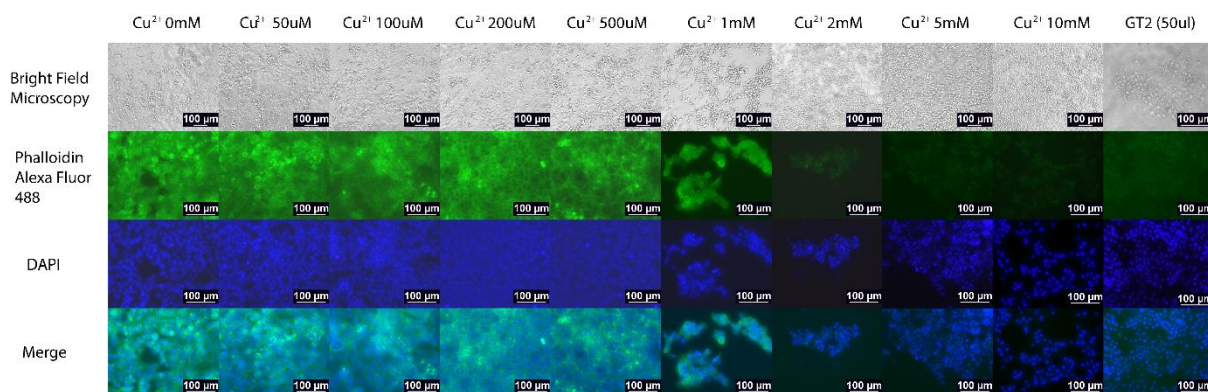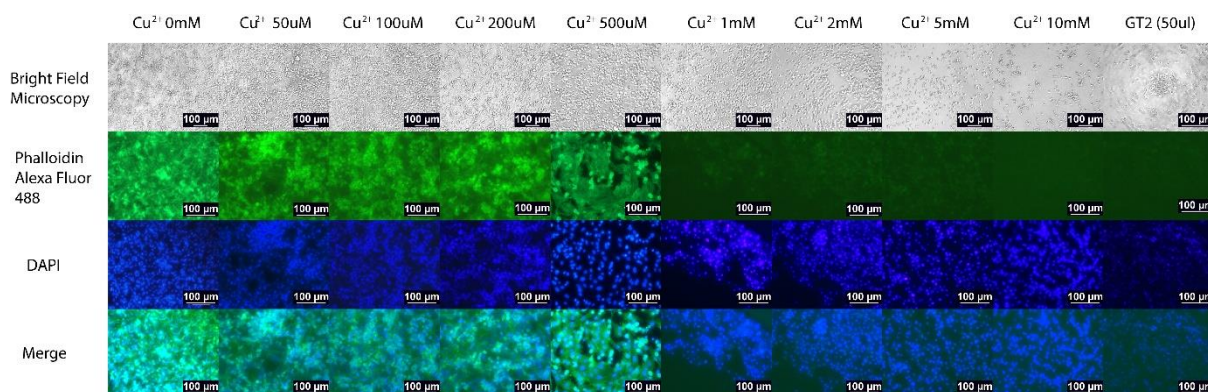

Figure 2.19 DAPI and Phalloidin staining of MDA-MB-231 cells after 3-day incubation with GT2 hydrogel treatment besides various Cu^{2+} ion concentrations,

DNA in the nucleus and actin filaments (MDA-MB-231) were stained in DAPI and phalloidin (Alexa 488) respectively at various Cu^{2+} concentrations and GT2 hydrogel. Nucleus in MCF-7 cells seems to increase at <500µM Cu^{2+} ion and decreased at >500µM Cu^{2+} ion. The signs of actin filament activity/expression in green color is inhibited at >1mM Cu^{2+} ion and GT2 hydrogel (50µl)

2.3.6 pH-Controlled Release of Copper-phage complex

GT2 hydrogel (50 µl) decomposition was observed in PBS solution (pH 7.4) during 1-5 days at room temperature (20 °C). GT2 hydrogel was slowly decomposed over 5 days. Stimulatingly, released Cu^{2+}-phage complex was seen in the form of a haze at the bottom of the glass vial by naked eye. At day 5, GT2 hydrogel was almost completely decomposed and completely dissolved in PBS solution following one vigorous shaking. (Figure 2.20) The decomposition rate of GT2 hydrogel in DMEM was also tested. GT2 hydrogel disappeared in DMEM at pH 7.4 (room temperature) rapidly (within 5 minutes) to the naked eye. However, GT hydrogel seemed to decompose slowly at pH 6.5 in DMEM (room temperature). (Figure 2.21) Based on ICP-AES data, Cu^{2+} ions were released completely in 12 hours from GT2 hydrogel in DMEM at pH 7.4 (room temperature). It might suggest that GT2 hydrogel can be fully dissolved in 12 hours at pH 7.4. Even if GT2 hydrogel disappears in 5 minutes in DMEM at pH 7.4, GT2 hydrogel was still not fully dissociated in 12 hours. This might indicate that GT2 hydrogel becomes transparent within 5 minutes, slowly dissociating over 12 hours. GT2 hydrogel decomposed at a slow rate at pH 6.5. (Figure 2.22) GT2 hydrogel showed a slower rate of releasing Cu^{2+} ions at pH 6.5 and at body temperature (37 °C). This might also indicate that GT2 hydrogel

decomposes slowly at 37 °C. (Figure 2.23) The controlled Cu^{2+} ion release of GT2 hydrogel was maintained over 1 month. (Figure 2.24) In a longer time period, GT2 hydrogel can release and decompose slowly at pH 6.5 at 37 °C.
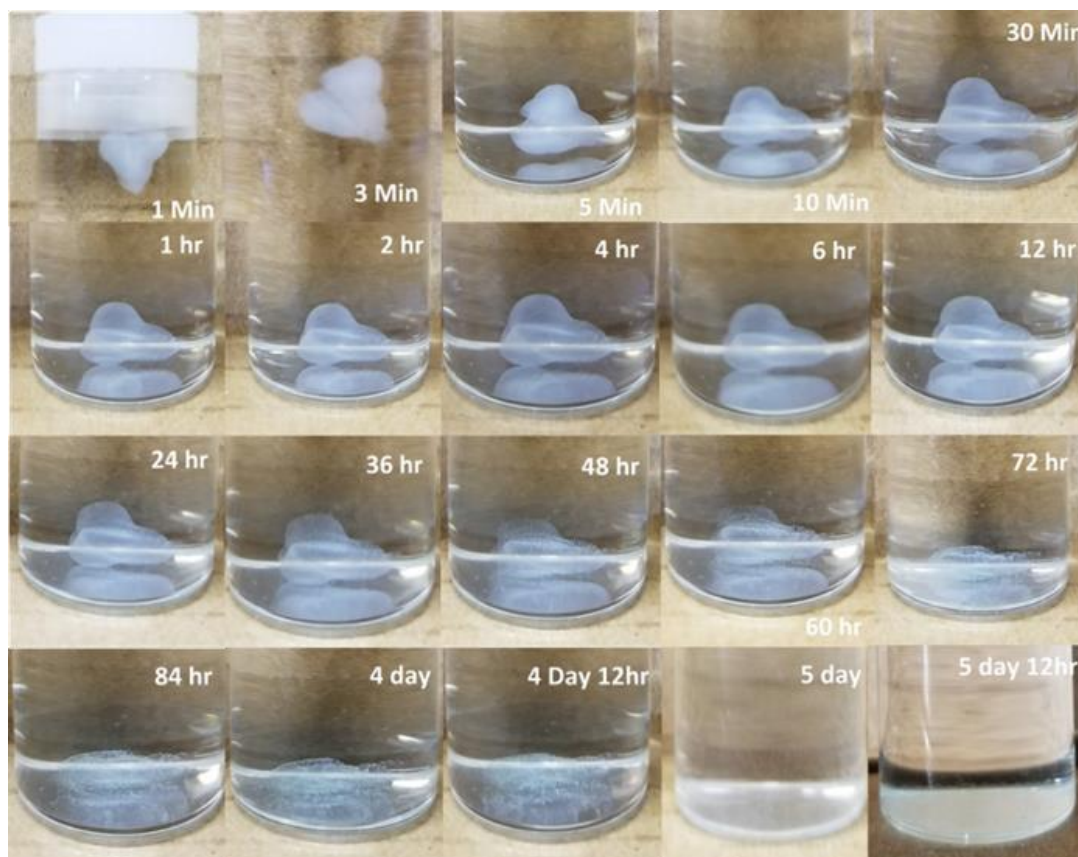
Figure 2.20 Decomposition of GT2 hydrogel at pH 7.4, The images of GT hydrogel in PBS solution at (pH 7.4) were obtained at different time points (1 min, 3 min, 5 min, 10 min, 30 minutes, 1 hour, 2 hour, 4 hour, 6 hour, 12 hour, 24 hour, 36 hour, 48 hour, 60 hour, 72 hour, 84 hour, 4 day, 4 day 12 hour, 5 day, and 5 day 12 hour)
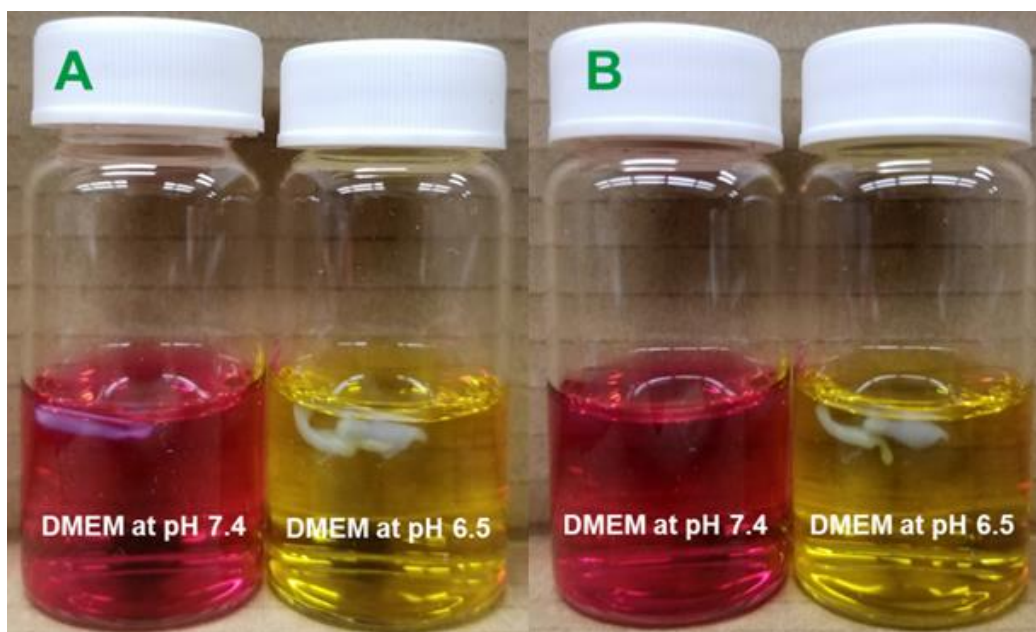
Figure 2.21 Decomposition of GT2 hydrogel in DMEM at two different pH, GT2 hydrogel disappear in DMEM less than 5 minutes at pH 7.4 by naked eyes. However, GT2 hydrogel disappear slowly at pH 6.5, compared to the one at pH 7.4 to the naked eye.
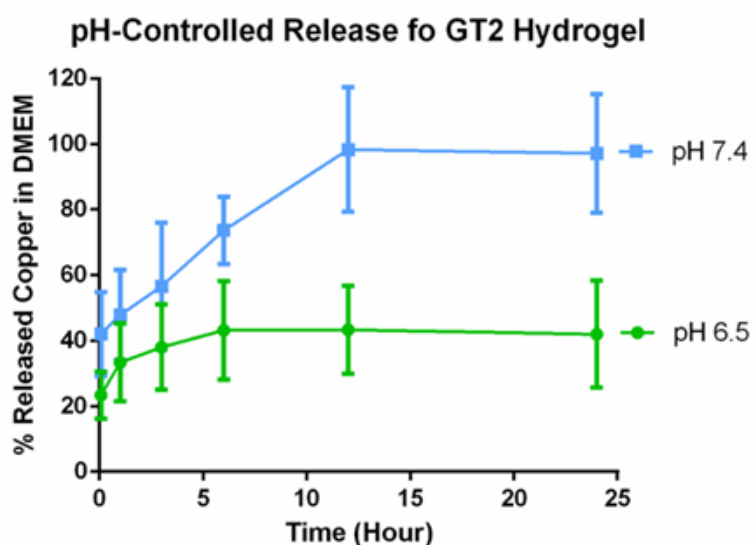
Figure 2.22 Decomposition of GT hydrogel in DMEM at pH 6.5 and 7.4 (20 °C), GT2 hydrogel decomposed faster at pH 6.5. GT2 hydrogel was completely decomposed in 12 hours.

Figure 2.23 GT2 hydrogel decomposition at pH 6.5 in hours (37 °C), GT2 hydrogel decomposed slower at body temperature (37 °C)

Figure 2.24 GT2 hydrogel decomposition at pH 6.5 in days (37 °C), GT2 hydrogel decomposed slower at body temperature (37 °C) for a longer period.

2.3.7 Encapsulation of Breast cancer cells by Cu^{2+}-Phage complex

In confocal images of MCF-7 and MDA-MB-231 cells with GT2 hydrogel, filament-like structures (located on the surface of both MCF-7 and MDA-MB-231 cells) were not identified due to the low resolution of the images. SEM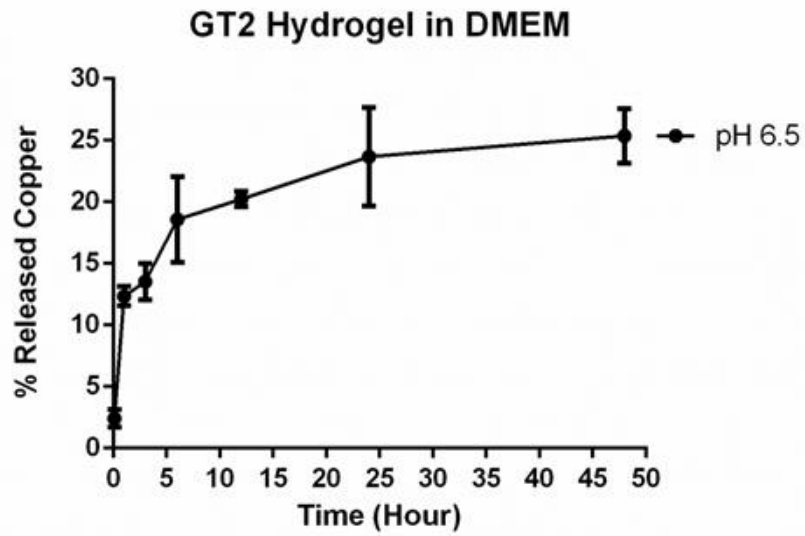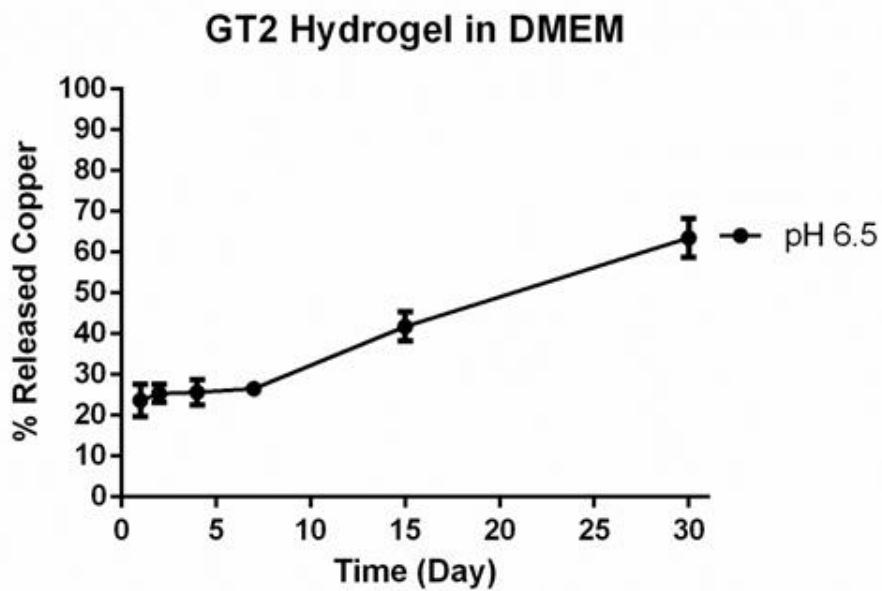 imaging was used to create the images of breast cancer cells at a higher resolution. (Figure 2.25, Figure 2.26, and Figure 27) In the SEM images (Figure 2.25 g,h, 2.26 g,h, and Figure 27), MCF-7 and MDA-MB-231 cells (previously treated with GT2 hydrogel, Cu^{2+}-phage complex) were surrounded by Cu^{2+}-GT2 phage complex. However, GT2 phages were not found on the surface of the breast cancer cells without Cu^{2+} ions. It suggests that only when GT2 phages are loaded with Cu^{2+} ions (Cu^{2+}-) can GT2 phage complex have a high affinity to both MCF-7 and MDA-MB-231 cell (membrane). Cu^{2+}-GT2 phage complex enclosed breast cancer cells may suffer from poor oxygen and nutrient absorption, and eventually led to apoptosis pathway.[80-82] Cu^{2+}-GT2 phage complex confinement might cause even a more serious damage for the breast cancer cells by preventing them from interacting and responding to ECM and signal proteins, essential for their survival in *in vivo* study.[83-84] It also suggests that surrounding the cancer cell with Cu^{2+} ion-GT2 phage complex may induce an effective and efficient delivery of Cu^{2+} ions into the cell[85], and eventually it also lead the cells to apoptosis pathway due to Cu^{2+} ion-induced oxidative stress.
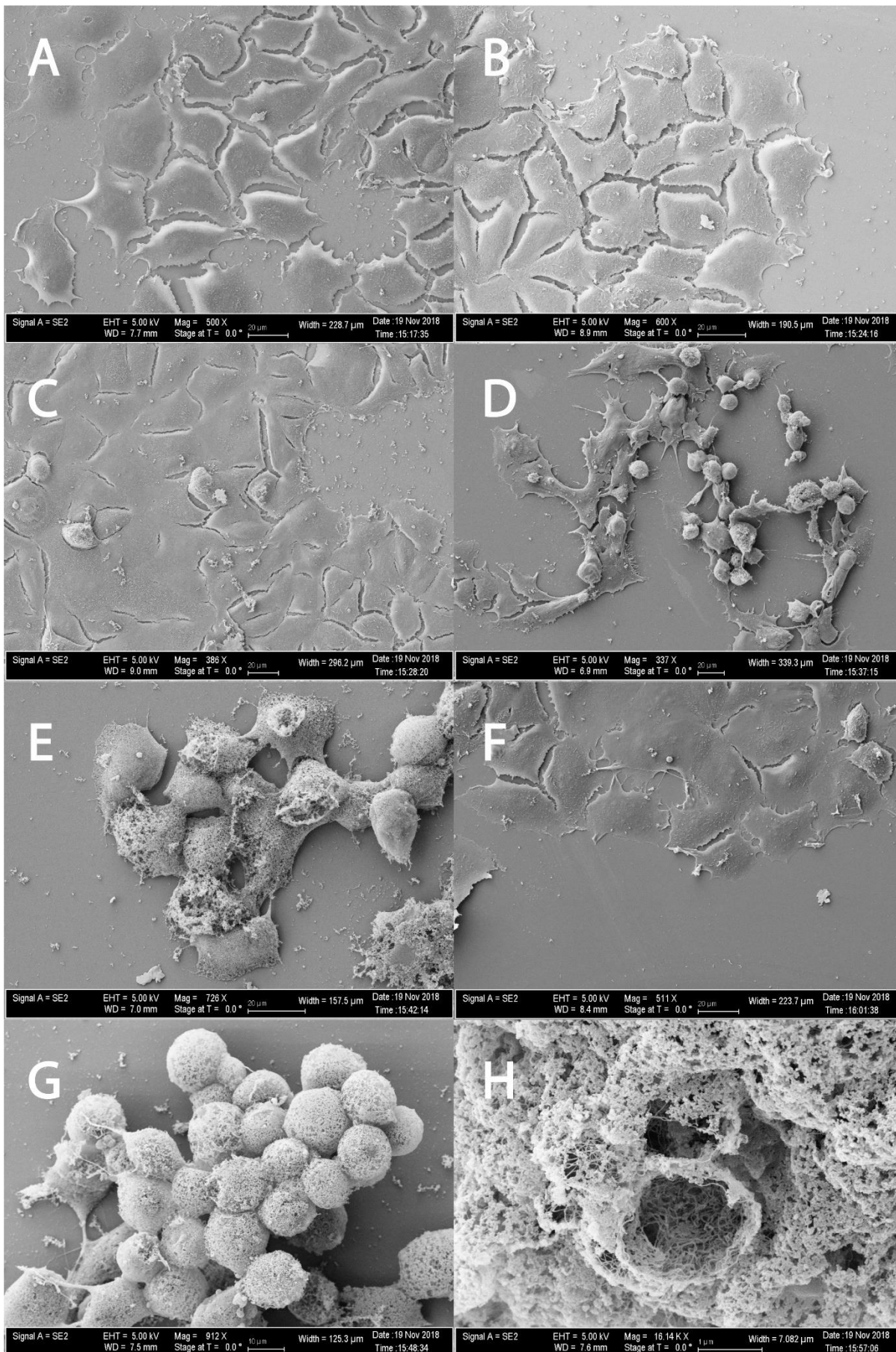
Figure 2.25 MCF-7 SEM images, (A) MCF-7 at 0µM Cu^{2+} ion, (B) MCF-7 at 50µM Cu^{2+} ion, (C) MCF-7 at 200µM Cu^{2+} ion, (D) MCF-7 at 1mM Cu^{2+} ion, (E) MCF-7 at 5mM Cu^{2+} ion, (F) MCF-7, treated with 50µl of GT2 phage, (G) MCF-7, treated with 50µl of GT2 hydrogel, (H) a MCF-7 cell (cell surface), treated with 50µl of GT2 hydrogel at higher magnification.
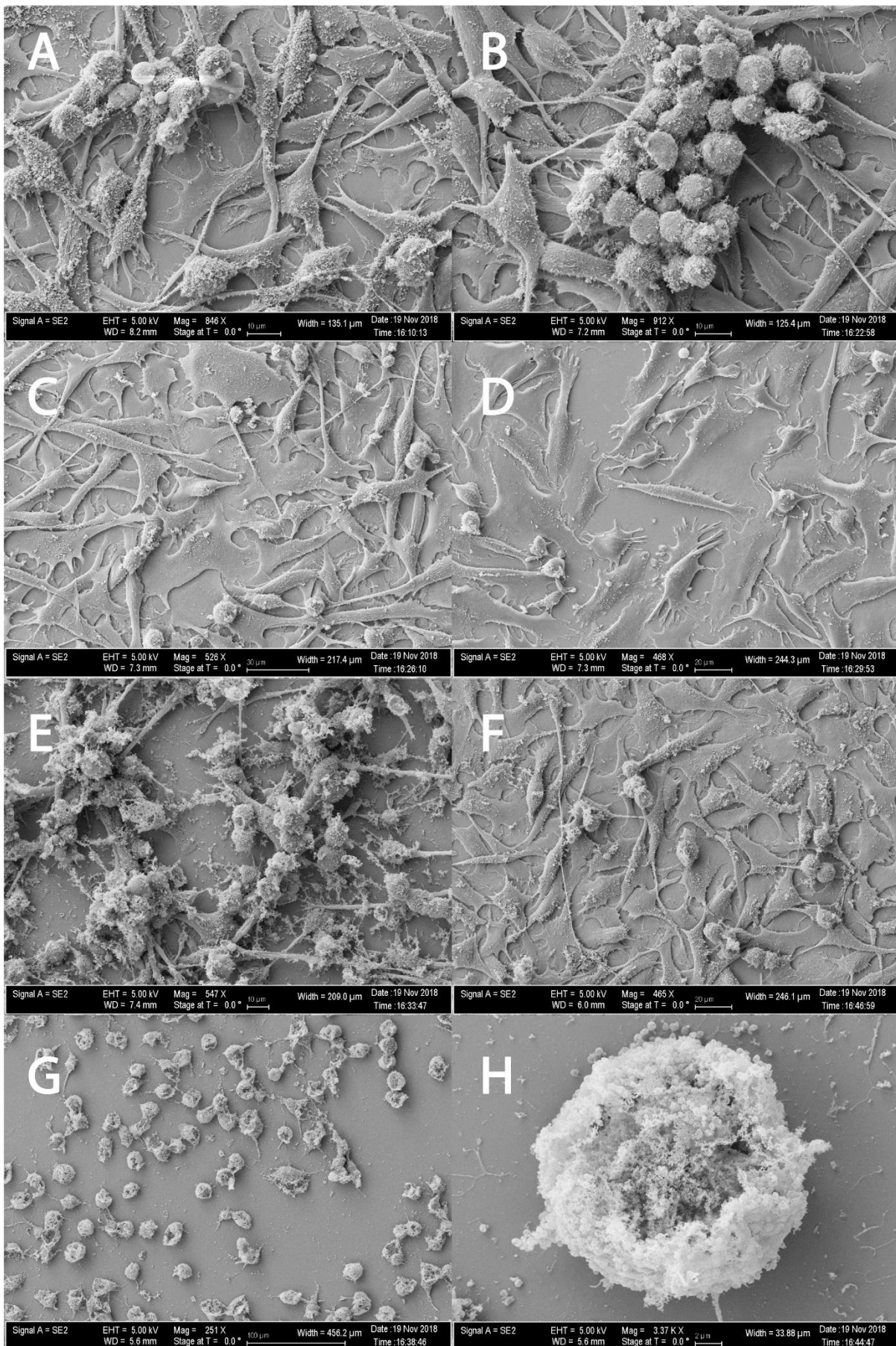
Figure 2.26 MDA-MB-231 SEM images, (A) MDA-MB-231 at 0µM Cu^{2+} ion, (B) MDA-MB-231 at 50µM Cu^{2+} ion, (C) MDA-MB-231 at 200µM Cu^{2+} ion, (D) MDA-MB-231 at 1mM Cu^{2+} ion, (E) MDA-MB-231 at 5mM Cu^{2+} ion, (F) MDA-MB-231, treated with 50µl of GT2 phage, (G) MDA-MB-231, treated with 50µl of GT2 hydrogel, (H) a MDA-MB-231 cell, treated with 50µl of GT2 hydrogel at higher magnification.

Figure 2.27 MCF-7/MDA-MB-231 SEM images at high magnifications, ((A), (B)) MDA-MB-231 covered with Cu^{2+} ion loaded GT2 phages, ((C), (D)) MCF-7 covered with Cu^{2+} ion loaded GT2 phages

2.4 Conclusion

Copper seems to be an important cell growth factor particularly for cancer cells due to its role as an inducer of angiogenesis and several important growth mechanism boosters. However, copper overaccumulation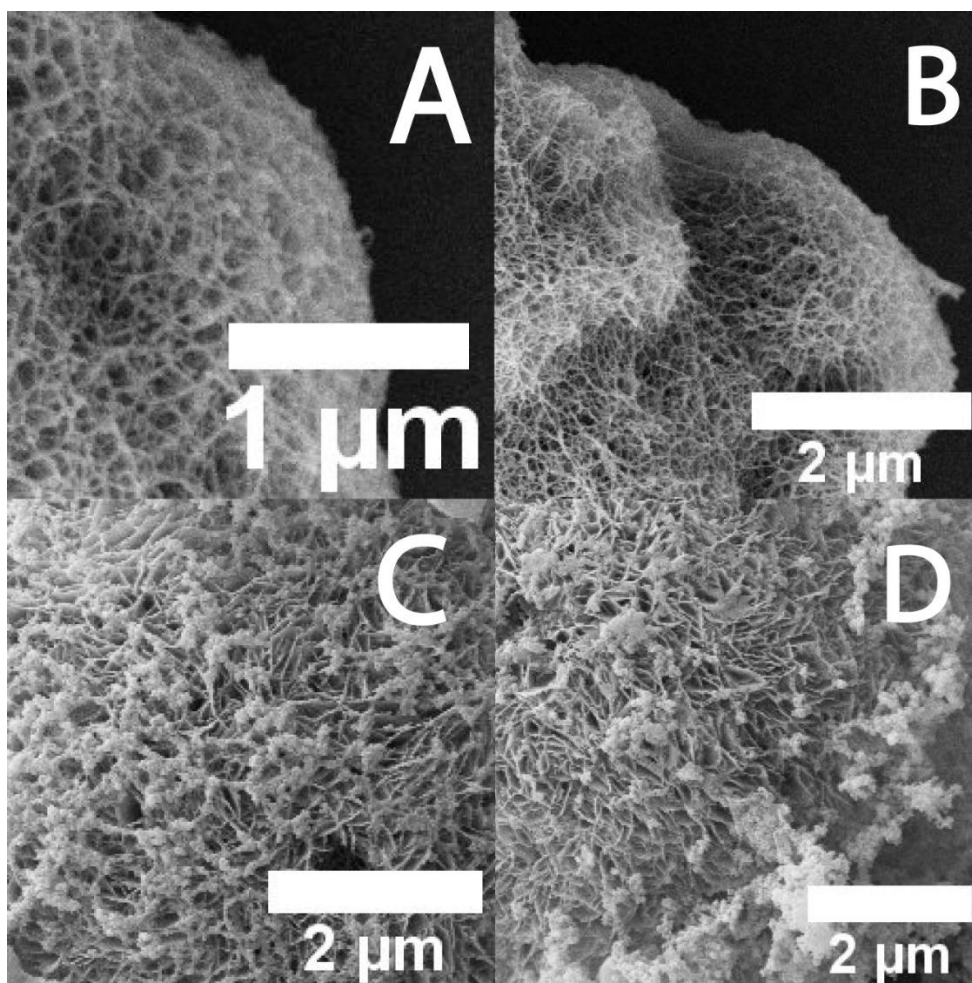 causes serious problem in the growth of breast cancer cell lines (MCF-7 and MDA-MB-231). GT2 hydrogel shows the release of the copper-phage complex in a pH-dependent manner at body temperature. Released (strongly linked) Cu^{2+} ion-GT2 phage complexes can surround the breast cancer cell membranes and eventually kill the cancer cells (MCF-7 and MDA-MB-231). This pH-controlled release mechanism may enable us to treat and kill cancer cells specifically in the body over a long time period (>1 month). Due to the cell confinement of Cu^{2+} ion-GT2 phage complex and direct delivery of Cu^{2+} ion into cytoplasm of cells, breast cancer cells may die from the lack of oxygen and nutrients and oxidative stress. It may also cause a synergetic effect on killing breast cancer cells with their lack of interaction and response to ECM and signal proteins, critical for their growth and survival in *in vivo* study.[86] Eventually, Cu^{2+} ion-bioorganic complex-surrounding mechanisms may lead cancer cells to the apoptosis pathway more efficiently and effectively. (Figure 2.28) This new novel method might brighten up the field of cancer therapeutic studies in the future, and it can also potentially be utilized for other studies such as the measurement of copper ion concentrations in water-based solutions and the removal of toxic organic complex as well as many other Cu^{2+} ion related organic chemical studies.

Figure 2.28 Schematic Image of overall process of building a breast cancer therapeutic Cu^{2+} ion-Phage hydrogel

Chapter 3. Gold (III) ion-M13 Phage Based Hydrogel Formation for Potential Green Biochemical Synthesis of Fine Gold Nanoparticles

3.1 Introduction

Nanotechnology has been advanced rapidly for many scientific researches such as the nanoprobes development for detecting metal ions, RNA, peptides or proteins so on.[87-89] Nanoparticles with the appealing properties have dominated the area of sensing and detective device development.[90-91] Particularly, sensors with gold nanoparticles (AuNPs) have been studied and advanced by a lot of great researchers using the AuNPs' feasible applicability with the high surface to volume ratio and fascinating optical properties of AuNPs enabling highly sensitive and selective detection.[92-94]

Especially, small sized Au NPs is more attractive for biomedical use in sensing, cellular imaging, drug delivery, and cancer therapy, chemical analysis, catalysis, electronics, and nonlinear optical processes.[95-97] The unique plasmon and optical properties of AuNPs significantly are subject to its morphological and physiological characteristics. Its size, shape and aggregation state determine the optical proprieties that can be fine-tuned by the appropriate synthesizing and stabilizing agent(s). Colloidal AuNPs normally show red or pink color and when it aggregates, its color changes to purple-blue.[87] Bottom-up assembly of AuNPs in the efficient way with an elegant control at the nanoscale is one of the key ambitions of nanoscience and nanotechnology.[98-100] AuNPs ,as metal nanomaterials, can also have the flexibility of surface modifications and the physicochemical properties generated from quantum size effects. Histidine-containing peptides have been reported for their high affinities to metal ions damaging central nervous systems by

changing peptide conformations into irregular forms. Through histidine-metal complexation and the protein deformation may cause human brain diseases such as Parkinson's and Alzheimer's diseases. Metallic nanowires were synthesized by applying the sequenced histidine-rich peptides as a template in a form of a nanotube. The specific sequenced peptides mineralizing specific metals/semiconductors can produce highly crystalline nanocrystals. The peptide conformational charges on nanotubes can control the size and the packing density of nanocrystals. M13 bacteriophage has been also used to electrostatically interact with AuNPs to form a hydrogel. Hydrogels composed of genetically engineered highly negative filamentous M13 phages and AuNPs.

Gold Nanoparticles have been used to make a various type of hydrogels. In this article, gold ions (Au^{3+} from $HAuCl_4$) are used to make a genetically engineered M13-phage based hydrogel by fusing a beta-amyloid peptide on the surface of the phage. It also produces fine gold nanoparticles (mostly <50nm) due to reducing power of M13 phage after the formation of hydrogel. The Au^{3+} ion-M13 phage hydrogel with embedded fine gold nanoparticles (B31 hydrogel) can be potentially used for many biomedical researches because of the unique properties of gold nanoparticle/ions and biosafe M13 phage.

3.2 Materials and Methods

3.2.1 Preparation of the engineered B31 phage

Through the previously published methods of phage display, a peptide sequence (HQKLVFFAED) was genetically fused on the pVIII coat proteins on the surface of genetically engineered M13 phage (B31 phage). (Figure 3.1)
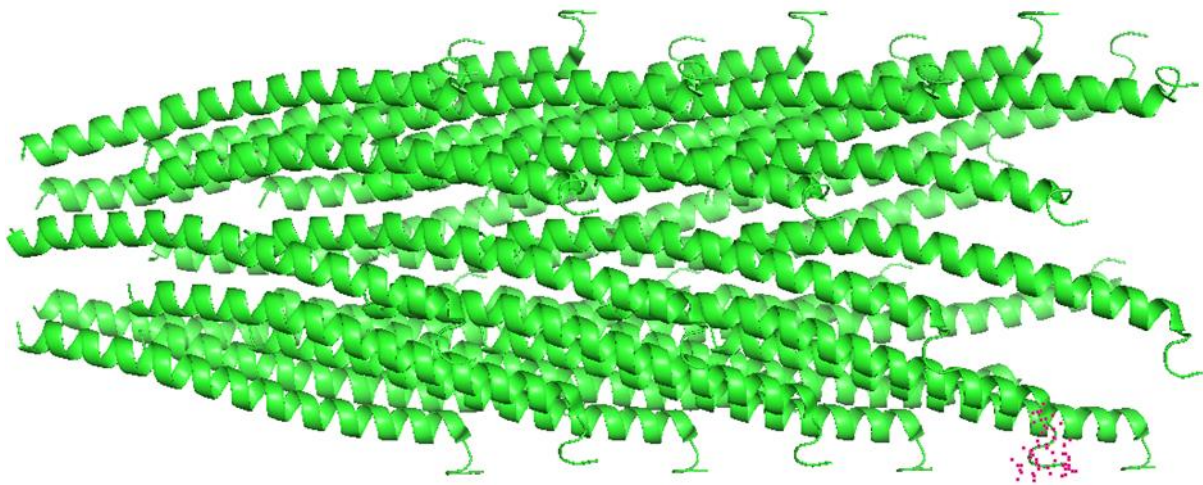

Figure 3.1 The pVIII major coat protein structure from PDB (Protein Data Bank) website, the tip of pVIII coat protein (pink dotted area) is where the novel peptide sequence (HQKLVFFAED) was genetically fused.

The B31 phage was amplified via the previously published protocol to fulfill the experimentally obtained critical/minimum concentration of the engineered M13 phage (2×10^{14} phage/ml).[29] The concentration of phage solution was measured, using the spectrometer, considering optical density (OD) 0.1 ((OD=0.1 in 1mm) (OD =1 in 1cm pathlength)) was unit-converted in to 1×10^{13} phages/ml based on the previously calculated data. The engineered phage solution was microfiltered with microfilter syringe (CORNING®) whose pore size was 0.2μm. The phage solution

was also purified via desalting process to remove ions and small undesired molecules in the phage solution by dialysis with a spectra/Por® 6 dialysis membrane (MW 50kD). Presence of B31 phages was confirmed by bio-AFM imaging using a biological atomic force microscope (Bruker Catalysis). (Figure 3.2)
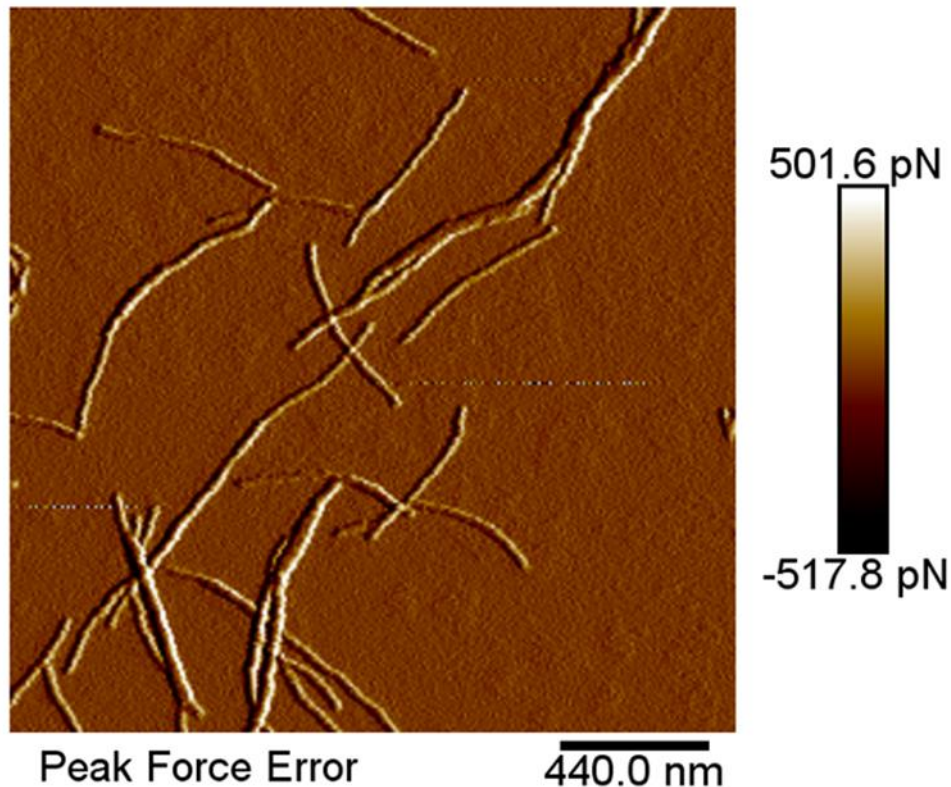
Figure 3.2 AFM images of B31 phage, B31 phage has also a filamentous virus shape like native M13 phage.

3.2.2 Au^{3+} ion-B31 phage Hydrogel Formation

50µl of 10mM Au^{3+} ions (in HAuCl$_4$, Chloroauric acid) was added to the 300µl of B31 phage solution (2.0 x 10^{14} phage/ml). After 2-3 hours at a room temperature (20 °C), Au^{3+} ions were passively/homogenously dispersed in the B31 phage solution and formed a hydrogel. Parts of B31 hydrogel were transferred into PBS, DMEM

media and hMSC media in the conical tubes for testing insolubility of B31 hydrogel in common biochemical cell culturing media.

3.2.3 Evaluation of B31 Hydrogel in mechanical properties

Torsional rheometer (Discovery Hybrid Rheometer, DHR-2) was used to measure the rheological behaviors of the hydrogels. B31 Hydrogel samples (300μl) were tested for storage modulus (elasticity) and loss modulus (viscosity) on steel parallel plate (geometry diameter = 40 mm) under the conditions of a time sweep at 37 °C with a 750 μm gap, and frequency sweep at 0.5-40 rad/s. Au^{3+} ion-WT aggregates were also tested as a control group in the same conditions.

3.2.4 AFM/TEM Imaging of AuNPs in Au^{3+}-B31 phage Hydrogel

After the Brightfield imaging for confirming the presence of AuNPs, AFM and TEM imaging methods were performed to visualize gold nanoparticles (AuNPs) in B31 hydrogel at higher magnifications and resolutions. ZEISS 10A Conventional Transmission Electron Microscope was used to perform TEM imaging in Microscopy Imaging lab at the University of Oklahoma. Bio-AFM imaging method was also used to visualize AuNPs in B31 hydrogel in the biological atomic force microscope (Bruker Catalysis). UV-vis Absorption spectrum was reviewed as a conformation. Absorption spectrum was also performed to find a peak at a certain wavelength to indicate an average size of AuNPs by following the data with Nano-spectrometer, compared to the related reference data.[101-103] (Table 3.1)

AuNP size	10nm	20nm	30nm	40nm	50nm	80nm	100nm

Peak Location (λ)	~515nm	~520nm	~530nm	~540nm	~550nm	~560nm	~580nm

Table 3.1 UV-vis absorption data for average gold nanoparticle (AuNP) size, the peak location moves to the left (lower wavelength (nm)) when AuNP size decreases and the peak location moves to the right (higher wavelength (nm)) when AuNP size increases. (average AuNP size (0.5nm – 100nm) range to correspond to peak wavelength (500nm – 600nm) range)

3.3 Results and Discussion

3.3.1 Au³⁺ ion-B31 phage Hydrogel

Peptide sequence (HQKLVFFAED) displaying M13 phage (B31 phage) was successfully amplified and mixed with Au^{3+} ions to form a hydrogel after 2-3 hours at a room temperature (20 °C) while WT phage did not form a hydrogel with Au^{3+} ions. After 24 hours, Au^{3+} ion-B31 hydrogel (Formed at Au^{3+} ion 1.5mM) turned light brown, indicating the formation of fine gold nanoparticles (fine AuNPs). Because of negatively charged amino acid resides (E and D) of displayed peptide (HQKLVFFAED), the overall surface net charge of B31 phages can be negative.[23, 27, 104] When B31 phages were engaged by Au^{3+} ions through metal ion-peptide interaction in a hydrogel structure, some Au^{3+} ions were reduced to form AuNPs due to a possible reducing effect of tightly bound negative side chains of amino acid residues in B31 phages. Additionally, the displayed peptide is an amyloid β-peptide motif that shows antiparallel alignments.[105] The antiparallel alignments among B31 phages with Au^{3+} ions will create small and tight spaces in B31 hydrogel inner network, and it may make a strong reducing power of B31 phages onto Au^{3+} ions

trapped in B31 hydrogel due to their proximate contacts. (Figure 3.3 and Figure 3.4) B31 hydrogel also show an excellent insolubility in water, PBS, and any other biochemical media. (Figure 3.5 and Figure 3.6)
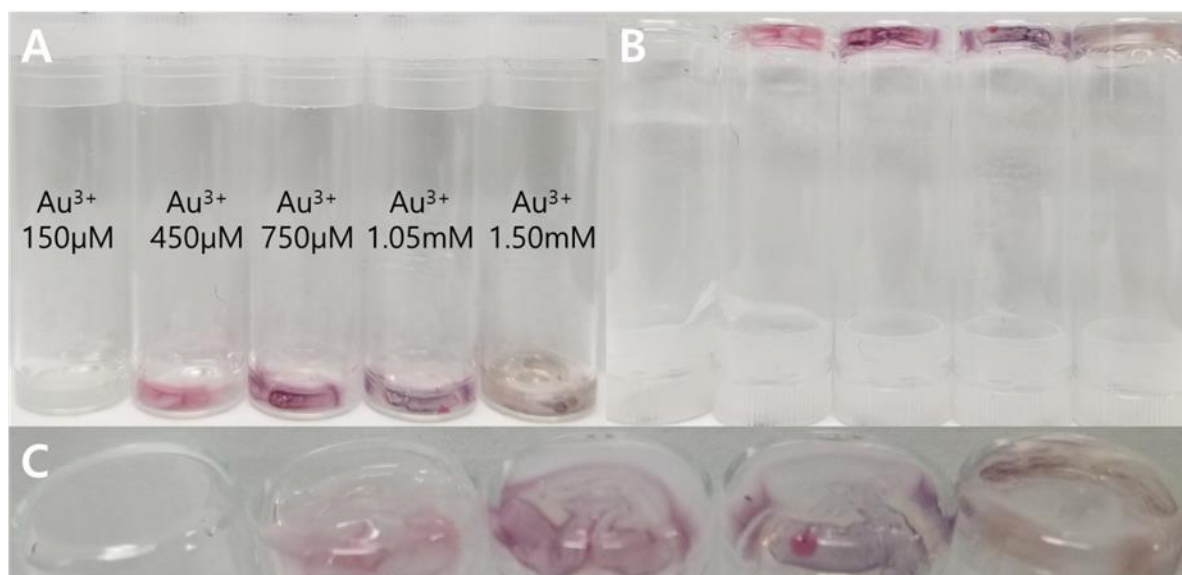

Figure 3.3 B31 hydrogel formation at different Au^{3+} ion concentrations, A critical concentration for Au^{3+} ion is 450µM. B31 phage showed a stronger interaction with Au^{3+} ions forming a light brown B31 hydrogel at Au^{3+} 1.5mM. Each different color of B31 hydrogel represents a different size of formed AuNPs in B31 hydrogel.
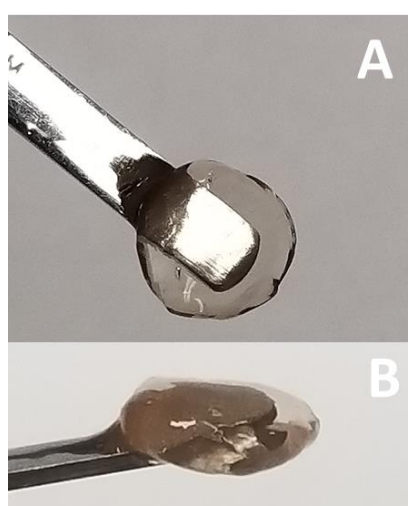

Figure 3.4 B31 hydrogel, (A) Top-down view of B31 hydrogel, (B) Side view of B31 hydrogel
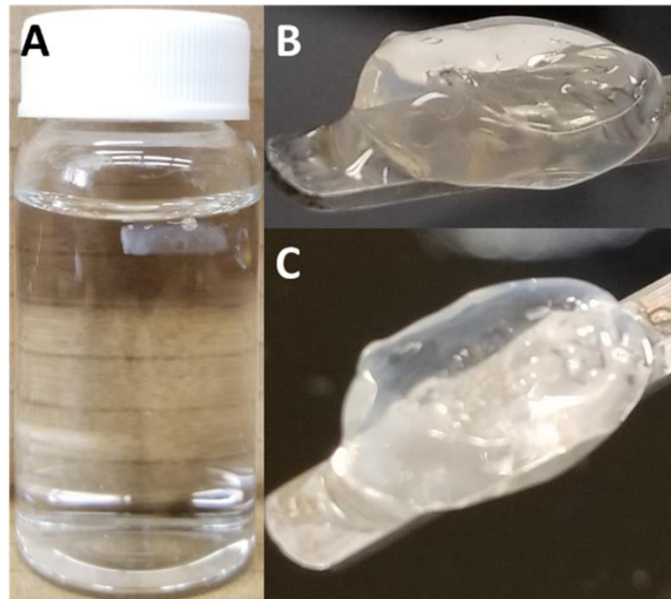
Figure 3.5 B31 hydrogel in distilled water, (A) B31 hydrogel is stable in water, (B) and (C) Freshly made B31 hydrogel is almost transparent without any color beside light white cloudiness due to B31 phage aggregations with Au^{3+} ions in the hydrogel. It indicates that there is almost no AuNPs formed in newly made B31 hydrogel.
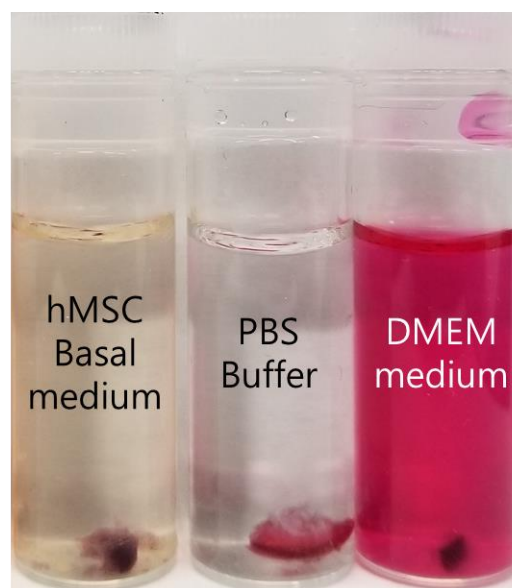

Figure 3.6 B31 hydrogel stability in biochemical media, a piece of B31 hydrogel was

inserted into each different medium. (hMSC basal medium, DMEM medium, and PBS buffer) B31 hydrogel showed a good insolubility in these three conditions regardless of time period.

3.3.2 B31 hydrogel mechanical properties

Au^{3+} ion-B31 hydrogel show higher values in storage modulus and loss modulus than ones of Au^{3+} ion-WT phage solution (a control) at all frequency sweeps at 0.5-40 rad/s. (Figure 3.7) B31 hydrogel is >8-fold more elastic and >2-fold more viscus than Au^{3+} ion-WT phage solution. It suggests that the interaction between Au^{3+} ions and B31 phages is stronger than one between Au^{3+} ions and WT phages.
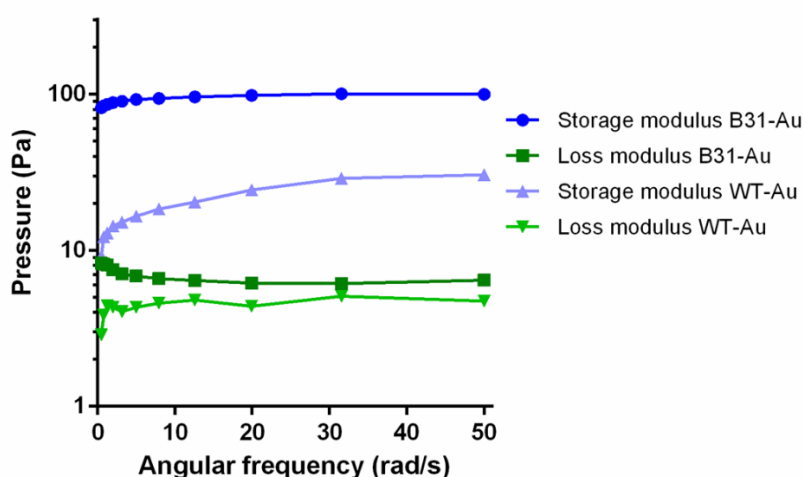

Figure 3.7 Mechanical strength of B31 hydrogel, the graph clearly indicates that WT phage does not interact with Au^{3+} ions as strong as B31 phage.

3.3.3 Fine AuNPs synthesis in Au^{3+}-B31 phage Hydrogel

The presence of fine AuNPs were first identified by brightfield imaging. (Figure 3.8) The dark regions in the phage hydrogel locate the AuNPs, formed in B31 hydrogel. AFM images confirmed that AuNPs in B31 hydrogel are smaller than ones

in Au^{3+} ion-WT phage complex. Based on the parameters in AFM software, the largest AuNPs in B31 hydrogel images were <50nm while there were AuNPs whose sizes were <200nm in Au^{3+} ion-WT phage complex. (Figure 3.9) In TEM images of B31 hydrogel and Au^{3+} ion-WT phage complex, the sizes of AuNPs were also smaller in B31 hydrogel than ones in Au^{3+} ion-WT phage complex. (Figure 3.10) The crystal structure of embedded AuNPs in B31 phage network in B31 hydrogel were found. (Figure 3.11) AuNPs in B31 hydrogel showed a peak around 529nm indicating the size of most AuNPs is 30nm. AuNPs in Au^{3+} ion-WT phage complex showed a low broad peak ranging 539nm, indicating the size of most AuNPs is >50nm. UV-vis absorption spectrum were obtained to confirm the size of AuNPs in B31 hydrogel. Absorption spectrum results also indicates the small AuNPs, formed in B31 hydrogel. (Figure 3.12)
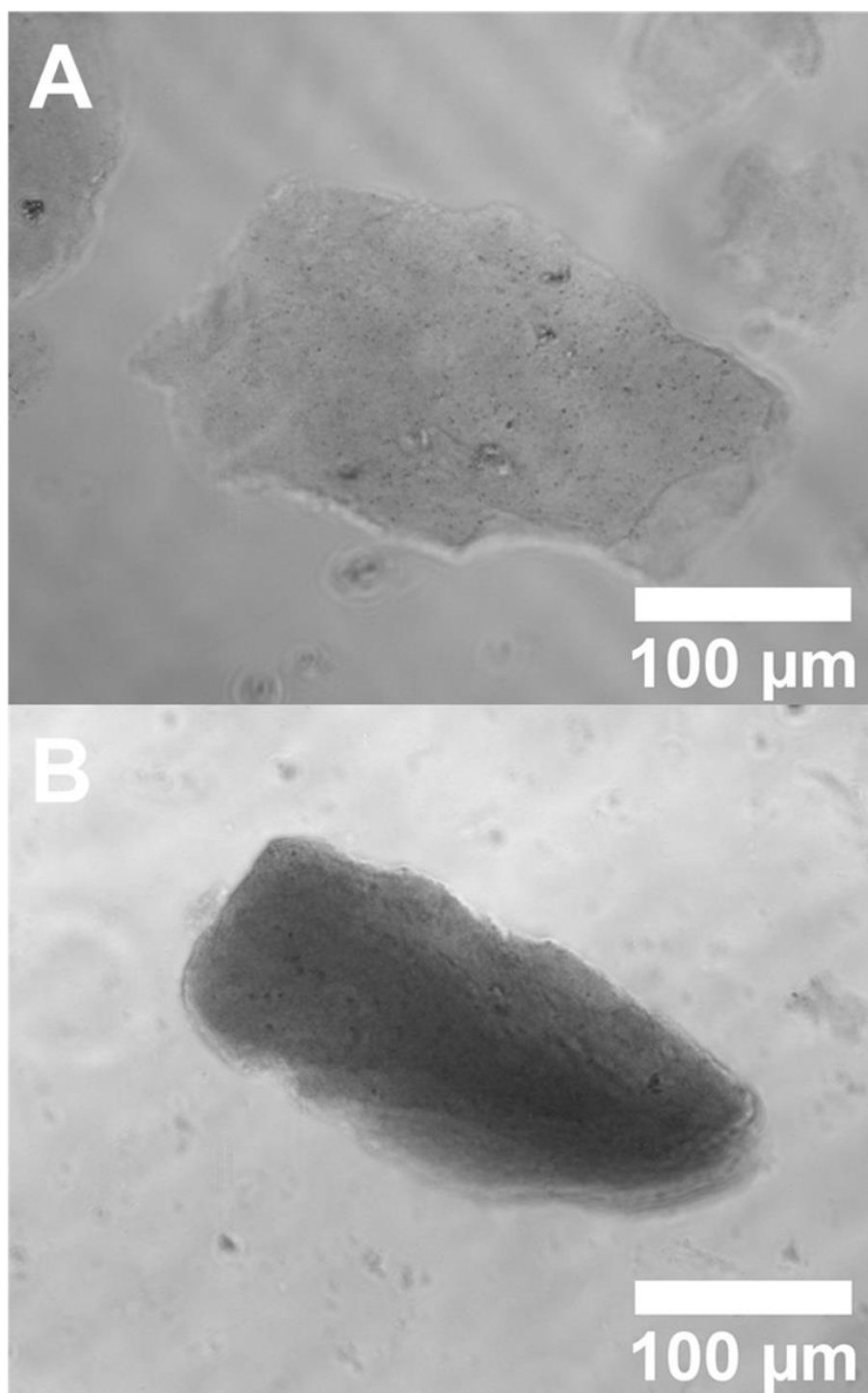
Figure 3.8 Brightfield Images of B31 hydrogel and Au^{3+} ion-WT phage complex, (A) B31 hydrogel has fine AuNPs, (B) WT phage complex has also AuNPs, that are larger than ones in B31 hydrogel.
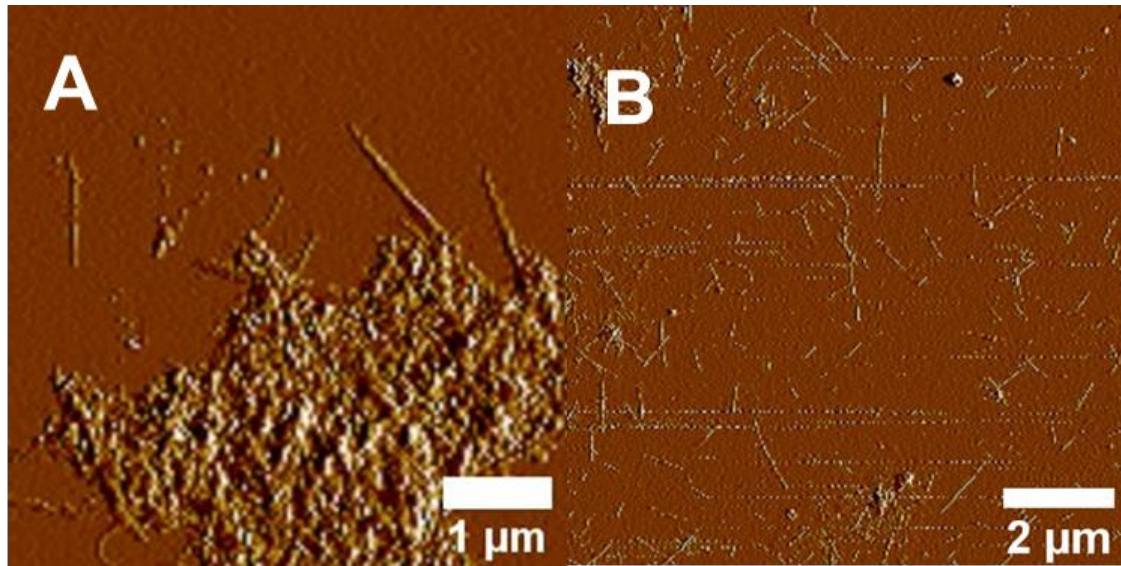
Figure 3.9 AFM images of B31 hydrogel and Au^{3+} ion-WT phage complex, (A) Fine AuNPs are found with B31 phage, (B) Many large AuNPs (>200nm) were found with WT phage.
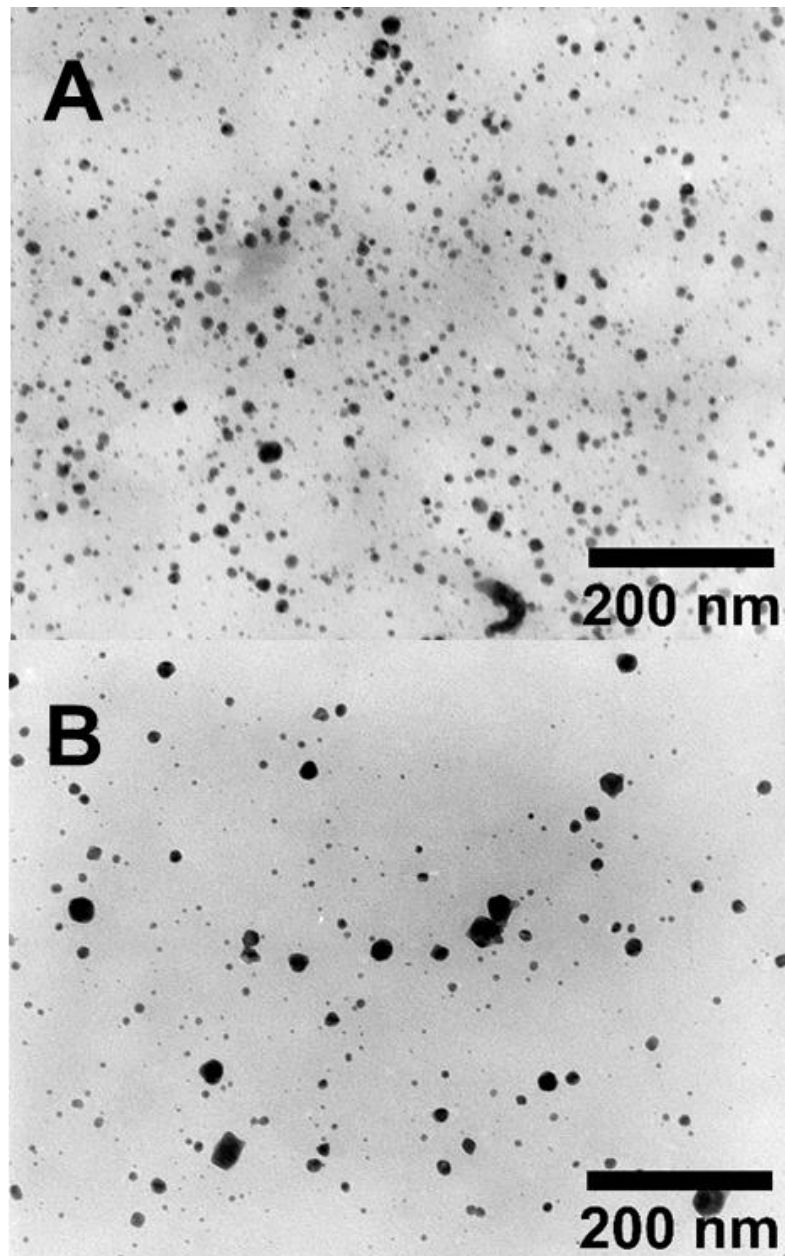
Figure 3.10 TEM images of B31 hydrogel and Au^{3+} ion-WT phage complex, AuNPs in B31 hydrogel (A) are smaller than AuNPs in Au^{3+} ion-WT phage complex (B).

Figure 3.11 AuNPs, formed in Au^{3+} ion-B31 phage linkages in B31 hydrogel inner network structure, the strong interaction between B31 phage and Au^{3+} ions induces fine AuNP synthesis possibly due to B31 phage encapsulating lower numbers of Au^{3+} ions in B31 hydrogel for later reduction to create AuNPs from captured Au^{3+} ions.

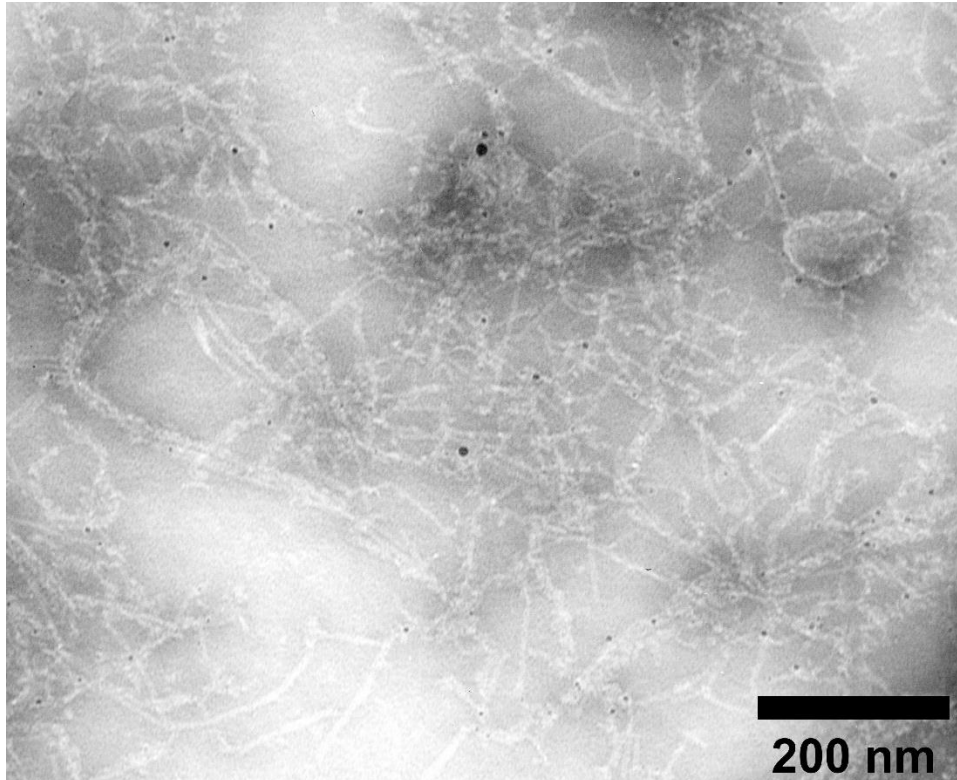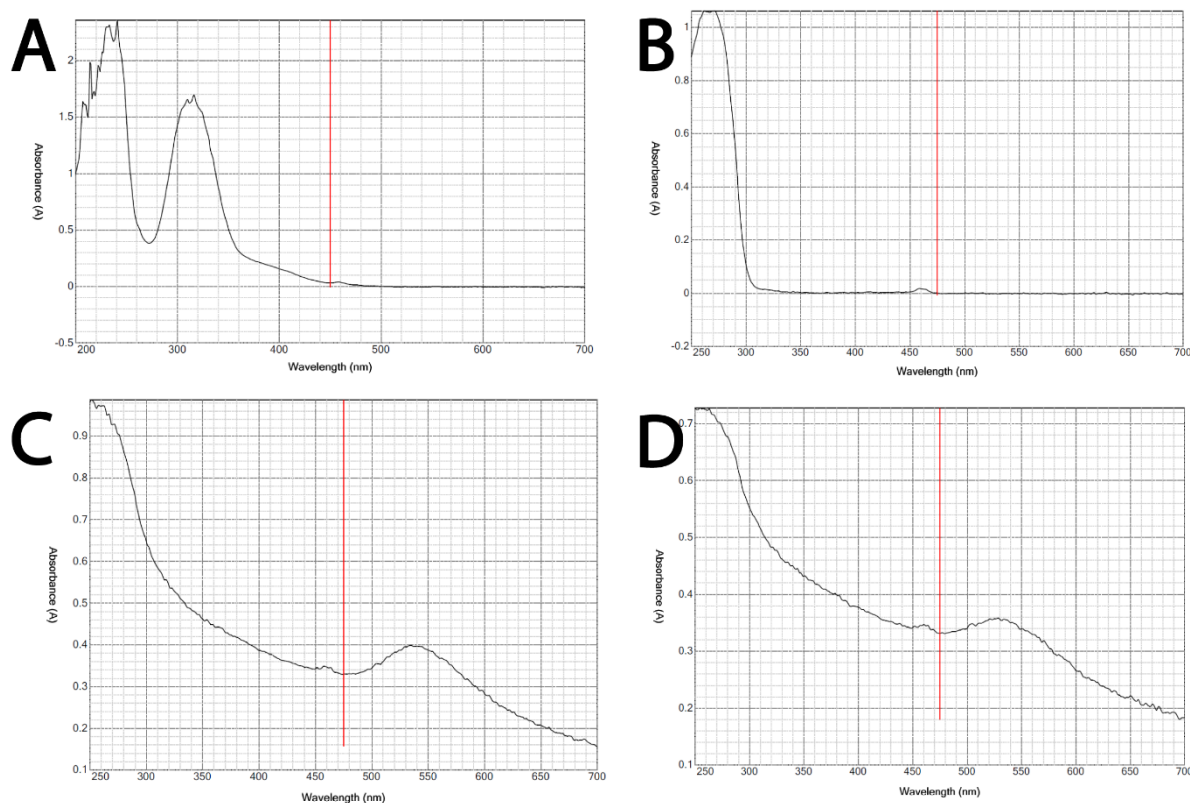**Figure 3.12** Absorption spectrum of (A) Au^{3+} ion, (B) B31 phage, (C) Au^{3+} ion-WT aggregated complex, a peak at 539nm, (D) B31 hydrogel, a peak at 529nm, the average size of AuNPs in B31 hydrogel (~30nm) is smaller than the average size of AuNPs in Au^{3+} ion-WT aggregated complex (~40nm-50nm).

3.4 Conclusion

Nanotechnology has been continuously developing with novel nanomaterials such as functionalized AuNPs for certain applications. Here is a novel green biochemical synthesis of AuNPs, that do not require a complex chemical reactions and toxic chemical reagents. Engineered M13 phage (B31 phage) can be a great reducing/stabilizing/capping agent of AuNPs. In comparison to WT phage, B31 phage can make finer AuNPs (>30-40nm) for a shorter time period (1-2 days). The Au^{3+} ion-B31 phage hydrogel with embedded fine gold nanoparticles (B31 hydrogel)

can be potentially used for many biomedical researches because of the better and unique properties of gold nanoparticle/ions and biosafe M13 phage hydrogel. (Figure 3.13)
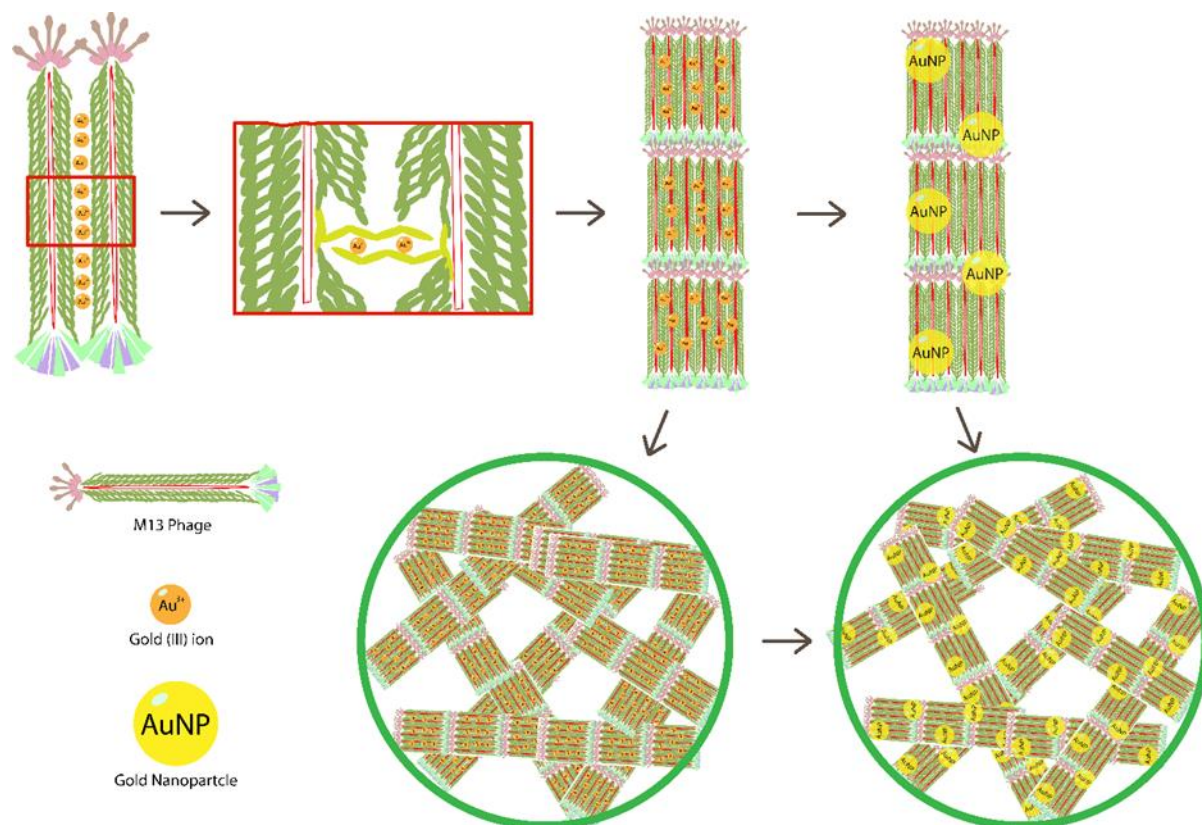

Figure 3.13 Schematic Image of overall process of green biochemical synthesis of fine AuNPs in Au^{3+} ion-B31 phage hydrogel

Appendix: List of Copyrights and Permissions

Copyright Clearance Center

RightsLink®

ACS Publications
Most Trusted. Most Cited. Most Read.

Title: Chemically Modifying Viruses for Diverse Applications
Author: Kritika Mohan, Gregory A. Weiss
Publication: ACS Chemical Biology
Publisher: American Chemical Society
Date: May 1, 2016
Copyright © 2016, American Chemical Society

PERMISSION/LICENSE IS GRANTED FOR YOUR ORDER AT NO CHARGE

This type of permission/license, instead of the standard Terms & Conditions, is sent to you because no fee is being charged for your order. Please note the following:

- Permission is granted for your request in both print and electronic formats, and translations.
- If figures and/or tables were requested, they may be adapted or used in part.
- Please print this page for your records and send a copy of it to your publisher/graduate school.
- Appropriate credit for the requested material should be given as follows: "Reprinted (adapted) with permission from (COMPLETE REFERENCE CITATION). Copyright (YEAR) American Chemical Society." Insert appropriate information in place of the capitalized words.
- One-time permission is granted only for the use specified in your request. No additional uses are granted (such as derivative works or other editions). For any other uses, please submit a new request.

If credit is given to another source for the material you requested, permission must be obtained from that source.

This Agreement between The University of Oklahoma -- James Cho ("You") and Springer Nature ("Springer Nature") consists of your license details and the terms and conditions provided by Springer Nature and Copyright Clearance Center.

License Number	4482170169180
License date	Dec 04, 2018
Licensed Content Publisher	Springer Nature
Licensed Content Publication	Nature Nanotechnology
Licensed Content Title	Virus-based piezoelectric energy generation
Licensed Content Author	Byung Yang Lee, Jinxing Zhang, Chris Zueger, Woo-Jae Chung, So Young Yoo et al.
Licensed Content Date	May 13, 2012
Licensed Content Volume	7
Licensed Content Issue	6
Type of Use	Thesis/Dissertation
Requestor type	academic/university or research institute
Format	electronic
Portion	figures/tables/illustrations
Number of figures/tables/illustrations	1
High-res required	no
Will you be translating?	no
Circulation/distribution	>50,000
Author of this Springer Nature content	no
Title	M13 BACTERIOPHAGE-BASED POLYMERS, A PROMISING NEXT GENERATION OF BIOHYDROGEL
Institution name	The University of Oklahoma
Expected presentation date	Dec 2018
Order reference number	23
Portions	Figure 3a
Requestor Location	The University of Oklahoma 101 Stephenson pkwy

Norman, OK 73019 United States Attn: The University of Oklahoma |
| Billing Type | Invoice |
| Billing Address | The University of Oklahoma 101 Stephenson pkwy

Norman, OK 73019 United States Attn: James L Cho |
| Total | 0.00 USD |

Title: Identification of Novel Short BaTiO3-Binding/Nucleating Peptides for Phage-Templated in Situ Synthesis of BaTiO3 Polycrystalline Nanowires at Room Temperature

Author: Yan Li, Binrui Cao, Mingying Yang, et al

Publication: Applied Materials

Publisher: American Chemical Society

Date: Nov 1, 2016

Copyright © 2016, American Chemical Society

PERMISSION/LICENSE IS GRANTED FOR YOUR ORDER AT NO CHARGE

This type of permission/license, instead of the standard Terms & Conditions, is sent to you because no fee is being charged for your order. Please note the following:

- Permission is granted for your request in both print and electronic formats, and translations.
- If figures and/or tables were requested, they may be adapted or used in part.
- Please print this page for your records and send a copy of it to your publisher/graduate school.
- Appropriate credit for the requested material should be given as follows: "Reprinted (adapted) with permission from (COMPLETE REFERENCE CITATION). Copyright (YEAR) American Chemical Society." Insert appropriate information in place of the capitalized words.
- One-time permission is granted only for the use specified in your request. No additional uses are granted (such as derivative works or other editions). For any other uses, please submit a new request.

If credit is given to another source for the material you requested, permission must be obtained from that source.

BACK | CLOSE WINDOW

JOHN WILEY AND SONS LICENSE
TERMS AND CONDITIONS

Dec 06, 2018

This Agreement between The University of Oklahoma -- James Cho ("You") and John Wiley and Sons ("John Wiley and Sons") consists of your license details and the terms and conditions provided by John Wiley and Sons and Copyright Clearance Center.

License Number	4483170815220
License date	Dec 06, 2018
Licensed Content Publisher	John Wiley and Sons
Licensed Content Publication	Angewandte Chemie International Edition
Licensed Content Title	Virus-Based Chemical and Biological Sensing
Licensed Content Author	Chuanbin Mao, Aihua Liu, Binrui Cao
Licensed Content Date	Aug 26, 2009
Licensed Content Volume	48
Licensed Content Issue	37
Licensed Content Pages	21
Type of use	Dissertation/Thesis
Requestor type	University/Academic
Format	Electronic
Portion	Figure/table
Number of figures/tables	2
Original Wiley figure/table number(s)	Figure 1 Figure 3
Will you be translating?	No
Title of your thesis / dissertation	M13 BACTERIOPHAGE-BASED POLYMERS, A PROMISING NEXT GENERATION OF BIOHYDROGEL
Expected completion date	Dec 2018
Expected size (number of pages)	71
Requestor Location	The University of Oklahoma 101 Stephenson pkwy Norman, OK 73019 United States Attn: The University of Oklahoma
Publisher Tax ID	EU826007151
Total	0.00 USD
Terms and Conditions	

This Agreement between The University of Oklahoma -- James Cho ("You") and Elsevier ("Elsevier") consists of your license details and the terms and conditions provided by Elsevier and Copyright Clearance Center.

License Number	4483171402966
License date	Dec 06, 2018
Licensed Content Publisher	Elsevier
Licensed Content Publication	Advanced Drug Delivery Reviews
Licensed Content Title	β-hairpin peptide hydrogels for package delivery
Licensed Content Author	Peter Worthington,Sigrid Langhans,Darrin Pochan
Licensed Content Date	Feb 1, 2017
Licensed Content Volume	110
Licensed Content Issue	n/a
Licensed Content Pages	10
Start Page	127
End Page	136
Type of Use	reuse in a thesis/dissertation
Intended publisher of new work	other
Portion	figures/tables/illustrations
Number of figures/tables/illustrations	1
Format	electronic
Are you the author of this Elsevier article?	No
Will you be translating?	No
Original figure numbers	Figure 2
Title of your thesis/dissertation	M13 BACTERIOPHAGE-BASED POLYMERS, A PROMISING NEXT GENERATION OF BIOHYDROGEL
Publisher of new work	The University of Oklahoma
Expected completion date	Dec 2018
Estimated size (number of pages)	71
Requestor Location	The University of Oklahoma 101 Stephenson pkwy
	Norman, OK 73019 United States Attn: The University of Oklahoma
Publisher Tax ID	98-0397604
Total	0.00 USD
Terms and Conditions	

ACS Publications
Most Trusted. Most Cited. Most Read.

Title: Accessing Three-Dimensional Crystals with Incorporated Guests through Metal-Directed Coiled-Coil Peptide Assembly

Author: Manish Nepal, Michael J. Sheedlo, Chittaranjan Das, et al

Publication: Journal of the American Chemical Society

Publisher: American Chemical Society

Date: Aug 1, 2016

Copyright © 2016, American Chemical Society

81

References

1.   Park, J. K.; Seo, S. K.; Cho, S.; Kim, H. S.; Lee, C. H., Characteristics of Sodium Polyacrylate/Nano-Sized Carbon Hydrogel for Biomedical Patch. *J Nanosci Nanotechno* **2018,** *18* (3), 1611-1614.

2.   Wang, Y.; Dou, C. Y.; He, G. D.; Ban, L. T.; Huang, L.; Li, Z.; Gong, J. X.; Zhang, J. F.; Yu, P., Biomedical Potential of Ultrafine Ag Nanoparticles Coated on Poly (Gamma-Glutamic Acid) Hydrogel with Special Reference to Wound Healing. *Nanomaterials-Basel* **2018,** *8* (5).

3.   Solaro, R.; Alderighi, M.; Barsotti, M. C.; Battisti, A.; Cifelli, M.; Losi, P.; Di Stefano, R.; Ghezzi, L.; Tine, M. R., Chemical-physical and in vivo evaluations of a self-assembling amphiphilic peptide as an injectable hydrogel scaffold for biomedical applications. *J Bioact Compat Pol* **2013,** *28* (1), 3-15.

4.   Deng, J.; Cheng, C.; Teng, Y. Y.; Nie, C. X.; Zhao, C. S., Mussel-inspired post-heparinization of a stretchable hollow hydrogel tube and its potential application as an artificial blood vessel. *Polym Chem-Uk* **2017,** *8* (14), 2266-2275.

5.   Ammar, M. M.; Waly, G. H.; Saniour, S. H.; Moussa, T. A., Growth factor release and enhanced encapsulated periodontal stem cells viability by freeze-dried platelet concentrate loaded thermo-sensitive hydrogel for periodontal regeneration. *Saudi Dent J* **2018,** *30* (4), 355-364.

6.   Wang, B.; Li, W. W.; Dean, D.; Mishra, M. K.; Wekesa, K. S., Enhanced hepatogenic differentiation of bone marrow derived mesenchymal stem cells on liver ECM hydrogel. *J Biomed Mater Res A* **2018,** *106* (3), 829-838.

7.   Black, K. A.; Lin, B. F.; Wonder, E. A.; Desai, S. S.; Chung, E. J.; Ulery, B. D.; Katari, R. S.; Tirrell, M. V., Biocompatibility and Characterization of a Peptide Amphiphile Hydrogel for Applications in Peripheral Nerve Regeneration. *Tissue Eng Pt A* **2015,** *21* (7-8), 1333-1342.

8.   Cheng, B. C.; Yan, Y. F.; Qi, J. J.; Deng, L. F.; Shao, Z. W.; Zhang, K. Q.; Li, B.; Sun, Z. L.; Li, X. M., Cooperative Assembly of a Peptide Gelator and Silk Fibroin Afford an Injectable Hydrogel for Tissue Engineering. *Acs Appl Mater Inter* **2018,** *10* (15), 12474-12484.

9.   Kufelnicki, A.; Swiatek, M.; Vogt, A.; Skarzewski, J., The cobalt(II)-N,N '-diglycylethylenediamine-dioxygen system - A potential model for metal-peptide interactions. *J Coord Chem* **1998,** *43* (1), 21-30.

10.   Sutherland, L., Rapid peptide synthesis - Next-generation, cost-effective means of peptide production. *Genet Eng News* **2003,** *23* (13), 1-+.

11.   Dauber, M.; Schnolzer, M.; Hoheisel, J.; Jacob, A., Parallel small scale peptide synthesis meets a fast, low-cost purification method for the production of high quality peptide microarrays to analyze DNA/protein interactions. *J Pept Sci* **2008,** *14* (8), 79-79.

12.   Russell, J., Reducing Peptide Synthesis Costs (vol 32, pg 30, 2012). *Genet Eng Biotechn N* **2012,** *32* (14), 8-8.

13.   Marvin, D. A.; Welsh, L. C.; Symmons, M. F.; Scott, W. R. P.; Straus, S. K., Molecular structure of fd (f1, M13) filamentous bacteriophage refined with respect to X-ray fibre diffraction and solid-

state NMR data supports specific models of phage assembly at the bacterial membrane. *J Mol Biol* **2006,** *355* (2), 294-309.

14.   Devaraj, V.; Han, J.; Kim, C.; Kang, Y. C.; Oh, J. W., Self-Assembled Nanoporous Biofilms from Functionalized Nanofibrous M13 Bacteriophage. *Viruses-Basel* **2018,** *10* (6).

15.   Tridgett, M.; Lloyd, J. R.; Kennefick, J.; Moore-Kelly, C.; Dafforn, T. R., Mutation of M13 Bacteriophage Major Coat Prote in for Increased Conjugation to Exogenous Compounds. *Bioconjugate Chem* **2018,** *29* (6), 1872-1875.

16.   Wang, J. L.; Wang, L.; Li, X.; Mao, C. B., Virus activated artificial ECM induces the osteoblastic differentiation of mesenchymal stem cells without osteogenic supplements. *Sci Rep-Uk* **2013,** *3*.

17.   Moghimian, P.; Srot, V.; Rothenstein, D.; Facey, S. J.; Harnau, L.; Hauer, B.; Bill, J.; van Aken, P. A., Adsorption and Self-Assembly of M13 Phage into Directionally Organized Structures on C and SiO2 Films. *Langmuir* **2014,** *30* (38), 11428-11432.

18.   Kishchenko, G. P.; Minenkova, O. O.; Ilichev, A. I.; Gruzdev, A. D.; Petrenko, V. A., Study of the Structure of Phage-M13 Virions Containing Chimeric B-Protein Molecules. *Mol Biol+* **1991,** *25* (6), 1171-1176.

19.   Makowski, L., Phage Display - Structure, Assembly and Engineering of Filamentous Bacteriophage-M13. *Curr Opin Struc Biol* **1994,** *4* (2), 225-230.

20.   Chung, W. J.; Lee, D. Y.; Yoo, S. Y., Chemical modulation of M13 bacteriophage and its functional opportunities for nanomedicine. *Int J Nanomed* **2014,** *9*, 5825-5836.

21.   Mohan, K.; Weiss, G. A., Chemically Modifying Viruses for Diverse Applications. *Acs Chem Biol* **2016,** *11* (5), 1167-1179.

22.   Chung, W. J.; Oh, J. W.; Kwak, K.; Lee, B. Y.; Meyer, J.; Wang, E.; Hexemer, A.; Lee, S. W., Biomimetic self-templating supramolecular structures. *Nature* **2011,** *478* (7369), 364-368.

23.   Lee, B. Y.; Zhang, J. X.; Zueger, C.; Chung, W. J.; Yoo, S. Y.; Wang, E.; Meyer, J.; Ramesh, R.; Lee, S. W., Virus-based piezoelectric energy generation. *Nat Nanotechnol* **2012,** *7* (6), 351-356.

24.   Mao, C. B.; Liu, A. H.; Cao, B. R., Virus-Based Chemical and Biological Sensing. *Angew Chem Int Edit* **2009,** *48* (37), 6790-6810.

25.   Cao, B. R.; Mao, C. B., Identification of Microtubule-Binding Domains on Microtubule-Associated Proteins by Major Coat Phage Display Technique. *Biomacromolecules* **2009,** *10* (3), 555-564.

26.   Kehoe, J. W.; Kay, B. K., Filamentous phage display in the new millennium. *Chem Rev* **2005,** *105* (11), 4056-4072.

27.   Li, Y.; Cao, B. R.; Yang, M. Y.; Zhu, Y.; Suh, J.; Mao, C. B., Identification of Novel Short BaTiO3-Binding/Nucleating Peptides for Phage-Templated in Situ Synthesis of BaTiO3 Polycrystalline Nanowires at Room Temperature. *Acs Appl Mater Inter* **2016,** *8* (45), 30714-30721.

28.   Liu, A. H.; Abbineni, G.; Mao, C. B., Nanocomposite Films Assembled from Genetically Engineered Filamentous Viruses and Gold Nanoparticles: Nanoarchitecture- and Humidity-Tunable

Surface Plasmon Resonance Spectra. *Adv Mater* **2009,** *21* (9), 1001-+.

29.   Binrui Cao, H. X., Chuanbin Mao, Phage as a Template to Grow Bone Mineral Nanocrystals. *Methods Mol Biol.* **2014,** *1108*, 123-135.

30.   Blaik, R. A.; Lan, E.; Huang, Y.; Dunn, B., Gold-Coated M13 Bacteriophage as a Template for Glucose Oxidase Biofuel Cells with Direct Electron Transfer. *Acs Nano* **2016,** *10* (1), 324-332.

31.   Robinson, N. E.; Robinson, A. B., Review article: Use of Merrifield solid phase peptide synthesis in investigations of biological deamidation of peptides and proteins. *Biopolymers* **2008,** *90* (3), 297-306.

32.   Chung, J.; Ha, C.; Kim, S.; Ahn, S.; Kwon, K., In Vivo selection of Target Peptides to Dysfunctional Endothelial Cells Using M13 Phage Peptide Display Library in Mice. *Circulation* **2013,** *128* (22).

33.   Nepal, M.; Sheedlo, M. J.; Das, C.; Chmielewski, J., Accessing Three-Dimensional Crystals with Incorporated Guests through Metal-Directed Coiled-Coil Peptide Assembly. *J Am Chem Soc* **2016,** *138* (34), 11051-11057.

34.   Dilger, J. M.; Glover, M. S.; Clemmer, D. E., A Database of Transition-Metal-Coordinated Peptide Cross-Sections: Selective Interaction with Specific Amino Acid Residues. *J Am Soc Mass Spectr* **2017,** *28* (7), 1293-1303.

35.   Prudent, M.; Girault, H. H., On-line electrogeneration of copper-peptide complexes in microspray mass spectrometry. *J Am Soc Mass Spectr* **2008,** *19* (4), 560-568.

36.   Franzini, E.; De Gioia, L.; Fantucci, P.; Zampella, G.; Bonacic-Koutecky, V., DFT investigation of copper-peptide complexes related to the octarepeat domain of the prion protein. *Inorg Chem Commun* **2003,** *6* (6), 650-653.

37.   Djalali, R.; Chen, Y. F.; Matsui, H., Au nanocrystal growth on nanotubes controlled by conformations and charges of sequenced peptide templates. *Abstr Pap Am Chem S* **2003,** *226*, U714-U714.

38.   Brodin, J. D.; Ambroggio, X. I.; Tang, C. Y.; Parent, K. N.; Baker, T. S.; Tezcan, F. A., Metal-directed, chemically tunable assembly of one-, two- and three-dimensional crystalline protein arrays. *Nat Chem* **2012,** *4* (5), 375-382.

39.   Karavasili, C.; Panteris, E.; Vizirianakis, I. S.; Koutsopoulos, S.; Fatouros, D. G., Chemotherapeutic Delivery from a Self-Assembling Peptide Nanofiber Hydrogel for the Management of Glioblastoma. *Pharm Res-Dordr* **2018,** *35* (8).

40.   Ichihara, Y.; Kaneko, M.; Yamahara, K.; Koulouroudias, M.; Sato, N.; Uppal, R.; Yamazaki, K.; Saito, S.; Suzuki, K., Self-assembling peptide hydrogel enables instant epicardial coating of the heart with mesenchymal stromal cells for the treatment of heart failure. *Biomaterials* **2018,** *154*, 12-23.

41.   Nguyen, P. K.; Gao, W.; Patel, S. D.; Siddiqui, Z.; Weiner, S.; Shimizu, E.; Sarkar, B.; Kumar, V. A., Self-Assembly of a Dentinogenic Peptide Hydrogel. *Acs Omega* **2018,** *3* (6), 5980-5987.

42.   Wang, J.; Liu, K.; Xing, R. R.; Yan, X. H., Peptide self-assembly: thermodynamics and

kinetics. *Chem Soc Rev* **2016,** *45* (20), 5589-5604.

43. Sun, J. E. P.; Stewart, B.; Litan, A.; Lee, S. J.; Schneider, J. P.; Langhans, S. A.; Pochan, D. J., Sustained release of active chemotherapeutics from injectable-solid beta-hairpin peptide hydrogel. *Biomater Sci-Uk* **2016,** *4* (5), 839-848.

44. Jin, H. L.; Wan, C.; Zou, Z. W.; Zhao, G. F.; Zhang, L. L.; Geng, Y. Y.; Chen, T.; Huang, A.; Jiang, F. G.; Feng, J. P.; Lovell, J. F.; Chen, J.; Wu, G.; Yang, K. Y., Tumor Ablation and Therapeutic Immunity Induction by an Injectable Peptide Hydrogel. *Acs Nano* **2018,** *12* (4), 3295-3310.

45. Worthington, P.; Langhans, S.; Pochan, D., beta-hairpin peptide hydrogels for package delivery. *Adv Drug Deliver Rev* **2017,** *110*, 127-136.

46. Rajagopal, K.; Lamm, M. S.; Haines-Butterick, L. A.; Pochan, D. J.; Schneider, J. P., Tuning the pH responsiveness of beta-hairpin peptide folding, self-assembly, and hydrogel material formation. *Biomacromolecules* **2009,** *10* (9), 2619-25.

47. Zhao, M.; Zhou, Y. J.; Liu, S. Y.; Li, L.; Chen, Y. N.; Cheng, J. Q.; Lu, Y. R.; Liu, J. P., Control release of mitochondria-targeted antioxidant by injectable self-assembling peptide hydrogel ameliorated persistent mitochondrial dysfunction and inflammation after acute kidney injury. *Drug Deliv* **2018,** *25* (1), 546-554.

48. Tang, J. X.; Janmey, P. A.; Lyubartsev, A.; Nordenskiold, L., Metal ion-induced lateral aggregation of filamentous viruses fd and M13. *Biophys J* **2002,** *83* (1), 566-581.

49. Stapleton, S. M.; Oseni, T. O.; Bababekov, Y. J.; Hung, Y. C.; Chang, D. C., Race/Ethnicity and Age Distribution of Breast Cancer Diagnosis in the United States. *Jama Surg* **2018,** *153* (6), 594-595.

50. Kurosky, S. K.; Mitra, D.; Zanotti, G.; Kaye, J. A., Treatment Patterns and Outcomes of Patients With Metastatic ER+/HER-2(-) Breast Cancer: A Multicountry Retrospective Medical Record Review. *Clin Breast Cancer* **2018,** *18* (4), E529-E538.

51. ODonoghue, C.; Zhou, J. M.; Collins, M.; Sun, W. H.; Lee, M., Trends in regional treatment for micrometastatic breast cancer: A National Cancer Database review. *Ann Surg Oncol* **2018,** *25*, 425-426.

52. Abrahams, H. J. G.; Gielissen, M. F. M.; Verhagen, C. A. H. H. V. M.; Knoop, H., The relationship of fatigue in breast cancer survivors with quality of life and factors to address in psychological interventions: A systematic review. *Clin Psychol Rev* **2018,** *63*, 1-11.

53. Ferraresso, L. G.; de Arruda, E. G. R.; de Moraes, T. P. L.; Fazzi, R. B.; Ferreira, A. M. D.; Abbehausen, C., Copper(II) and zinc(II) dinuclear enzymes model compounds: The nature of the metal ion in the biological function. *J Mol Struct* **2017,** *1150*, 316-328.

54. Habib-Ur-Rehman; Kaleemullah; Reman, F. U.; Akbar, A.; Khan, M. A.; Kakar, N.; Ahmad, M. Z.; Kakar, A.; Kakar, I.; Qudratullah; Kakar, M. A.; Ayub, M.; Kakar, S. A., Nutraceutical Applications of Copper, Manganese and Zinc in Rumen Metabolism and Body Immune Processes. *Indo Am J Pharm Sci* **2018,** *5* (1), 226-235.

55. Walser, M.; Bestwick, M., Quantifying the role of copper in modifying cytochrome c

oxidase expression and oxidant production in yeast mitochondria. *Abstr Pap Am Chem S* **2018,** *255*.

56.   Milnerowicz, H.; Jablonowska, M.; Bizon, A., Change of Zinc, Copper, and Metallothionein Concentrations and the Copper-Zinc Superoxide Dismutase Activity in Patients With Pancreatitis. *Pancreas* **2009,** *38* (6), 681-688.

57.   Jasmer-McDonald, K.; Petris, M.; Shanbhag, V.; Gudekar, N., Exploring the role of copper-dependent lysyl oxidase (LOX) in metastatic growth. *Cancer Res* **2017,** *77*.

58.   Jiang, H. X.; Kong, X. H.; Wang, S. P.; Guo, H. Y., Effect of Copper on Growth, Digestive and Antioxidant Enzyme Activities of Juvenile Qihe Crucian Carp, Carassius carassius, During Exposure and Recovery. *B Environ Contam Tox* **2016,** *96* (3), 333-340.

59.   Zowczak, M.; Iskra, M.; Torlinski, L.; Cofta, S., Analysis of serum copper and zinc concentrations in cancer patients. *Biological Trace Element Research* **2001,** *82* (1-3), 1-8.

60.   Finney, L.; Vogt, S.; Fukai, T.; Glesne, D., Copper and Angiogenesis: Unravelling a Relationship Key to Cancer Progression. *Clin Exp Pharmacol P* **2009,** *36* (1), 88-94.

61.   Jain, S.; Cohen, J.; Ward, M. M.; Kornhauser, N.; Chuang, E.; Cigler, T.; Moore, A.; Donovan, D.; Lam, C.; Cobham, M. V.; Schneider, S.; Rua, S. M. H.; Benkert, S.; Greenwood, C. M.; Zelkowitz, R.; Warren, J. D.; Lane, M. E.; Mittal, V.; Rafii, S.; Vandat, L. T., Tetrathiomolybdate-associated copper depletion decreases circulating endothelial progenitor cells in women with breast cancer at high risk of relapse. *Ann Oncol* **2013,** *24* (6), 1491-1498.

62.   Nackos, E.; Lee, S.; Willis, A.; Kornhauser, N.; Ward, M.; Cobham, M.; Cigler, T.; Moore, A.; Fitzpatrick, V.; Schneider, S.; Wiener, A.; Guillaume-Abraham, J.; Seo, B. R.; Warren, J. D.; Rubinchik, A.; Fischbach, C.; Mittal, V.; Vandat, L., Copper depletion as a strategy to affect the tumor microenvironment in breast cancer patients at high risk of relapse and in triple negative preclinical models of breast cancer: Updated results of a phase II study of tetrathiomolybdate (TM) in breast cancer (BC) patients (pts) at high risk for recurrence. *Cancer Res* **2016,** *76*.

63.   Michels, A.; Yu, D.; Frei, B., Selective Delivery of Copper Enhances Cytotoxicity of Millimolar Concentrations of Ascorbate towards Cancer Cells. *Faseb J* **2015,** *29*.

64.   Kaplan, J. H.; Maryon, E. B., How Mammalian Cells Acquire Copper: An Essential but Potentially Toxic Metal. *Biophys J* **2016,** *110* (1), 7-13.

65.   Liang, Q.; Dedon, P. C., Cu(II)/H2O2-induced DNA damage is enhanced by packaging of DNA as a nucleosome. *Chem Res Toxicol* **2001,** *14* (4), 416-422.

66.   Pham, D. Q. H.; Li, M. S.; La Penna, G., Copper Binding Induces Polymorphism in Amyloid-beta Peptide: Results of Computational Models. *J Phys Chem B* **2018,** *122* (29), 7243-7252.

67.   Di Natale, G.; Bellia, F.; Sciacca, M. F. M.; Campagna, T.; Pappalardo, G., Tau-peptide fragments and their copper(II) complexes: Effects on Amyloid-beta aggregation. *Inorg Chim Acta* **2018,** *472*, 82-92.

68.   Bielawski, K.; Bielawska, A.; Slodownik, T.; Poplawska, B.; Bolkun-Skornicka, U., DNA-binding activity and cytotoxicity of Pt-berenil compounds in MDA-MB-231 and MCF-7 breast

cancer cells. *Acta Pol Pharm* **2008,** *65* (1), 135-140.

69.   Akbas, S. H.; Timur, M.; Ozben, T., The effect of quercetin on topotecan cytotoxicity in MCF-7 and MDA-MB 231 human breast cancer cells. *Clin Chim Acta* **2005,** *355*, S308-S308.

70.   Soleymani, J.; Hasanzadeh, M.; Somi, M. H.; Shadjou, N.; Jouyban, A., Probing the specific binding of folic acid to folate receptor using amino-functionalized mesoporous silica nanoparticles for differentiation of MCF 7 tumoral cells from MCF 10A. *Biosens Bioelectron* **2018,** *115*, 61-69.

71.   Witkowska, D.; Bielinska, S.; Kamysz, W.; Kozlowski, H., Cu2+ and Ni2+ interactions with N-terminal fragments of Hpn and Hpn-like proteins from Helicobacter pylori Unusual impact of poly-Gln sequence on the complex stability. *J Inorg Biochem* **2011,** *105* (2), 208-214.

72.   Nunes, A. M.; Zavitsanos, K.; Malandrinos, G.; Hadjiliadis, N., Coordination of Cu2+ and Ni2+ with the histone model peptide of H2B N-terminal tail (1-31 residues): A spectroscopic study. *Dalton T* **2010,** *39* (18), 4369-4381.

73.   Drew, S. C.; Masters, C. L.; Barnham, K. J., Alzheimer's A beta Peptides with Disease-Associated N-Terminal Modifications: Influence of Isomerisation, Truncation and Mutation on Cu2+ Coordination (vol 5, e15875, 2010). *Plos One* **2014,** *9* (7).

74.   Santana, R. C.; Cunha, R. O.; Santos, M. G.; Ferreira, K. D.; Carvalho, J. F.; Calvo, R., Growth, EPR and optical absorption spectra of L-threonine single crystals doped with Cu2+ ions. *J Phys Chem Solids* **2007,** *68* (4), 586-593.

75.   Remko, M.; Fitz, D.; Rode, B. M., Effect of metal ions (Li+, Na+, K+, Mg2+, Ca2+, Ni2+, Cu2+, and Zn2+) and water coordination on the structure and properties of L-arginine and zwitterionic L-arginine. *J Phys Chem A* **2008,** *112* (33), 7652-7661.

76.   Jehdaramarn, A.; Pornsuwan, S.; Chumsaeng, P.; Phomphrai, K.; Sangtrirutnugul, P., Effects of appended hydroxyl groups and ligand chain length on copper coordination and oxidation activity. *New J Chem* **2018,** *42* (1), 654-661.

77.   Kim, I.; Moon, J. S.; Oh, J. W., Recent advances in M13 bacteriophage-based optical sensing applications. *Nano Converg* **2016,** *3* (1), 27.

78.   Vikhoreva, N. N.; Vikhorev, P. G.; Fedorova, M. A.; Hoffmann, R.; Mansson, A.; Kuleva, N. V., The in vitro motility assay parameters of actin filaments from Mytilus edulis exposed in vivo to copper ions. *Arch Biochem Biophys* **2009,** *491* (1-2), 32-38.

79.   Davies, M. J., The oxidative environment and protein damage. *Bba-Proteins Proteom* **2005,** *1703* (2), 93-109.

80.   Liu, J.; Yuan, C.; Pu, L. Q.; Wang, J., Nutrient deprivation induces apoptosis of nucleus pulposus cells via activation of the BNIP3/AIF signalling pathway. *Mol Med Rep* **2017,** *16* (5), 7253-7260.

81.   Chiou, S. K.; Hoa, N.; Ge, L. S.; Jadus, M. R., Nutrient Availability Alters the Effect of Autophagy on Sulindac Sulfide-Induced Colon Cancer Cell Apoptosis. *Gastroent Res Pract* **2012**.

82.   Silvestri, A.; Palumbo, F.; Rasi, I.; Posca, D.; Pavlidou, T.; Paoluzi, S.; Castagnoli, L.; Cesareni, G., Metformin Induces Apoptosis and Downregulates Pyruvate Kinase M2 in Breast Cancer Cells

Only When Grown in Nutrient-Poor Conditions. *Plos One* **2015,** *10* (8).

83.   Sepantafar, M.; Maheronnaghsh, R.; Mohammadi, H.; Radmanesh, F.; Hasani-Sadrabadi, M. M.; Ebrahimi, M.; Baharvand, H., Engineered Hydrogels in Cancer Therapy and Diagnosis. *Trends Biotechnol* **2017,** *35* (11), 1074-1087.

84.   Liu, Y. C.; Shu, X. Z.; Prestwich, G. D., Tumor engineering: Orthotopic cancer models in mice using cell-loaded, injectable, cross-linked hyaluronan-derived hydrogels. *Tissue Eng* **2007,** *13* (5), 1091-1101.

85.   Suwalsky, M.; Ungerer, B.; Quevedo, L.; Aguilar, F.; Sotomayor, C. P., Cu2+ ions interact with cell membranes. *J Inorg Biochem* **1998,** *70* (3-4), 233-238.

86.   Kim, A.; Shin, T. H.; Shin, S. M.; Pham, C. D.; Choi, D. K.; Kwon, M. H.; Kim, Y. S., Cellular Internalization Mechanism and Intracellular Trafficking of Filamentous M13 Phages Displaying a Cell-Penetrating Transbody and TAT Peptide. *Plos One* **2012,** *7* (12).

87.   Priyadarshini, E.; Pradhan, N., Gold nanoparticles as efficient sensors in colorimetric detection of toxic metal ions: A review. *Sensor Actuat B-Chem* **2017,** *238*, 888-902.

88.   Khan, M. E.; Khan, M. M.; Cho, M. H., Environmentally sustainable biogenic fabrication of AuNP decorated-graphitic g-C3N4 nanostructures towards improved photoelectrochemical performances. *Rsc Adv* **2018,** *8* (25), 13898-13909.

89.   Phanchai, W.; Srikulwong, U.; Chompoosor, A.; Sakonsinsiri, C.; Puangmali, T., Insight into the Molecular Mechanisms of AuNP-Based Aptasensor for Colorimetric Detection: A Molecular Dynamics Approach. *Langmuir* **2018,** *34* (21), 6161-6169.

90.   Gabig-Ciminska, M., Developing nucleic acid-based electrical detection systems. *Microb Cell Fact* **2006,** *5*, 9.

91.   Chen, H.; Zhou, K.; Zhao, G. H., Gold nanoparticles: From synthesis, properties to their potential application as colorimetric sensors in food safety screening. *Trends Food Sci Tech* **2018,** *78*, 83-94.

92.   Wang, C.; Yu, C. X., Detection of chemical pollutants in water using gold nanoparticles as sensors: a review. *Rev Anal Chem* **2013,** *32* (1), 1-14.

93.   Luczak, T., Development of a new voltammetric sensor by using a hybrid material consisting of gold nanoparticles and S-organic compounds for detection of deferiprone-anti-thalassemia and anti HIV-1 drug. *Measurement* **2018,** *126*, 242-251.

94.   Rasouli, Z.; Ghavami, R., Enhanced Sensitivity to Detection Nanomolar Level of Cu2+ Compared to Spectrophotometry Method by Functionalized Gold Nanoparticles: Design of Sensor Assisted by Exploiting First-order Data with Chemometrics. *Spectrochim Acta A* **2018,** *191*, 336-344.

95.   Stamatelatos, A.; Sousanis, A.; Chronis, A. G.; Sigalas, M. M.; Grammatikopoulos, S.; Poulopoulos, P., Analysis of localized surface plasmon resonances in gold nanoparticles surrounded by copper oxides. *J Appl Phys* **2018,** *123* (8).

96.   Avakyan, L. A.; Heinz, M.; Skidanenko, A. V.; Yablunovski, K. A.; Ihlemann, J.; Meinertz, J.;

Patzig, C.; Dubiel, M.; Bugaev, L. A., Insight on agglomerates of gold nanoparticles in glass based on surface plasmon resonance spectrum: study by multi-spheres T-matrix method. *J Phys-Condens Mat* **2018,** *30* (4).

97.   Stolle, H. L. K. S.; Garwe, F.; Muller, R.; Krech, T.; Oberleiter, B.; Rainer, T.; Fritzsche, W.; Stolle, A., Design of a scalable AuNP catalyst system for plasmon-driven photocatalysis. *Rsc Adv* **2018,** *8* (53), 30289-30297.

98.   Shang, C. X.; Cai, C.; Zhao, C. X.; Du, Y. G., Synthesis and anti-inflammatory activity of gold-nanoparticle bearing a dermatan sulfate disaccharide analog. *Chinese Chem Lett* **2018,** *29* (1), 81-83.

99.   de Souza, C. D.; Rostelato, M. C. M.; Zeituni, C.; Gonzalez, A. D. C.; Nogueira, B. R., New Gold-198 Nanoparticle Synthesis to Be Used in Cancer Treatment. *Med Phys* **2018,** *45* (6), E243-E243.

100.   Parboosing, R.; Govender, T.; Maguire, G. E. M.; Kruger, H. G., Synthesis, Characterization and Biocompatibility of a Multifunctional Gold Nanoparticle System for the Delivery of Single-Stranded RNA to Lymphocytes. *S Afr J Chem-S-Afr T* **2018,** *71*, 1-+.

101.   Khlebtsov, N. G., Determination of size and concentration of gold nanoparticles from extinction spectra. *Anal Chem* **2008,** *80* (17), 6620-6625.

102.   Haiss, W.; Thanh, N. T. K.; Aveyard, J.; Fernig, D. G., Determination of size and concentration of gold nanoparticles from UV-Vis spectra. *Anal Chem* **2007,** *79* (11), 4215-4221.

103.   Gadogbe, M.; Ansar, S. M.; He, G. L.; Collier, W. E.; Rodriguez, J.; Liu, D.; Chu, I. W.; Zhang, D. M., Determination of colloidal gold nanoparticle surface areas, concentrations, and sizes through quantitative ligand adsorption. *Anal Bioanal Chem* **2013,** *405* (1), 413-422.

104.   Lamboy, J. A.; Arter, J. A.; Knopp, K. A.; Der, D.; Overstreet, C. M.; Palermo, E. F.; Urakami, H.; Yu, T. B.; Tezgel, O.; Tew, G. N.; Guan, Z. B.; Kuroda, K.; Weiss, G. A., Phage Wrapping with Cationic Polymers Eliminates Nonspecific Binding between M13 Phage and High p/Target Proteins. *J Am Chem Soc* **2009,** *131* (45), 16454-16460.

105.   Tjernberg, L. O.; Tjernberg, A.; Bark, N.; Shi, Y.; Ruzsicska, B. P.; Bu, Z. M.; Thyberg, J.; Callaway, D. J. E., Assembling amyloid fibrils from designed structures containing a significant amyloid beta-peptide fragment. *Biochem J* **2002,** *366*, 343-351.